AB INITIO STUDIES OF THE STRUCTURAL, DYNAMICAL AND

THERMODYNAMICAL PROPERTIES OF GRAPHITIC AND

HYDROGENATED GRAPHITIC MATERIALS AND THEIR POTENTIAL

FOR USE IN HYDROGEN STORAGE

RANA MUHAMMAD ARIF KHALIL

Ph.D. Thesis   2014

Ab initio Studies of the Structural, Dynamical and Thermodynamical Properties of Graphitic and Hydrogenated Graphitic Materials and their Potential For use in Hydrogen Storage

Rana Muhammad Arif Khalil

Physics and Materials Research Centre
School of Computing, Science and Engineering
University of Salford, Salford, UK.

Submitted in Partial Fulfilment of the Requirements of the Degree of Doctor of Philosophy, May 2014.

Contents

List of Figures

List of Tables

Acknowledgements

There are a number of people to whom I would like to offer my appreciations for their help and advice throughout the completion of this work.

First and foremost, I am highly grateful to my supervisor Prof Ian Morrison, for his advice and guidance. Without his support and encouragement, it would have been more difficult to complete my research.

Secondly, I would like to offer thank to the University of Salford, where I spent my beautiful periods of life in research. I found very hospitable staff and teachers.

I am indebted to Prof. Keith Ross for discussion about the research materials. I am also thankful to Dr. Daniel Roach for his help. I would like to offer my thanks to Anne Sherwin [Librarian] for the support and encouragement. I am also grateful to Gael Baldissin and Mark Lunde as colleagues they provided me support to work on cluster machine.

I also want to thank my brothers and sisters for their patience throughout the period of my research.

Special thanks go to Higher Education Commission Pakistan for providing me scholarship to study in United Kingdom.

Symbolic Representations and Abbreviations

PBE	Perdew Burke Ernzerhof
G06	Grimme Correction
TS	Tkatchenko and Scheffler Correction
DFPT	Density Functional Perturbation Theory
OTF	On The Fly
GGA	Generalized Gradient Approximation
LDA	Local Density Approximation
DFT-D	Density Functional Dispersion Correction
VdW	Van der Waals
BFGS	Broyden-Fletcher-Goldfarb-Shanno
CNTs	Carbon Nanotubes
SWNT	Single Wall Nanotube
DFT	Density Functional Theory
C-H	Carbon-Hydrogen Bond
QHA	Quasi Harmonic Approximation
ZPE	Zero-point energy
CASTEP	CAmbridge Serial Total Energy Package

Abstract

The study presented in this PhD thesis is related to exploration of the properties of graphitic materials within the frame-work of ab initio methods. Structural and dynamical properties of graphitic materials are evaluated using the ab initio pseudopotential method. In graphitic materials, properties are obtained by incorporating Van der Waals interactions together with the generalized gradient approximation to density functional theory. These Van der Waals interactions improve the structural and dynamics of graphitic systems.

In order to study the dynamical properties, the finite displacement method has been used to construct the dynamical matrix and force constant matrix. Phonon dispersions are investigated by the direct force constant matrix method in supercells. In this approach, force constants are assumed to be zero beyond a certain limit. Phonon frequencies are calculated from the force constant matrix. The dispersion relations and the Brillouin zone integrated density of states are also investigated.

The significance of phonon dispersion has been studied to in various regions. Results are compared with dispersion corrected scheme and without dispersion corrected schemes to understand the importance of dispersion correction. Conclusions are also drawn on the applicability of theoretical approximations used. Further, ab initio results are also compared with the available data from experimental studies.

The binding energies and electronic band gaps of exo-hydrogenated carbon nanotubes are determined to investigate the stability and band gap opening using density functional theory. The vibrational density of states for hydrogenated carbon nanotubes has been calculated to confirm the C-H stretching mode due to sp^3 hybridization. The thermodynamical stability of hydrogenated carbon nanotubes has been explored in the chemisorption limit. Statistical physics and density functional theory calculations have been used to predict hydrogen release temperatures at standard pressure in zigzag and armchair carbon nanotubes.

Chapter 1. Introduction

The extra-ordinary variety of carbon allotropes gives them a special place in diverse fields such as nano-electronics and bio-engineering. Structural, dynamical and thermodynamical properties of graphitic materials lead to many important phenomena of physics. The most important form of carbon is known as graphite. This mechanically soft material is mostly used in pencil leads utilizing its weak inter-layer interactions. Graphite is also an important material due to its high conductivity.

The recent discovery of graphene has highlighted the need for graphitic materials. In future, graphene (Novoselov et al., 2005, Geim and Novoselov, 2007) can be considered as an important form among the carbon family. Graphene is becoming a rising star on the horizon of material science and condensed matter physics. Graphene consists of flat mono layers of carbon atoms tightly packed into a 2D (two dimensional) honey comb lattice and is considered as a building block for graphite materials of all other dimensions. It can be wrapped up to 0D fullerenes, rolled into 1D nanotubes or stacked in to 3D graphite. Properties of carbon based materials change on shrinking the size down to the nano scale. Therefore graphite, graphene and carbon nanotubes (CNTs) have many interesting structural and dynamical properties in 3D, 2D and 1D respectively.

Carbon nanotubes research was greatly encouraged by the initial report of the observations of carbon tubules of nanometer dimensions (Iijima, 1991) with amazing mechanical, thermal and electronic properties. CNTs are among the strongest and most resilient materials known to exist in nature. Their electronic properties present peculiar features in the sense that these properties depend on tube geometry, resulting in semiconductor or metallic character (Tans et al., 1997). CNTs have an important application as these can be used as hydrogen storage materials. Hydrogen can meet the energy demand of a hungry world to cover the energy shortage and global climate change in a scenario where hydrogen is produced by carbon neutral methods. It is important to find the ways to store the hydrogen on board efficiently and safely for the purpose of hydrogen powered transportation (Nikitin et al., 2005).

One of the suitable ways for storage is hydrogen adsorption on a medium which is useful for adsorbing and releasing amounts of hydrogen. Carbon based materials like graphite and CNTs are also widely used to store the hydrogen. Recently high attention has been paid to the carbon nanotube as potential hydrogen storage medium due to its light mass density and high surface to volume ratio, as well as a high degree of reactivity between carbon and hydrogen (Dillon et al., 1997). But still controversy is found about the storage of hydrogen in single wall carbon nanotubes. This controversy arises due to fact that Single Wall Nanotubes (SWNTs) can be either metal or semiconductor in nature depending on their diameters and helicities (Wu et al., 2006).

It is vital to understand the interactions of CNTs with the hydrogen molecule and atomic hydrogen. Both physisorption and chemisorption methods are used to store the hydrogen in CNTs. Physisorption, that is the process of weak adsorption of molecular hydrogen on SWNTs has been widely investigated and debated but covalent reactions between atomic hydrogen and SWNTs have a particular interest and are still less explored (Li et al., 2003).

1.1.   Atomic structure of Carbon Nanotubes

The pure element carbon can be found in different allotropes. In 1985, Kroto et. al discovered fullerene. Before this only amorphous carbon, graphite and diamond were included in well-known forms of carbon. One of the most important and prominent molecule is the spherical bucky ball C_{60}, which has a bound structure similar to the seams of an old fashioned soccer ball. After this discovery, it became accepted that sp^2 hybrid graphene layers exist not only in planar honeycomb sheets like in graphite but also as spherical curved and closed shaped cages. In 1991, Iijima discovered a cylindrical form of the bucky ball, known as the nanotube. These new fullerenes divide into two main categories: Single Wall Nanotube (SWNT) and Multi Walls Nanotube (MWNT). SWNT consists of one graphene sheet rolled into cylinder and MWNT is made of several concentric SWNTs.

In this section, basic atomic structures of graphene and CNTs are described. The unit cell of graphene contains two carbon atoms **A** and **B** as shown in Figure 1-1 and the distance $\mathbf{a_{cc}}$ between carbon to carbon atoms is about 0.142 nm (Buchs,

2008). Graphene to graphene inter planar spacing is about 0.335 nm in a graphite stack, where $\mathbf{a_1}$ and $\mathbf{a_2}$ are primitive vectors.
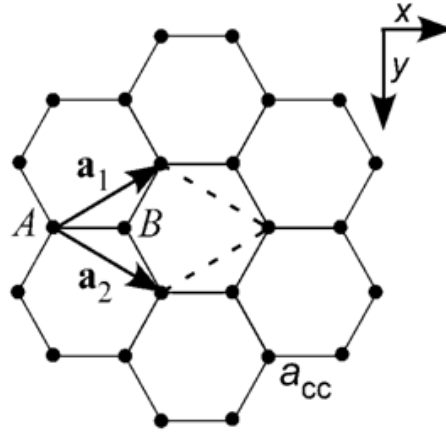
Figure 1-1: Schematic diagram of graphene ; a_1 and a_2 are the lattice vectors.

A SWNT is geometrically considered as a single graphene sheet rolled into a cylinder. Its structure is generally indexed by its Chiral vector $\mathbf{C_h}$ as defined by the circumferential vector $\overrightarrow{AA'}$ which starts and ends on the same lattice site on the SWNT and is brought back to the basic graphene sheet as shown Figure 1-2. The circumferential vector is defined as linear combination of basis vectors $\mathbf{a_1}$ and $\mathbf{a_2}$ of the hexagonal honey comb lattice with (Buchs, 2008).

$$C_h = na_1 + ma_2 \tag{1.1}$$

Thus, the geometry of a SWNT is described by the pair of integers (n, m) called the Chiral indices where diameter of tube D can be defined as

$$D = \frac{|C_h|}{\pi} = \frac{a}{\pi} \cdot \sqrt{n^2 + nm + m^2} \tag{1.2}$$

Where a is a lattice constant of the honey comb lattice: $a = \sqrt{3} \cdot a_{CC}$ ($a_{CC} \approx$ 1.42 Å is the C-C bond legth). The chiral angle θ which is defined as the angle between C_h and the zigzag direction of graphene sheet parallel to a_1 can be written as:

$$cos\theta = \frac{C_h \cdot a_1}{|C_h||a_1|} = \frac{2n + m}{2\sqrt{n^2 + m^2 + n \cdot m}} \tag{1.3}$$

As the graphene lattice has hexagonal symmetry, the possible values of θ are in the range of $0 \leq \theta \leq 30$ and the complementary angle between the tube axis and zigzag direction $\Phi = 30^0 - \theta$ is shown in Figure 1-2. If $\Phi = 30^0$, (n,0) is a type of zigzag. On the other hand, if $\Phi = 0^0$, (n,n) is a type of arm-chair. The unit cell of CNT is

described by Chiral vector C_h and the translation vector T perpendicular to C_h. The translational vector T is the smallest graphene lattice which is defined the translational period R along the tube axis and can be evaluated as $T = r_1 a_1 + r_2 a_2$ with

$$r_1 = \frac{2m + n}{d_R} ; r_2 = -\frac{2n + m}{d_R} \qquad (1.4)$$

where d_R is the greatest common divisor of (2m+n) and (2n+m). The Norm of T is given by:

$$|T| = \frac{3a_{cc}\sqrt{n^2 + m^2 + n.m}}{d_R} \qquad (1.5)$$

The unit cell of CNT is built by a cylindrical surface with height $|T|$ and diameter D, having number of atoms:

$$N_c = \frac{4(n^2 + m^2 + nm)}{d_R} \qquad (1.6)$$
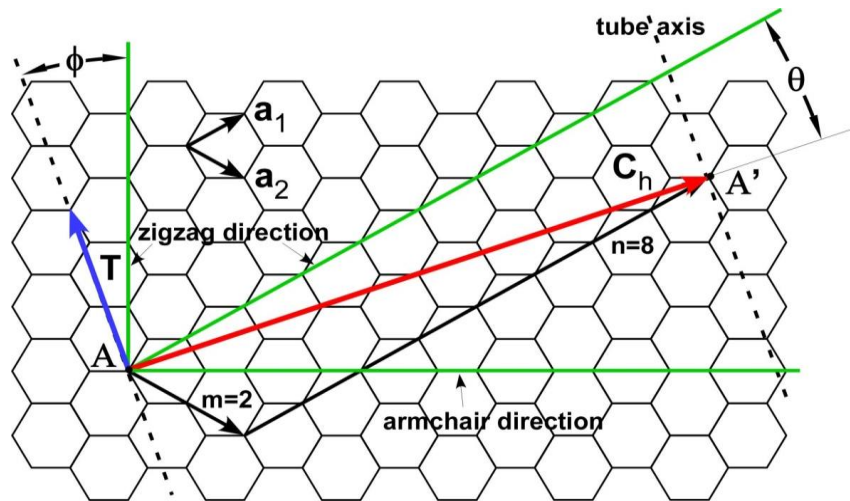
Figure 1-2: Graphene honey comb lattice with Chiral vector $C_h = na_1 + ma_2.$

and Translation vector **T.** A metallic (8,2) Chiral SWNT is illustrated in this figure (Buchs, 2008; Fig.1.1).

Generally, on the basis of indices n and m, nanotubes can be defined in such a way that if m=0, the nanotubes are called zigzag nanotubes and if n = m, nanotubes are called arm chair nanotubes. Otherwise, they are called Chiral nanotubes. For given nanotube indices (n,m) if n = m + 3k (where k is positive integer including zero), the nanotube is metallic otherwise it will be semiconducting.

1.2.   Literature Review

A considerable amount of literature has been published on Graphitic materials. In 1956, Yoshimori and Kitano performed the first study of lattice vibration of graphite. Subsequently, Young and Kopple (1965) presented a model for the reactor graphite which was based upon the previous Yoshimiri and Kitano bond bending and stretching model. It was considered the best model in primary studies of graphite.

In 1972, Nicklow et al. investigated normal modes of vibration of graphite lattices for high quality pyrolytic graphite by using coherent inelastic neutron scattering. The axially Symmetric model was presented to best fit the experimental dispersion data and described the data on low q {phonon wave number}, low frequency modes in the (1 0 0) direction. In 1973, Ross also studied the modes of vibration in polycrystalline graphite using inelastic neutron scattering at temperatures up to 1920 ^{0}C.

In 1995, Kresse et al. performed an ab initio study to investigate the dispersion relation of diamond and graphite. In this study, the supercell approach and local density approximation was used and found to agree with neutron inelastic data for low energy modes. In this study, high optical modes were also matched with reflection energy loss spectroscopy. In 2003, Dubay and Kresse performed an ab initio calculation of the phonon dispersion relation for single wall arm chair nanotubes and zigzag nanotubes. In this paper, the zone folding method was used to calculate dispersion relation of an isolated graphite layer. Discrepancies between the theory and experiment were found in this research work.

In 2004, Wirtz and Rubio reviewed the ab initio calculation of graphite and graphene by using the LDA and GGA approaches of density functional theory. On comparing both ab initio approaches the modes of vibration for the GGA approach were found to be close to the experimental predictions. The calculated values of frequency in the GGA approach were also found to be lower than the LDA approach.

In 2005, Mounet and Marzari studied the structural, vibrational and themodynamical properties of diamond, graphite and derivatives using density

functional perturbation theory (DFPT) in the Generalized Gradient Approximation (GGA). The low frequency modes of vibration for the graphite system were studied but these modes of vibration needed further explanation.

In 2007, Piscanec et al. found two Kohn anomalies in the highest optical phonon branch at Γ and K points of Brillouin Zone. The ab initio DFPT-GGA method was used in order to study the dispersion curve for graphite system. In 2008, Zimmermann et al. developed the force constant model to describe the lattice dynamics of Graphene and CNT(10,10). A set of parameters was introduced to calculate the phonon dispersion of graphene by fitting the ab initio dispersion. Vibrational modes of special carbon nanotubes were obtained by folding the two dimensional (2D) dispersion of graphene.

In 2008, Lazzeri et al. found electron-phonon coupling of selected phonon modes for graphene and graphite. In this study, long range electron-electron interaction was introduced using Green's function approaches based on the screened electron-electron interaction. These interactions would be neglected in GGA and LDA approaches.

In 2008, Falkovsky calculated the dispersion curve of graphene with interaction between three neighbours in the frame work of the Born-von Karman model. In this work, values of force constant were found by fitting the frequencies at critical points and elastic constants were also measured for the graphite system.

In 2008, Yan et al. performed the ab initio study of monolayer and a few layers of graphite using LDA in the frame-work of the DFPT. It was reported that optical modes can shift their frequency in bilayer and trilayer graphite relative to single layer graphite. In this study, differences are found between the ab initio theoretical and available experimental studies of graphite.

In 2009, Perebeinos and Tersoff studied the phonon for the graphene system using the valence force model. This study was compared with the previous ab initio investigation and experimental results for graphene.

In 2009, Tewary and Yang constructed the parametric inter atomic potential based on the Tersoff-Brenner potential model. In this study, the range of interaction

of each atom was extended up to four atoms for the graphene system. The parameters of potential were obtained by fitting the calculated values to the cohesive energy, lattice constants and phonon frequencies of graphene. The potential has been used to study the flexural rigidity of graphene. Nika and Balandin (2012) described the optical phonons by counting number of atomic planes in Raman experiment with few layer graphene and acoustic phonons which are responsible as heat carriers in the graphene. In recent studies, Paulatto et al. (2013) used the DFPT to analyse the phonon anharmonic broadening and thermal conductivity. In this study, it was found that broadening in graphite and bilayer graphene is very similar to graphene.

It is becoming increasing difficult to ignore the weak VDW interaction in graphitic materials especially sp^2 bonded graphite. So far very few dispersion corrected studies have been performed to study the structure and dynamical properties of graphite by using density functional theory. Previously the GGA was considered a more reliable approach to study the weakly bonded system. Recently semi-empirical dispersion corrections have been introduced in CASTEP {Cambridge Serial Total Energy Package} code (Clark et al., 2005). In the present study, we used the semi empirical dispersion scheme along with the GGA rather than just using the LDA. These types of study of the graphitic materials still were not found in literature. The purpose of this ab initio study, therefore, was to investigate the effect of dispersion correction on the structural and vibrational properties of the graphite system. These dispersion corrections have improved the prediction of structural properties. The dispersion corrected schemes, especially the TS scheme (Tkatchenko and Scheffler, 2009) produce accurate modes of vibration using ab initio methods. This approach reduces the computation time compared with semi-local GGA-PBE functional so it is a more efficient way to calculate the dynamical properties of graphite as well.

However, ab initio methods use direct solution of large sets of quantum wave functions in Density Functional Theory (DFT). The results generated from these calculations are extremely accurate and approach the reality of the system via the mathematics or solutions of quantum mechanics. The methods of ab initio phonon frequency fall into two broad classes: the linear response approach and the direct approach. Many physical properties depend upon a system response to some form of

Perturbation. Density functional Perturbation theory (DFPT) is particularly powerful and is a flexible tool in calculation of phonon, Raman Intensities and infra-red absorption. System responses to external perturbation may be calculated using DFT with addition of some perturbing potential. These types of calculations need large computational efforts. However, the second category is based on the Supercell Finite Displacement Approach. This is an efficient and better way to calculate the phonon in large number of systems. This includes the interactions of large number of atoms. This method is used in the present vibrational studies about the graphitic materials.

Over the next 30 years, two major issues may be decreasing the world supply of fossil fuels and the increasing rate of global warming and climate change. Therefore, major attention has been paid towards the hydrogen manufacture and storage (Yurum et al., 2009). The hydrogen can be used as an alternate and renewable source; it may be obtained from water. However efficient storage of the hydrogen for mobile applications is still a vital challenge for the scientific and industrial community (Jena, 2011).

Numerous works have been published on carbon as hydrogen storages as carbon is mostly used as a catalyst support and in fuel cell electrodes. In 1997, Dillon et.al. performed the first study of the use of the Single Wall Nanotubes (SWNT) as hydrogen storage materials. It was reported 10 wt. % of hydrogen in SWNT, this was measured using the temperature desorption programme. The large quantity of gas can be adsorbed in the pores of carbon nanotubes. After this study, researchers developed an interest to use carbon nanotubes as hydrogen storage.

For instance, in 1998, Chambers et al. studied the hydrogen-storage abilities of graphitic nano fibres and alkali doped multi-walled graphite. In 2001, Yildrim et.al. performed an ab initio study of a fully exo-hydrogenated zigzag and armchair single wall carbon nanotubes. They found that zigzag nanotubes were more likely to have significant sp^3 structure as compared with arm chair nanotubes. It means that the binding energy of zigzag is always lower than arm chair nanotubes with the same radius. In 2001, Chan developed a mechanism for the dissociation of hydrogen molecule on CNT using density functional theory. In this ab initio study; pressure was used to dissociate H-H bonds and form C-H bonds. In 2002, Khare et al. found

that atomic hydrogen covalently binds with the carbon atoms of nanotubes and the formation of C-H bond was confirmed by the IR stretching mode.

In 2003, Schimmel et al. claimed the storage capacities of carbon materials were closer to 2.5 wt. %. In 2004, Bashkin studied the thermal stability of hydrogenated SWNT under the pressure of 9 GPa at T=500 ^{0}C. It was reported that C-H peaks were found in the region between 2860 cm^{-1} to 2920 cm^{-1} using IR spectroscopy. In 2005, Nikitin et al. reported that C-H bonds weakened with increase in radius for hydrogenated SWNTs. They also found that 65 $\pm$15 at. % of the carbon atoms in SWNTs can be hydrogenated to form C-H bonds. This corresponds to hydrogen capacity 5.1$\pm$2.1 wt. %. It was also found that hydrogenated CNTs were stable at room temperature and hydrogen was released by heating to 600^{0}C. Thus hydrogenation and dehydrogenation processes were found to be reversible. It was mentioned that a stable C-H bond can break in the well-defined carbon nanotubes between the ranges of temperature 50-100^{0}C. In 2005, Park et al. studied the atomic and electronic structures of hydrogen–chemisorbed single wall CNTs. In this study they investigated the relative stability of the various hydrogen adsorption geometries with coverage. The band gap of carbon nanotubes also changed with the hydrogen coverage, independent of the metallicity of nanotubes. This may be caused by sp^3 hybridization in hydrogenated CNTs.

In 2006, Zhang et al. reported the hydrogenation of SWNT by means of hydrogen plasma treatment. It was reported that the vibrational frequency of chemisorbed hydrogen was found to be 2920 cm^{-1} corresponding to sp^3 C-H stretching or asymmetric stretching of sp^3 CH$_2$ group. In this study, each hydrogen atom was externally attached to carbon through the chemisorbtion process and the calculated value of the gravimetric density was about 7.74 wt. %.

In 2006, Bazhenov reported 5.4 wt. % of hydrogen in SWNT at a hydrogen pressure of 50 kbar at 500 ^{0}C. The C-H mode was found at the value of 2845 cm^{-1} by studying the optical transmission spectra. In 2008, Nikitin et al. found that SWCN with diameter 2nm could be 100% hydrogenated and the nanotubes were stable at room temperature with hydrogen storage capacity calculated at 7 wt. %. In this study, it was reported that most of the C-H bonds formed on the nanotube surface can be dissociated in the temperature range 200-300 ^{0}C. It was also found that

hydrogen desorption was largely controlled by the reaction kinetics due to large activation barriers of H_2 formation from stable H pairs adsorbed on the SWCN.

Tokura et al. (2008) investigated adsorption of atomic hydrogen on SWNTs using spectroscopy. This study suggests that the hydrogen adsorption which creates the structure deformation from sp^2 to sp^3 like bonding depends on the diameters of SWCNTs. Yoshihara et al. (2008) reported the interaction of hydrogen with SWNTs using an SWNT thin film sensor and thermal desorption spectroscopy. It was found that adsorption of atomic hydrogen on SWNTs shows non- activated and thermal adsorption states due to first order kinetics, where non-activated adsorption is dominated. The desorption of hydrogen molecules was also found to follow the first order kinetics.

In 2009, Bhowmick et al. performed studies of Pt-SWNTs to investigate the spill- over effect for the hydrogenation of Pt-SWNT composite using hydrogen molecules. It was also reported that SWNTs store the hydrogen by chemisorption to form stable C-H bond. It was also reported that C-H bond formation can be probed using the spectroscopic techniques during the interaction of hydrogen with SWCN. Recently, it was also reported that chemisorption of two hydrogen atoms on the exterior side walls of carbon ad-dimer defective armchair SWCNTs was thermodynamically more stable than the pristine nanotubes with two hydrogen atoms chemisorbed (Wang et al., 2010).

In all the studies mentioned in previous paragraphs about chemisorbed hydrogenated carbon nanotubes, the C-H bond formation was not properly studied using the density functional theory. Hydrogen release temperature was not yet properly investigated in zigzag and arm chair hydrogenated CNTs. Therefore, we performed the systematic ab initio study of hydrogen release temperature in hydrogenated CNTs.

1.3.   Aims and Objectives of the Work

Research about the structural and dynamical properties of graphite system cannot be completed without including the VdW (Van der Waals) interactions due to weakly intermolecular forces between layers of graphite. These VdW interactions have a strong influence on properties of graphite.

In this project, structural and dynamical properties of graphite system were performed using dispersion corrections like G06 and TS schemes (Grimme, 2006, Tkatchenko and Scheffler, 2009) along with density functionals. Local density functional (LDA) and generalized gradient approximation (GGA) were also used to investigate the properties of single layer and double layers graphite. The research work was carried out to compare the properties of graphite with density functionals and incorporation of these functionals with dispersion corrections.

The following are the main objectives of performing this study:

- To investigate the structural and vibrational properties of graphite using density functional theory (DFT) and density functional theory with dispersion corrections (DFT-D) methods.
- To study the structural and vibrational properties of rhombohedral graphite system using DFT-D functional.
- To obtain the binding energies and band gaps of hydrogenated zigzag and armchair CNTs.
- To obtain the complete vibrational information of hydrogenated carbon nanotube by means of computational vibrational density of states and dispersion curve.
- To utilise the results of computational calculations and statistical thermodynamics to predict the hydrogen releasing temperatures in hydrogenated CNTs.

The binding energies and band gaps have been found for zigzag and armchair CNTs using PBE-GGA functional. The band gap opening in CNTs are important due to its use in nano-electronics. Hydrogenation of nanotubes is vital in the modification of electronic structure for the device applications. These properties have been

compared with respect to diameters of CNTs. The hydrogenated CNT was explored to investigate the C-H mode using vibrational density of states. The prediction of hydrogen releasing temperature was done to find the stability of a C-H bond in hydrogenated CNTs using the density functional theory and statistical thermodynamics. This is the first extensive study of hydrogen release temperatures in CNTs.

1.4.   Outline of Thesis

In the first chapter, inspirations and motivations have been discussed to perform the current study of graphitic materials. In the second chapter, the origin of density functional theory has been described by using Hartree-Fock approximation and Born Oppenheimer Approximation. The density functionals and influence of dispersion corrected schemes on density functionals are described and their limitations also pointed out.

The third chapter explains the role of the plane wave pseudopotential methods in order to solve the Kohn-Sham equations for periodic systems. Various methods are described to solve the Kohn-Sham equations in order to get the ground state energy.

The fourth chapter provides the insight about the methods of the phonon calculations. Statistical partition functions are also described to perform the free energy calculations. These free energy calculations will be utilized to find the hydrogen release temperatures.

The fifth chapter is about the results and discussion in which structural and dynamical properties of graphite and graphene have been described by using ab initio methods. The VdW dispersion corrections are important factors in this study. The semi empirical ab initio methods are successful and efficient tools to explain the structural properties.

In the sixth chapter, the major application of CNT as hydrogen storage has been studied using density functional theory and statistical partition functions. Following the geometry optimization in zigzag and arm chair CNTs, binding

energies of chemisorbed hydrogenated CNTs have been studied. The dependence of band gaps of hydrogenated CNTs on diameters are determined using the PBE-GGA functional. The vibrational density of states has been studied for hydrogenated CNTs in order to evaluate the C-H modes of vibration. The partition functions have been used to determine the translational and rotational free energies of hydrogen molecules. Hydrogen release temperatures in zigzag and arm chair CNTs have been predicted using the thermodynamical calculations as implemented in CASTEP code.

Finally, the seventh chapter is about a brief summary of the work and accuracy of the modelling that has been described. Some suggestions and recommendations have been made regarding further research on graphitic materials.

Chapter 2. Theoretical Background

2.1.   Introduction

One significant need is to solve the quantum mechanical wave function for the system. These solutions are useful to explain the properties of ions or atoms. This chapter gives a brief description about the methods to solve the Schrodinger wave equation. In particular, we describe how to solve the wave function in the Born-Oppenheimer approximation (Born and Oppenheimer, 1927) and Hartree-Fock formalism (Hartree, 1928, Fock, 1930). We then describe the Thomas-Fermi approximation (Thomas, 1926, Fermi, 1928). Finally, we describe Density functional theory (DFT) as developed by Kohn-Sham (Kohn and Sham, 1965). Exchange and correlation functionals play fundamental roles in density functional theory but exact forms of these functionals are still unknown. Dispersion correction schemes introduce the VdW interactions in weakly bonded systems. These schemes have been recently employed correctly in CASTEP 7.0 code (Clark et al., 2005) to add the long range interactions for layered systems such as the graphite.

2.2.   Many –Body Problem Interacting System

Atomic systems are always described in terms of interactions between two types of particle: positive nuclei and negative electrons. The Schrodinger wave equation describing the motion can be written as

$$\hat{H}\Psi = E\Psi \tag{2.1}$$

with Ψ as the many body wave function, E as the energy of the system and $\hat{H}$ as the Hamiltonian describing this interaction which can be written as:

$$\widehat{H} = -\sum_{I} \frac{\hbar^2 \nabla_{RI}^2}{2M_I} + \frac{1}{2}\sum_{I \neq J} \frac{Z^2 e^2}{|R_I - R_J|} - \sum_{i} \frac{\hbar^2}{2m}\nabla_{ri}^2$$
$$+ \frac{1}{2}\sum_{i \neq j} \frac{e^2}{|r_i - r_j|} - \sum_{i,I} \frac{Ze^2}{|r_i - R_I|} \tag{2.2}$$

Where the nuclei have the positions R_I, mass M and charge Z and electrons are with positions r_i, mass m and charge e. The same term i.e. I=J or i=j are ignored to avoid the self-interaction.

2.3.   Born-Oppenheimer Approximation

Born and Oppenheimer (1927) recognised that the atomic nuclei are more massive particles than the electrons and, as a result, their velocities are much lower. The nuclei can be considered as stationary with electrons following the motion of the nuclei. The Hamiltonian for the electronic wave function is given by

$$\widehat{H}_{el} = -\frac{\hbar^2}{2m}\nabla_{ri}^2 + \frac{1}{2}\sum_{i,j} \frac{e^2}{|r_i - r_j|} - \sum_{i,I} \frac{Ze^2}{|r_i - R_I|} \tag{2.3}$$

The second term in equation (2.3) is the electron-electron interaction term, a repulsive Coulomb interaction due to the negative charge of the electron.

For a system in the electronic state, Ψ, the measured energy , E, will be an upper bound to the true ground state energy (Parr and Yang, 1989;p.05);

$$E[\Psi] \geq E_0 \tag{2.4}$$

The average of many measurement of the energy $E[\Psi]$ is given by the relation

$$E[\Psi] = \frac{\langle\Psi|\widehat{H}|\Psi\rangle}{\langle\Psi|\Psi\rangle} \tag{2.5}$$

Each measurement of energy provides one of the eigenvalues of the $\widehat{H}$ and full minimization of the functional $E[\Psi]$ with respect to all allowed N-electron wave functions will give the true ground state Ψ_0 and energy E_0 .

2.4.   Quasi Particles

The result of placing one electron into a uniform distribution of electrons creates a hole in the charge density from all other electrons as similar charge electrons repel each other. The exchange interaction arises due to the exclusion

principle, electron with parallel spin tend to avoid each other. The result of this repulsion is that there is a reduction in the probability of finding an electron near to a given electron as shown in Figure 2-1. This is known as the exchange-correlation hole. The charge of the exchange-correlation hole is equal to minus one electron and therefore, viewed from a distance each electron-hole pair (or the quasi particle) acts like a charge neutral particle (Sutton, 1996; p.155). Charge neutral particles do not interact at a distance and their motion is essentially independent. The electron and its exchange-correlation hole are inseparable and they move through the system as a single entity which is called a quasi particle.
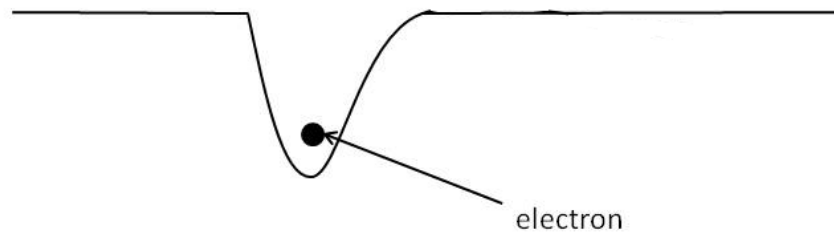
Figure 2-1: The electron-hole pair–the electron causes a dip in the charge distribution of all other electrons.

2.5.   Hartree Approximation

Hartree (1928) expressed the independent quasi particle view of the electron that only sees the average field generated by the other electrons in the system. This was in order to approximately solve the electron-electron interaction in equation by rewriting the many body wave function as a product of single electron wave functions, $\phi_i(r_i)$.

$$\Psi^H(r_1, r_2, \ldots \ldots r_N) = \prod_{i=1}^{N} \phi_i(r_i) \tag{2.6}$$

The single particle states can be normalised to unity and the energy of the system can be written as (Kaxiras, 2003; p.44).

$$E^H = <\Psi^H|\hat{H}|\Psi^H>$$

$$= \sum_i \left\langle \phi_i \left| \frac{-\hbar^2 \nabla_r^2}{2m_e} + V_{ion}(r) \right| \phi_i \right\rangle \tag{2.7}$$

$$+ \frac{e^2}{2} \sum_{i,j(i \neq j)} \left\langle \phi_i \phi_j \left| \frac{1}{|r - r'|} \right| \phi_i \phi_j \right\rangle$$

Applying the variational principle we obtain single particle Hartree equation:

$$[\frac{-\hbar^2 \nabla_r^2}{2m_e} + V_{ion}(r) + e^2 \sum_{j \neq i} \langle \phi_j | \frac{1}{|r - r'|} | \phi_j \rangle] \phi_i(r) = \varepsilon_i \phi_i(r) \tag{2.8}$$

Where the constraints ε_i are Lagrange multipliers that take into account the normalization of states.

In order to solve the single particle Schrodinger equation for each $\phi_i(r_i)$, all other states $\phi_j(r_j)$ must be known. This requires a self-consistent method of solution starting with an initial choice of the functions and continuing until convergence. If the trial functions are orthogonal and this orthogonality should be maintained throughout the self-consistent cycle then the final functions will look like single-particle states. Each electron will experience the ionic potential $V_{ion}(r)$ and the potential due to all the other electrons, this is called the Hartree potential.

$$V_i^H(r) = e^2 \sum_{j \neq i} \langle \phi_j | \frac{1}{|r - r'|} | \phi_j \rangle \tag{2.9}$$

This mean field approximation includes only the Coulomb repulsion between electrons. The aim is to reduce the many-electron problem to an effective one-electron form.

2.6.   Hartree-Fock Theory

Fock (1930) improved the Hartree model and described the way to make the wave function anti symmetric with respect to the exchange of electrons and therefore satisfy the Pauli exclusion principle (Pauli, 1925). This could be achieved by adding and subtracting all possible permutations of the Hartree product. This wave function is explained by Slater in the form of the determinant of the matrix (Slater, 1930).

$$\Psi_{HF} = \frac{1}{\sqrt{N!}} \begin{vmatrix} \phi_1(r_1) & \phi_2(r_1) \ldots \ldots \ldots \phi_N(r_1) \\ \phi_1(r_2) & \phi_2(r_2) \ldots \ldots \ldots \phi_N(r_2) \\ \ldots \ldots \ldots \ldots \ldots \ldots \ldots \ldots \ldots \ldots \ldots \ldots \ldots \\ \ldots \ldots \ldots \ldots \ldots \ldots \ldots \ldots \ldots \ldots \ldots \ldots \ldots \\ \phi_1(r_N) & \phi_2(r_N) \ldots \ldots \ldots \phi_N(r_N) \end{vmatrix} \tag{2.10}$$

The Hartree-Fock described the methods to solve the orthogonal orbtials, ϕ_i , that minimize the ground state energy for this form of Ψ. The single-particle wave equations from the variational method now written as:

$$\left[\frac{-\hbar^2\nabla_r^2}{2m_e} + V_{ion}(r) + V_i^H(r)\right]\phi_i(r) - e^2\sum_{j\neq i}\left\langle\phi_j\left|\frac{1}{|r-r'|}\right|\phi_i\right\rangle\phi_j(r) = \varepsilon_i\phi_i(r) \qquad (2.11)$$

This has one extra term compared with the Hartree's equation (2.8), known as the exchange term $V_i^x(r)$.

2.7.   Density Functional Theory

The DFT approach involves writing the total energy of a system of interacting electrons in terms of the density of charge n(r) rather than the many body wavefunction. The density has an advantage as it deals with function of three variables, i.e. three Cartesian directions rather than the dealing with many-body wave functions of the system which depend on 3N variables.

2.8.   The Thomas –Fermi Model

In the earliest form of density functional theory, Thomas (1926) and Fermi (1928) proposed a model to describe the energy as a simple function of density. The energy of the system is then given by:

$$E_{TF}[n(r)] = \int \frac{3}{10}(3\pi^2)^{2/3}.n(r)^{5/3}dr$$
$$+ \int V_{ext}(r)n(r)dr + \frac{1}{2}\iint\frac{n(r)n(r_1)}{|r-r_1|}drdr_1$$

$$(2.12)$$

= Kinetic Energy + External Potential (due to nuclei)

+ Electron- Electron Interaction

This model is qualitatively correct for atoms but does not give a binding energy for molecules and fails to explain the exchange and correlation effects.

2.9.   Hohenberg-Kohn Theorems

Hohnberg and Kohn (1964) showed that the external potential is uniquely determined by the electron density only. Therefore, the Hamiltonian, and hence all ground state properties, are determined solely by the electron density.

In other words, all physical properties of a system can be determined by the charge density as the expectation value of an operator that is a unique functional of the ground state charge density, $n_0(r)$.

The Hamiltonian uniquely determined by $n(r)$, is also defined as the sum of the kinetic energy T, the external potential V_{ext} and the electron-electron interaction potential V. In order to prove the Hohenberg and Kohn theorem, we will start with the Schrodinger equations for two systems with potential, V_{ext} and V'_{ext} that differ by more than a constant. These systems described by Hamiltonians H and H', have ground state energies E_0 and E'_0 and charge densities $n_0(r)$ and $n'_0(r)$ respectively (Taylor and Heinonen, 2002; p.186). The ground state wave functions for Hamiltonian H and H' are Ψ_0 and Ψ'_0 respectively. According to the variational principle:

$$E_0 = \langle \Psi_0 | H | \Psi_0 \rangle < \left\langle \Psi'_0 \; \middle| H \middle| \Psi'_0 \right\rangle \tag{2.13}$$

Where:

$$\left\langle \Psi'_0 \; \middle| H \middle| \Psi'_0 \right\rangle = \left\langle \Psi'_0 \middle| H' \; + V_{ext} - V'_{ext} \middle| \Psi'_0 \right\rangle \tag{2.14}$$

$$= E_0{}' + \int n'_0(r) \left[V_{ext} - V'_{ext} \right] dr \tag{2.15}$$

Therefore:

$$E_0 < E_0{}' + \int n'_0(r) \left[V_{ext} - V'_{ext} \right] dr \tag{2.16}$$

It can also be shown similarly that

$$E_0{}' < E_0 + \int n_0(r) \left[V'_{ext} - V_{ext} \right] dr \tag{2.17}$$

 If we assume that $n_0(r)$ and $n'_0(r)$ are equal and combine the above two equations

$$E_0 + E_0{}' < E_0 + E_0{}' \tag{2.18}$$

This is clearly not true and hence, E_0 and $E_0{}'$ must be different as the charge densities cannot be equal. We have established that two non-degenerate ground states always lead to different ground state densities.

In principle, E_0 can be found by varying the n(r) to minimize $E[n(r)]$, if $E[n(r)]$ is known. The energy functional can be written in terms of the external potential and another functional $F_{HK}[n(r)]$ which includes the kinetic energy and electron-electron terms:

$$E[n(r)] = F_{HK}[n(r)] + \int V_{ext} n(r) dr \tag{2.19}$$

Where

$$F_{HK}[n(r)] = \langle \Psi[n]|T + U|\Psi[n]\rangle \tag{2.20}$$

Hohenberg and Kohn also observed that if one can find $E[n(r)]$, then true ground-state density $n(r)$ minimizes it. In equation (2.19), $F_{HK}[n(r)]$ comprise of all internal energies of the interacting particle systems. This is also called universality of total energy functional. It should be noted that $E[n(r)]$ is not known.

2.10. Kohn-Sham formalism

The basic idea in Kohn and Sham (1965) formalism is to use a non-interacting "reference" or auxiliary system and to look for an external potential $V_S(r)$ such that the non-interacting system has the same ground state density as the real interacting system.

The Hamiltonian for this system can be written as

$$H_s = T_S + V_s \tag{2.21}$$

According to Hohenberg-Kohn theory, the energy of this system is described as:

$$E[n(r)] = T_s[n(r)] + \int V_s(r)n(r)dr \tag{2.22}$$

As the particles in this system are non-interacting, the exact wave-function can be separated into normalized single-particle states, $\phi_i(r)$, and the charge density can be written as (Taylor and Heinonen, 2002 ; p.187):

$$n(r) = \sum_{i=1}^{N} |\phi_i(r)|^2 \tag{2.23}$$

The energy functional for the real system can be described to include the kinetic energy $T_s[n(r)]$ of the non-interacting system

$$E[n(r)] = T_s[n(r)] + \frac{e^2}{2} \iint \frac{n(r)n(r')}{|r - r'|} dr dr' + \int V_s(r)n(r)\, dr + E_{xc}[n(r)] \tag{2.24}$$

$E_{xc}[n(r)]$ is known as the exchange-correlation energy. According to the Hohenberg and Kohn theorem, the charge density that minimizes $E[n(r)]$ is the ground state density.

Application of the variational principle leads to the Kohn-Sham equations;

$$[-\frac{\hbar^2}{2m_e}\nabla_i^2 + V_H(r) + V_{ext}(r) + V_{xc}(r)]\,\phi_i(r) = \epsilon_i\phi_i(r) \qquad (2.25)$$

Where V_{xc} is called the exchange-correlation potential defined as $\frac{\partial E_{xc}[n(r)]}{\partial n(r)}$. These equations need to be solved self-consistently and the solution gives the Kohn-Sham eigenvalues ϵ_i and electron wave functions.

The exact form of the $E_{xc}[n(r)]$ functional is not known but several approximations are available. The Kohn-Sham formulation thus achieves in transforming the N-body problem in to N single-body problems. It is worth mentioning that formally there is no physical interpretation of these single Kohn-Sham eigen values and orbitals, they are solely mathematical artefacts that support the determination of the true ground state density.

2.11. Functionals

In the Kohn-Sham equations, we simply replace the fully interacting system with a non-interacting system that produces the same ground state density. As the Kohn-Sham kinetic energy is not the true kinetic energy, we need to define the exchange and correlation energy as (Tulip, 2005);

$$E_{xc}[n(r)] = T[n(r)] - T_s[n(r)] + E_{ee}[n(r)] - E_H[n(r)] \qquad (2.26)$$

where $T_s[n(r)]$ and $E_{ee}[n(r)]$ are the exact kinetic and electron-electron interaction energies respectively. Physically this term can be explained as consisting of the contributions of detailed correlation and exchange to the system. The equation (2.25) ensures the exact form of the Kohn-Sham formulation. However, the actual form of $E_{xc}[n(r)]$ is still not known. Thus we need to develop an approximate functional based upon the electron density.

2.12. Local Density Approximation

The Local Density Approximation (LDA) states that the contribution to the exchange-correlation energy from an infinitesimal volume dr is same as a homogenous electron gas (jellium) with the same density at r. Therefore, by assuming this approximation, the only need is the exchange and correlation energy of the homogenous electron gas as a function of density. In this system the electrons are

subject to a constant potential and thus the charge density is constant (n_0). Hence the exchange and correlation energy E_{xc}^{hom} can be written as:

$$E_{xc}^{hom} = N\varepsilon_{xc}^{hom}(n_0) = \int n_0 \varepsilon_{xc}^{hom}(n_0)dr \qquad (2.27)$$

Where N is the number of electrons and $\varepsilon_{xc}^{hom}(n_0)$ is the exchange-correlation energy per unit volume.
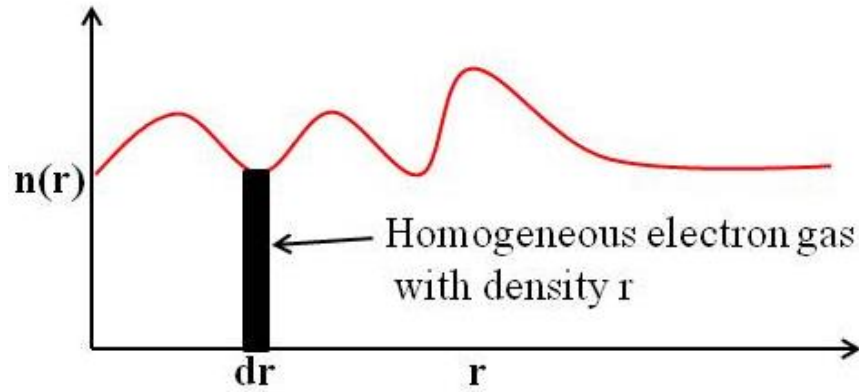
Figure 2-2: Local density equivalent to uniform electron gas is being considered in the region dr by Local density approximation.

This leads to the exchange-correlation energy of the system being expressed as:

$$E_{xc}^{LDA} = \int n(r)\varepsilon_{xc}^{hom}[n(r)]\,dr \qquad (2.28)$$

and the exchange-correlation potential is now:

$$V_{xc}^{LDA}(r) = \frac{\delta E_{xc}^{LDA}}{\delta n} = \varepsilon_{xc}^{hom}(n(r)) + n(r)\frac{\delta \varepsilon_{xc}^{hom}(r)}{\delta n(r)} \qquad (2.29)$$

The LDA is usually parameterized by separating the energy into the exchange energy and correlation energy. The exchange energy is a simple analytical form and comes from the Dirac's exchange formula (Dirac, 1930) for the homogenous electron gas of density n.

$$E_{x}^{LDA} = -\frac{3}{4}\left(\frac{3}{\pi}\right)^{1/3}\int n(r)^{4/3}\,dr \qquad (2.30)$$

The correlation energy can be interpolated based on series of quantum Monte Carlo calculations obtained by Ceperley and Alder (1980) from the exchange and correlation of the electron gas.

      This method is considered to provide suitable results for slowly varying density systems like nearly free electron metals. It also works better in the systems

where the charge density is rapidly varying. It is found to work reasonably well in semiconductors and insulators. However, LDA tends to overestimate the ground state energy density and bulk modulus; and underestimates the band gap as compared with experimental data. Therefore, the LDA provides unexpected results for narrow gap insulators and certain oxides. LDA also overestimates the weaker bonds such as hydrogen bonds.

2.13.   Generalized Gradient Approximation

The exchange-correlation energy becomes a functional of the charge density and the gradient of the density in the Generalized Gradient Approximation (GGA) method ;

$$E_{xc}[n(r)] = \int g[n(r), |\nabla n|]dr \qquad (2.31)$$

The gradient correction improves the accuracy of density functional theory when applied to homo-nuclear dimers, small molecules and bulk properties of transition metals (Jaun and Kaxiras, 1993).   Well established examples of the GGA approximation are the PW91 and PBE functionals (Perdew et al., 1996, Perdew and Yue, 1986).

The GGA functional provides a better overall description of the electronic sub systems than does the LDA functional. The LDA description tends to over bind atoms, so that the bond length and cell volume are usually underestimated by a few percent. GGA corrects this error but produces the slightly long bond lengths.

2.14.   Dispersion Corrected Functionals

The GGA-DFT methods fail to describe the long range electron correlations that are responsible for the dispersion interaction. This is due to the semi-local nature of the density functional, which is deficient in treating the long range electron correlations necessary to provide all the dispersive interactions, for example, the layers in graphite system.

Dispersion interactions (also known as VdW interactions or London forces) play a crucial role. London (1930) described the relationship between the electron

correlation and long range forces between the atoms. It was realized that although the time-average electron density around an atom or the non-polar molecule has no dipole moment, electron oscillations lead to deformations of the density resulting in transient dipole moment on the other atoms or molecules by distorting the electron density. The existence of two dipoles creates a net interaction (Scholl and Steckel, 2009;p.225). Three schemes have been introduced to study the dispersion corrections in density functional theory. The first, known as the OBS scheme was introduced by Ortmann et al. (2005) in which the London relation has been used to calculate the dispersion coefficients from experimentally measured polarizabilities and ionization potentials. Grimme (2006) employed the scheme which was effective for transferability and successfully applied to study adsorption problems. The Tkatchenko and Scheffler (2009) scheme provided the relationship between the polarizability and volume, this scheme also explains the relative variation in dispersion coefficients of differently bonded atoms (McNellis et al., 2009).

London (1930) showed that the general form of the interaction between two spherically symmetric atoms at large distance was:

$$V^{dispersion} = \frac{C}{r^6}$$

Where r is the distance between the atoms and C is a collection of physical constants. The total energy expression can be written as

$$E_{DFT-D} = E_{KS-DFT} + E_{disp} \tag{2.32}$$

Where E_{KS-DFT} is the usual self-consistent Kohn-Sham energy as obtained from the chosen density functional and E_{disp} is an empirical dispersion correction given by

$$E_{disp} = -s_6 \sum_{i=1}^{N_{at}-1} \sum_{j=i+1}^{N_{at}} \frac{C_6^{ij}}{R_{ij}^6} f_{dmp}(R_{ij}) \tag{2.33}$$

Here, N_{at} is the number of atoms in the system, C_6^{ij} denotes the dispersion coefficient for the atom pair ij, s_6 is the global scaling factor that only depends on density functional used, and R_{ij} is an inter-atomic distance. In order to avoid near singularities for small R, a damping function f_{dmp} must be used, which is given by

$$f_{dmp}(R_{ij}) = \frac{1}{1 + e^{-d(\frac{R_{ij}}{s_r R}-1)}} \tag{2.34}$$

Where R is the sum of the atomic VdW radii, d is a parameter which controls the damping function steepness and s_r is called the scaling factor (Grimme, 2006) referred to as G06.

The default values of s_6 and d in the Grimme scheme are 0.75 and 20 with the PBE functional for the graphite system. These parameters are used to perform the optimized graphite structure calculations. However, in order to perform the vibrational studies, the values of s_6 and d can be adjusted for the graphite system in order to achieve the required frequency.

The better TS dispersion correction was applied by Tkatchenko and Scheffler (2009). In contrast to G06, the TS scheme is a parameter free non empirical method. The TS scheme replaces the s_6 by a constant factor ½. In this scheme, the scaling factor s_r is functional dependent. The default values for s_r and d are 0.94 and 20 for the TS scheme in the CASTEP 7.0 code. These values are sufficient for geometry optimization in graphite. However, values of s_r and d should be adjusted for vibrational properties of graphite. The approach to calculate the VdW radii is the same in both methods. However, a difference is found in determining the dispersion coefficients. The TS scheme is more self-consistent compared to the Grimme scheme in the sense that C_6 coefficients are calculated using the electron density of the system under study using the data for the free atoms (Admaska et al., 2012).

2.15. Summary

The problem of modelling a system of atoms becomes easier by separating the motion of the electron with that of ion cores and it is based on the assumption that electrons respond instantaneously to any change in nuclear positions. Therefore, electrons are usually treated as an independent particles travelling in an external nuclear potential and modelled by the single particle wave functions.

The energy of the system is a functional of charge density (which can be calculated from the electron wave functions) and the ground state-density can be obtained by minimising the energy with respect to charge density. These are the fundamentals of density functional theory.

The exchange-correlation energy which is required to solve the Kohn-Sham equations can be approximated by number of functionals. The local and semi-local functionals have limitations for the inter-layer bonded system and therefore dispersion corrected functionals have also been used.

Chapter 3. Computational Methods

3.1.   Introduction

For applications of the density functional theory, the Kohn-Sham equations need to be solved. This chapter describes the computational methods used to solve the Kohn-Sham equations. We would need to define an appropriate basis set to expand the wave functions and express the different parts of the Hamiltonian. The pseudopotential method can reduce the size of the basis set and therefore reduce the computational expense. For this purpose, the Cambridge Serial Total Energy Package CASTEP 7.0 (Clark et al., 2005) was developed by Clark et al. (2005) in order to study periodic systems. The CASTEP code deals with solving the ground state charge density and wave function for a given set of coordinates. The forces can also be calculated on ions to optimize the ionic positions and cell parameters to give a minimum energy configuration.

3.2.   Basis Sets

The Kohn-Sham equations can be solved by expanding the orbitals $\phi_i(r)$ in a set of N basis functions that can be written as:

$$\phi_i = \sum_{i=1}^{N} a_n \chi_n \tag{3.1}$$

Our purpose is to find the coefficients a_n needed to expand ϕ_i in a given basis set χ_n. We would require an infinite basis set for an exact solution, but in practice we can work with finite sets, trying to make it one that can generate a function that is close enough to ϕ_i.

Plane wave basis sets are used because of their analytic properties and their mathematical simplicity. Due to their periodicity, they are well suited to the calculations of periodic solids. In calculations of this work we have only used plane waves basis sets which are the independent of atom positions and species, unbiased.

3.3.   Plane Wave Basis Sets

Bloch (1928) introduced a wave function for periodic systems that can be written as a product of a wave –like function and a cell periodic part (Ashcroft and Mermin, 1976).

$$\phi_{nk}(\mathbf{r}) = e^{i\mathbf{k}.\mathbf{r}}u_{nk}(\mathbf{r}) \tag{3.2}$$

In solid state systems, the cell periodic part of the wave function can be expanded using a basis set of plane waves whose wave vectors are the reciprocal vectors of the crystal,

$$u_{nk}(r) = \sum_{G} c_{Gnk}\, e^{i\mathbf{G}.\mathbf{r}} \tag{3.3}$$

Thus each electronic wave function can be written as a discrete sum of plane waves:

$$\phi_{nk}(r) = \sum_{G} c_{Gnk}\, e^{i(\mathbf{k}+\mathbf{G}).\mathbf{r}} \tag{3.4}$$

The coefficients c_{Gnk} can be defined in terms of their Discrete Fourier Transforms (FFT):

$$c_{Gnk} = \frac{1}{N_{FFT}}\sum_{r} c_{rnk}\, e^{-i\mathbf{G}.\mathbf{r}} \tag{3.5}$$

$$\text{where } c_{rnk} = \sum_{G} c_{Gnk}\, e^{i\mathbf{G}.\mathbf{r}} \equiv u_{nk}(\mathbf{r})$$

This can be attained computationally using a finite 3D FFT grid, the size of which is marked by certain parameters of the system in question; $\mathbf{r}$ is a point in grid. The reciprocal lattice vectors $\mathbf{G}$ are defined by $\mathbf{G}.\boldsymbol{a} = 2\pi m,$ where $\boldsymbol{a}$ is the lattice vector of the crystal and m is an integer. n represents the band index number.

According to Bloch's theorem, the electronic wave function at each k-point can be expanded in terms of a discrete plane wave basis set. In principle, an infinite plane wave basis set is required for that purpose. However, the coefficients $"c_{Gnk}"$ for the plane waves with smaller kinetic energy $|\mathbf{k} + \mathbf{G}|^2$ are typically more important than those of large kinetic energy. A cut-off energy can be described in a

sphere for the reciprocal space by fixing the highest **G** vectors for the infinite basis set;

$$E_{cut} \geq \frac{\hbar^2 |\mathbf{k} + \mathbf{G}|^2}{2m_e} \tag{3.6}$$

Thus the plane wave basis set can be truncated to include only plane waves that have the kinetic energy less than some particular cut-off energy; this produces the finite basis set. Unfortunately, an error in the computed total energy results from this truncation. This error can be reduced by increasing the value of the cut-off energy. The Kohn-Sham equations can be obtained in the form required by expanding the electron wave expansion in terms of plane waves

$$\sum_{G'} \left[\frac{1}{2} |\mathbf{k} + \mathbf{G}|^2 \delta_{GG'} + V_{ion}(\mathbf{G} - \mathbf{G}') + V_{xc}(\mathbf{G} - \mathbf{G}') \right.$$

$$\left. + V_H(\mathbf{G} - \mathbf{G}') \right] c_{\mathbf{G'nk}} = \varepsilon_i c_{\mathbf{Gnk}} \tag{3.7}$$

obtained by substitution of equation (3.4) in equation (2.25).

It is clear that the first term in above equation representing the reciprocal representation of the kinetic energy is diagonal, while the potentials V_{ion}, V_{xc} and V_H representing Coulombic, exchange-correlation and Hartree potentials are expressed in terms of Fourier components. The solution of (3.7) proceeds by diagonalization of a Hamiltonian matrix whose elements $H_{k+G,k+G'}$ are given by the terms in brackets above , or by using the Car-Parrinello or conjugate-gradient methods for large basis sets; the details of which will be described in section 3.10. However, the size of the matrix is fixed by the choice of cut off energy E_{cut}, and will be intractably large for systems that contain both the valence and core electrons. This is a problem, but it can be overcome by using the pseudopotentials as we describe later.

3.4.   K-point Sampling

It has already been described from Bloch's theorem that each electron occupies a definite state k. However, the theoretically infinite number of electrons within a periodic solid corresponds to an infinite number of k-points. At each k-point, only a finite number of available energy levels are occupied. Thus it is required to consider a finite number of electrons at an infinite number of k-points. However, it is possible to use only a finite number of k-points using special

sampling in reciprocal space. Therefore, an integrated function $f(r)$ over the Brillouin zone can be written as

$$f(r) = \frac{\Omega}{(2\pi)^3} \int_{BZ} F(k)dk = \sum_j w_j F(k_j) \tag{3.8}$$

where $F(k)$ is the Fourier transform of $f(r)$, Ω is the cell volume, j represent the number of special points in a set and w_j are weighting factors. Monkhorst and Pack (1976) described the method consisting a set of special k-points for selecting the appropriate sampling of Brillouin zone. This is an unbiased method of choosing a set of k-points.

3.5.   Pseudopotentials

The basic idea of the pseudopotential is the replacement of one problem with other. The pseudopotential approximation replaces the core electrons and the coulomb potential with a weaker potential. The purpose of this is to develop smooth, node-less pseudo wave functions for the valence states in the core region while matching the real wave function outside a 'core radius' r_c . A material in a system consists of ion cores and valence electrons, cores consist of atomic nuclei and tightly bound electrons held by a strong coulomb potential. The wave functions of these core electrons are orthogonal to the valence electrons. In the pseudopotential method, the ion cores are considered frozen and valence electrons are treated explicitly. On the basis of this assumption, core electrons do not influence the chemical bonding of the system and do not change as a result of the environment.
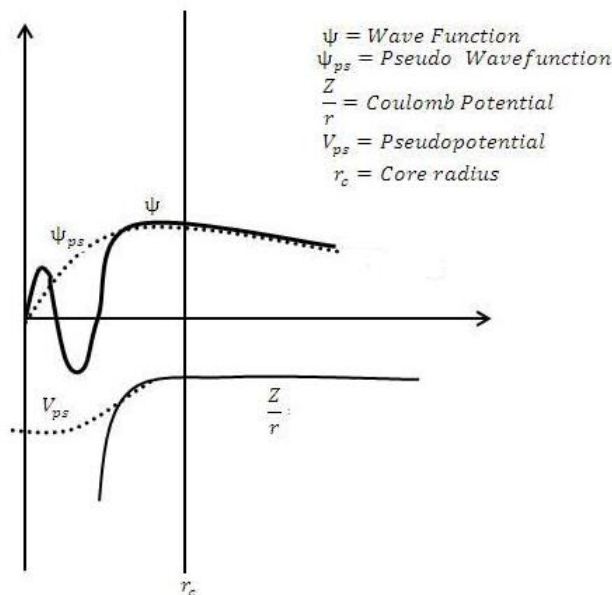
Figure 3-1: Pseudo wave function and potential corresponding to all electron wave function and potential are identical outside the core radius r_c .

The weaker potential is vital as it makes the solution of the Kohn-Sham equations simpler by allowing the expansion of the wave functions in a relatively small set of planewaves. In this way, pseudopotentials can reduce the computational effort.

3.6.   Ab-initio Pseudopotentials

The ab initio pseudopotentials used in electronic structure calculations are generated from ab initio all electron atomic calculations. Within DFT, this is done by assuming a spherical screening approximation and self-consistently solving the radial Schrodinger equation. The Schrodinger equation for an atom can be expressed assuming spherical symmetry;

$$\hat{H}\psi_l^m = E_l\psi_l^m \tag{3.9}$$

$$\psi_l^m = \frac{u_l}{r}Y_l^m(\theta, \varphi) \tag{3.10}$$

Where u_l is a solution of the radial Schrodinger equation.

If we replace u inside the core region with an optimally smooth function the radial Schrodinger equation becomes (Fuchs and Scheffler, 1999).

$$\left[-\frac{1}{2}\frac{d^2}{dr^2} + \frac{l(l+1)}{2r^2} + V_l^{ps}(r)\right]u_l^{ps} = E_l u_l^{ps} \tag{3.11}$$

The expression for pseudopotential $V_l^{ps}(r)$ can be written as

$$V_l^{ps}(r) = \frac{\left[E_l + \frac{1}{2}\frac{d^2}{dr^2} - \frac{l(l+1)}{2r^2}\right]u_l^{ps}}{u_l^{ps}} \tag{3.12}$$

Values for the potential V_l^{ps} corresponding to value of l are obtained from the above expression. This results in the semi-local pseudopotential;

$$V^{Ps} = \sum_l V_l^{ps}(r)\hat{p}_l \tag{3.13}$$

In early studies of pseudopotential methods, Kleinman and Bylander (1982) introduced the non-local separable pseudopotential to reduce the number of integrals for the energy band calculations. Non-local pseudopotentials in the semi-local form can be expressed as:

$$V^{Ps} = V^{loc}(r) + \sum_l \sum_{m=-l}^{l} \delta \widetilde{V_l^{ps}} \, \hat{p}_l \qquad (3.14)$$

with $\delta \widetilde{V_l^{ps}} = V_l^{ps} - V^{loc}(r)$ and $\hat{p}_l$ represents the projection operator. The Kleinman-Bylander potential can be given in separable form as:

$$V_{KB}^{ps} = V^{loc}(r) + \sum_{lm} \frac{|\delta V_{lm} \Psi_{lm}^{PS} >< \delta V_{lm} \Psi_{lm}^{PS}|}{\left\langle \Psi_{lm}^{PS} \middle| \delta V_{lm} \middle| \Psi_{lm}^{PS} \right\rangle} \qquad (3.15)$$

Ψ_{lm}^{PS} is an eigenstate of the Hamiltonian. Kleinmann-Bylander pseudopotentials are norm conserving (see next section) and allow the calculation to scale linearly with the size of basis set.

3.7.   Norm-Conservation Condition

Norm conserving pseudopotentials are developed under the following conditions (Hamann et al., 1979).

1. Real and pseudo valence-state eigen-values are the same for a selected atomic configuration.

2. Real and pseudo-wave functions must be matched beyond a core radius, r_c.

3. The integrals from 0 to r of the real and pseudo-charge densities agree for each valence state for $r > r_c$. Thus both charge densities should be equal beyond the core radius.

4. The logarithmic derivatives of the real and pseudo-wave functions agree at r_c.

5. The first energy derivative of the logarithmic derivatives of the real and pseudo wave functions agree at r_c.

The third condition is important as this is related to the conservation property of a pseudopotential. The properties (4) and (5) are also vital for pseudopotential to have an optimum transferability among the various chemical environments in self-consistent calculations in which the pseudo charge density is treated as a real physical object.

3.8.   Transferability

The hardness of a pseudopotential is a measure of its variation in real space which is quantified by the extent of the potential in Fourier space. Usually, hard

potentials describe the properties of the localized rigid ion cores and are more transferable from one material to other. However, soft (smooth) potentials lead to the poor transferability. Considerable efforts have been made to find accurate and transferable potentials.

The transferability is a measure of the ability of the valence pseudo-electrons to respond to a change in the environment properly (Goedecker and Maschke, 1992). The norm conservation assures that the electron states of the atom have the correct first derivative with respect to energy. The integrated charge density in the core region is also closely related to the norm conservation condition.

3.9.   Ultrasoft Pseudopotentials

An ultrasoft pseudopotential was developed by Vanderbilt (1990) to achieve a much smoother pseudo-wave function. This method is based on two main points:

(i) The potentials are constructed from the atomic states evaluated at two different energies. It means that more than one reference energy ε per quantum state is allowed. For each quantum number l corresponding to a reference energy ε, a pseudo wavefunction φ^{PP} is constructed which fulfills the norm-conserving conditions.

For each pseudo wave function, a function can be described as (Kresse and Hafner, 1994):

$$|\chi_{lm\varepsilon}> = (\text{T}+V_{loc} - \varepsilon) \, |\varphi_{lm\varepsilon}^{PP} > \qquad (3.16)$$

It is now possible to describe the nature of basis $\beta_{lm\varepsilon}$ which is dual to $\varphi_{lm\varepsilon}^{PP}$. It means to have a rather complete set of projectors, two partial waves for each quantum channel l,m are constructed.

If the l,m and ε are labelled as index j for the basis $\beta_{lm\varepsilon}$ and these parameters are also labelled as i for the pseudo wave function $\varphi_{lm\varepsilon}^{PP}$, then

$$\langle \beta_i | \varphi_j^{PP} \rangle = \delta_{ij} \qquad (3.17)$$

also

$$\langle \beta_i | \varphi_j^{PP} \rangle = \delta_{ij} \qquad (3.18)$$

and

$$|\beta_i > = \sum_j (B)_{ij}^{-1} \, |\chi_i > \qquad (3.19)$$

where

$$B_{ij} = \langle \varphi_j^{PP} | \chi_i \rangle. \tag{3.20}$$

The nonlocal factorised pseudopotential operator can be described as

$$V^{NL} = \sum_i |\chi_i \rangle \langle \beta_i| = \sum_{i,j} B_{i,j} \, |\beta_j \rangle \langle \beta_i| \tag{3.21}$$

It can be proved that $B_{i,j}$ and thus V^{NL} are Hermitian if the pseudopotential φ_i^{PP} satisfies a generalized norm conserving constraint;

$Q_{i,j}$ are matrix elements:

$$Q_{i,j} = \langle \varphi_j^{AE} | \varphi_i^{AE} \rangle - \langle \varphi_j^{PP} | \varphi_i^{PP} \rangle = 0 \tag{3.22}$$

The above equation can be written as

$$Q_{l\varepsilon,l\varepsilon'} = \int_0^{r_c} (\varphi_{l\varepsilon}^{AE} \varphi_{l\varepsilon'}^{AE} - \varphi_{l\varepsilon}^{PP} \varphi_{l\varepsilon'}^{PP}) \mathrm{dr} = 0 \tag{3.23}$$

This step makes better the transferability over a large energy range even for larger cut-off radii r_c. Such norm conserving Vanderbilt pseudopotentials have been worked out for certain elements, (Chou, 1992, Morrison et al., 1993), but usually these are not used in calculations.

(ii)   Dropping the norm-conservation constraint leads to a new class of pseudo-potentials. The pseudopotential operator is no longer Hermitian; but it is possible to transform the standard eigenvalue form:

$$(T + V_{loc} + V^{NL} - \varepsilon) \, |\varphi \rangle = 0 \tag{3.24}$$

 to a generalized eigenvalue problem:

$$(T + V_{loc} + V^{NL} - \varepsilon S) \, |\varphi \rangle = 0 \tag{3.25}$$

with the Hermitian overlap operator:

$$S = 1 + \sum_{i,j} Q_{i,j} \, |\beta_j \rangle \langle \beta_i| \tag{3.26}$$

β_i is projector function depending on ionic positions with Hermitian pseudopotential operator:

$$\hat{V}^{NL} = \sum_{i,j} D_{i,j} \, |\beta_j \rangle \langle \beta_i| \tag{3.27}$$

where

$$D_{i,j} = B_{i,j} + \varepsilon_j Q_{i,j} \tag{3.28}$$

As the norm-conservation constraint does not apply, a charge deficit between the pseudo wave functions and exact wave functions exists. This deficit is described by the local augmentation charges. There is close connection between the augmentation charges and overlap operator in the generalized eigenvalue problem above.

    It can be verified that the ultrasoft pseudopotentials generated with the above steps have an excellent transferability; it means that pseudo wave functions and their

logarithmic derivatives match at each reference energy ε_i and for small variations around it. The basic purpose of these potentials is to allow calculations to be performed with as low a cut off energy for the plane wave basis set as possible. This is due to relaxing the norm conservation rule. The resulting wave function can then be expanded using a small plane wave basis set.

In this work, the pseudo atomic calculations have been performed at configurations for C: $2s^2 \ 2p^2$ and H: $1s^1$ for the ultrasoft pseudopotentials. The ultrasoft on the fly (OTF) pseudopotentials (Vanderbilt, 1990) have been used for graphitic and hydrogenated graphitic materials. The CASTEP code allows generating pseudopotential on the fly, parameters can be provided rather than a file from the data base. This approach has a number of advantages; for example, the same exchange and correlation functional for atomic and solid state calculations can be used. It is possible to generate softer and harder potentials by changing the core radius.

3.10.   Solution of Kohn-Sham Equations

There are several methods to minimize the Kohn-Sham equation (2.25). A few well known methods are presented here.

3.11.   Matrix Diagonalization

The Kohn-Sham matrices can be constructed for a given set of atomic coordinates and trial density function. Hamiltonian matrices for each k-point must be formulated using the coefficients "c_{Gnk}" as in equation (3.4) and diagonalized to obtain the Kohn-Sham eigenstates. The matrix diagonalization produces a set of eigenstates that can be used to generate the new charge density. A new set of matrices are now constructed using new density. This process is repeated again and again until self-consistency is achieved. The procedure is depicted in Figure 3-2. The number of plane waves required in calculation, N_{PW}, increases with the volume of the unit cell. This method is not efficient as computational cost for iteration increases with the cube of number of plane waves.
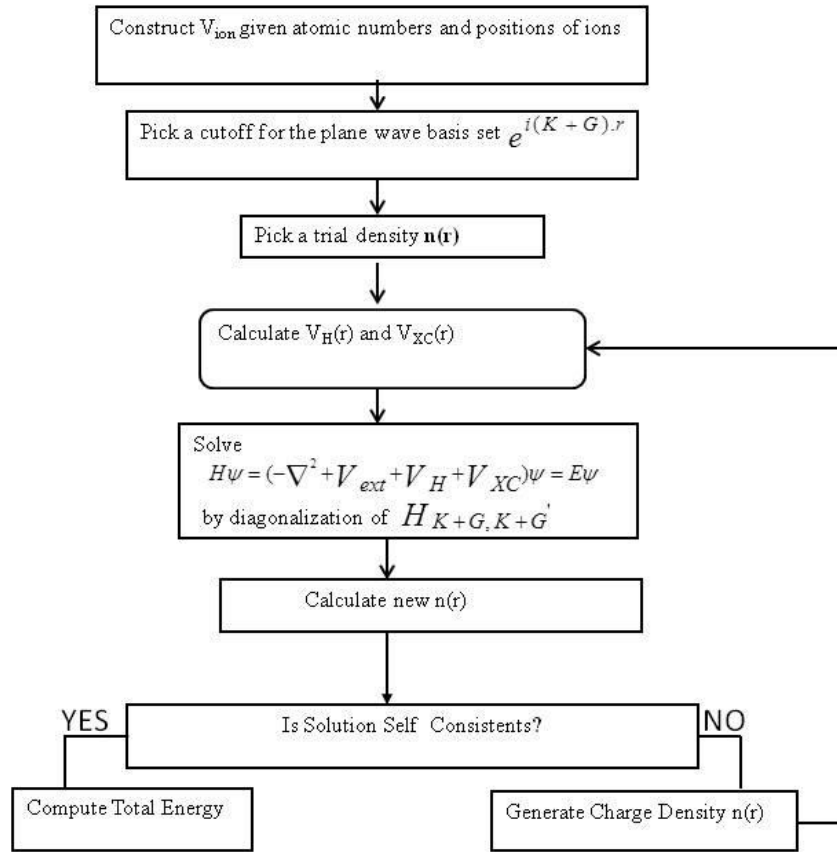
Figure 3-2: Flow diagram of the conventional matrix diagonalization process.

3.12.   Iterative Methods

Iterative methods reduce the computational costs when compared with the diagonalization of the Kohn-Sham matrix by finding only the lowest energy eigenstates. The techniques depend upon the initial guess of the energy of the system and the nature of the iterative steps.

The Car-Parrinello technique is an iterative method (Car and Parrinello, 1985). The iterations in this case are performed by integrating an effective classical force equation after assigning a fictitious mass, μ, to each Kohn Sham wave function. The effective force on a wavefunction is given by:

$$-\frac{dE}{d\phi_i} = -\hat{H}\phi_i \qquad (3.29)$$

Where $\hat{H}$ is Kohn-Sham Hamiltonian to comply with orthonormality constraint.

This force can be used to integrate an effective set of Newton's equations:

$$\mu\ddot{\phi}_i(t) = -\hat{H}\phi_i \tag{3.30}$$

Initial conditions are determined by some guess to ϕ_i and $\dot{\phi}_i$ assuming an initial effective kinetic energy associated with the time varying functions

$$E_{kin} = \frac{\mu}{2}\sum_i \langle \dot{\phi}_i | \dot{\phi}_i \rangle \tag{3.31}$$

As we integrate in time, the wave functions will approach the ground state provided E_{kin} is kept small in some sense.

3.13.   Steepest Descent Method

The ground state of a given configuration is found by direct minimization of the energy functional. The gradient of the energy function ∇E is calculated by $H\psi$. The simplest of these methods is the steepest descent (SD) method. This can be illustrated by using two dimensional functions on a contour graph.

A simple minimization method is to move along directions of steepest descent locating the minimum along the path of steepest descent and calculating new directions from the minimum until the ground state is found. The steepest descent method is limited by the fact that each direction is chosen using the information regarding the present sample point only neglecting the knowledge of previous directions. Assuming an arbitrary function F(x), and starting from the point x_1, the direction of steepest descent g_1, is calculated from the gradient operator. The function is minimized along g_2 to the point x_2 where the gradient g_2 is calculated ($g_2 \perp g_1$). These iterations continue until $F(x_n)$ is equal to $F(x_{n+1})$ with a given tolerance. This can demand many steps to reach the minima and is not always assured to find accurate minima.
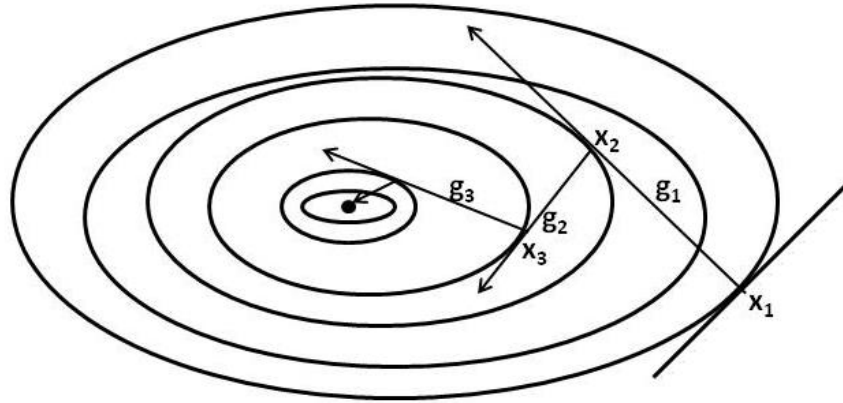
Figure 3-3: The steepest descent method requires many steps to converge.

3.14.   Conjugate Gradient Method

The Conjugate Gradient (CG) method generally requires fewer iterative steps than Steepest Descent (SD). The Conjugate Gradient (CG) method combines the information from all previous directions in such a way as to create a subsequent search direction that is independent of all previous directions. Starting from a point x_1, the function is minimized along the direction of d_1 which for this first step is the direction of gradient g_1, as in the SD method. The direction of d_{n+1} for subsequent iterations are conjugate to all previous directions (Fletcher and Reeves, 1964) and calculated by

$$d_{n+1} = -g_{n+1} + \gamma_n d_n$$
$$where \;\; \gamma_n = \frac{g_{n+1} \cdot g_{n+1}}{g_n \cdot g_n}$$

(3.32)

γ_n is the step size along the gradient g_{n+1}. This usually reduces the number of steps needed to converge on the minima as shown in Figure 3-4. The conjugate gradient method is the best n-steps procedure for solving a set of simultaneous linear equations containing a symmetric positive matrix of coefficients. The CASTEP code implements an efficient CG method or a related scheme known as Density Mixing.
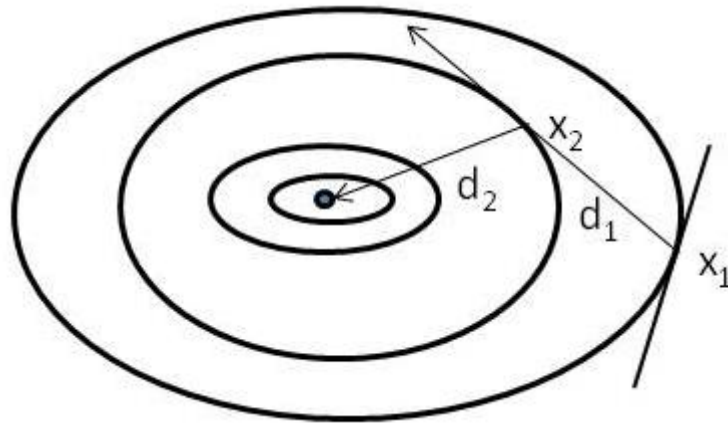
Figure 3-4: The conjugate gradient method requires two steps to converge.

3.15.   Density Mixing Scheme

In this scheme, the sum of electronic eigenvalues is minimized in the fixed potential rather than self-consistent minimization of the total energy (Kresse and Furthmuller, 1996). The new charge density at the end of a step is mixed with the initial charge density and process is repeated until convergency is achieved. The major advantage of density mixing is that metallic systems can be reliably converged in a quite small number of steps. The density mixing scheme can be used together with other minimization methods such as conjugate gradients that minimize the sum of eigenvalues.

3.16.   Fast Fourier Transforms

A major computational requirement is calculating the product of the Hamiltonian with a wave function $H\psi$. As the wave functions are expressed by a finite set of plane waves, this leads to the idea of a reciprocal–space grid. The components of Hamiltonian e.g. kinetic energy, the Hartree and the local pseudopotential operators can be expressed in reciprocal space in a "best possible" way. Thus transformation between real and reciprocal space has a benefit during the parts of calculations. A Fast Fourier Transform (FFT) is an efficient way of transforming various entities (wave function, potentials, search direction) from real to reciprocal space and vice versa (Segall et al., 2002).

3.17. Geometry Optimization

We may need to change the ionic positions to minimise total energy. Forces on the ions are calculated in minimization process to optimize the geometry. The force on an atom may be obtained as

$$F = -\frac{dE}{dR}$$
(3.33)

the partial derivative of total energy with respect to atomic positions give the force acting on that atom. The default for CASTEP is BFGS {Broyden-Fletcher-Goldfarb-Shanno} method (Broyden, 1970), in which a variable matrix method works in the same way as in Conjugate Gradient (CG) but it searches in a more accurate direction by evaluating the Hessian Matrix and therefore requires more memory to store large matrices but this problem can be solved on large parallel machines.

3.18. Summary

The electron wave-function can be expressed as the product of a cell-periodic part and a plane-wave part. The pseudopotential-method can reduce computational effort to solve density functional theory calculations of the solids by treating only the valence electrons.

The Kohn-Sham equations can be solved by matrix diagonalization or iterative methods to obtain the ground state wave function. The forces on the atoms in the system can be obtained from the gradient of energy. The magnitudes of forces lead towards the stable structure of the system. The properly optimized structure can be used in better modelling to a real material if the coordinates of atoms do not much differ from the experimentally calculated values.

Chapter 4. Lattice Dynamics and Thermodynamics

4.1.   Introduction

In this chapter, the theory of lattice dynamics is explained for properties of a crystal that are not covered by the static lattice model but describe the net motions of atoms. These properties include the dispersion relations, heat capacity and free energy. In the harmonic approximation, phonons are considered as independent of each other. However, the vibrations of a real crystal are not purely harmonic, meaning that the concept of independent phonons breaks down. This section covers the ab initio methods to calculate the phonon characteristics. The partition functions of statistical physics enable calculation of the free energy of the system. The harmonic approximation is used in evaluation of the vibrational free energy.

4.2.   Harmonic Approximation

The total potential of the crystal can be written in terms of the inter-atomic potentials assuming multi-body interactions over the sums of two-body terms. Here we will consider two-body interactions only. If an atom whose equilibrium position at lattice site R moves a small distance u(R), its new position is given by

$$r(R) = R + u(R) \tag{4.1}$$

If the contribution to the total potential of the crystal, U, from two atoms at position R and R' is given by $\Phi(R - R')$, the potential can be written as (Ashcroft and Mermin, 1976; p.422);

$$U = \frac{1}{2} \sum_{RR'} \phi\big(R - R' + u(R) - u(R')\big) \tag{4.2}$$

Expanding the above relation about the equilibrium position as a three-dimensional Taylor series we get:

$$U = \frac{N}{2} \sum_{RR'} \phi(R) + \frac{1}{2} \sum_{RR'} \big(u(R) - u(R')\big) . \nabla \phi(R - R')$$

$$+ \frac{1}{4} \sum_{RR'} [(u(R) - u(R')) . \nabla]^2 \ \phi(R - R')$$

$$+ O(u^3)$$

(4.3)

As the first term in the above equation is constant and the second term produces a force (the gradient of energy) that must be equal to zero in the equilibrium configuration, then the next important is the quadratic term. Considering only this term in the potential is known as the Harmonic Approximation. The total potential is therefore defined as a sum of the equilibrium and Harmonic terms:

$$U = U_{eq} + U_{harm}$$

(4.4)

Since U_{eq} is just a constant, it can be ignored in dynamical problems. The harmonic term is usually written in more general form:

$$U_{harm} = \frac{1}{2} \sum_{\substack{RR' \\ \mu\upsilon}} u_\mu (R) f_{\mu\upsilon}(R - R')u_\upsilon(R')$$

(4.5)

Where $f_{\mu\upsilon}$ is the force constant matrix which, for pair potentials, can be written as:

$$f_{\mu\upsilon}(R - R') = \delta_{RR'} \sum_{R''} [\phi_{\mu\upsilon} (R - R'') - \phi_{u\upsilon}(R - R')]$$

(4.6)

4.3. Phonon Calculation: Finite Displacement Method

The finite displacement phonon calculations were carried out in order to calculate the vibrational properties of optimised structures (Frank et al., 1995) after performing the geometry optimization. In a finite displacement calculation, each atom is displaced by small amount along the Cartesian direction, then a self-consistent field calculation is carried out to evaluate the forces on the perturbed system. Both positive and negative displacements are applied in each direction so that corresponding force constants can be calculated using the central force differences. Using the harmonic approximation, vibrational frequencies can be evaluated from the force constants. The number of calculated frequencies is 3N, where N is the number of atoms in the unit cell. As, there are three centre of mass translations along the x, y and z directions, there are, in total, 3N-3 modes of vibration.

In the finite difference approach, $F^+_{i\alpha j\beta}$ is the force on atom j in the β direction due to a shift Δ of the atom i in the positive α direction and $F^-_{i\alpha j\beta}$ is the force due to a shift of atom i in the negative α direction. The force constant matrix $\Phi_{i\alpha,j\beta}$ is given by:

$$\Phi_{i\alpha,j\beta} = \frac{F^-_{i\alpha j\beta} - F^+_{i\alpha j\beta}}{2\Delta} \tag{4.7}$$

Before constructing the dynamical matrix, we have to make sure that the matrix of the force constants should fulfil a particular set of rules (Ackland et al., 1997). The force constants of equation (4.7) can be used in (4.5) to get the potential energy. Firstly, matrix elements should be symmetric because of partial differentiation is commutative;

$$\Phi_{i\alpha,j\beta} = \Phi_{j\beta,i\alpha} \tag{4.8}$$

In this notation the atoms i and j are included in the subscript. α and β show the Cartesian direction.

The second rule follows from Newton's third law:

$$\Phi_{i\alpha,i\beta} = -\sum_{j\neq i}\Phi_{i\alpha,j\beta} \tag{4.9}$$

And from the two above rules, it follows

$$\sum_{j\neq i}\Phi_{i\alpha,j\beta} = \sum_{j\neq i}\Phi_{i\beta,j\alpha} \tag{4.10}$$

These three rules are true regardless of the actual symmetry of the system under consideration. Ideally, for an exact force constant matrix they should be automatically satisfied.

The displacement of atoms to calculate the force constant destroys the periodic boundary conditions. In order to treat this problem in practical terms, a supercell is chosen, which consists of large number of primitive cells such that interaction of an atom outside this cell with the displaced atom in the central primitive cell can be regarded as being negligible. The accuracy of phonon calculation depends upon the size of supercell. By using a large supercell in force calculations, we can include more inter-atomic interactions and reduce the error in this interaction cut-off approximation.

The supercell method for the phonon calculations is an extension of the finite displacement method. The inter-atomic force constant method is based on the supercell approach. In the supercell, Hellmann-Feynman forces on all atoms can be evaluated inside the supercell by moving away one atom from equilibrium in the central primitive cell. The Harmonic approximation remains applicable as long as the displacement of the source atom is small (Ye et al., 2004). The interatomic force constant between the source and destination atoms is described by the ratio of force on the displacement.

$$\Phi_{\alpha\beta}(0j, mk) \cong \frac{\partial^2 E}{\partial x_\alpha(0j)\partial x_\beta(mk)} \approx \frac{\delta f_\beta(mk)}{\delta u_\alpha(0j)} \tag{4.11}$$

In equation (4.11) (0j) and (mk) are the source and destination atoms respectively and α and β are three Cartesian directions x, y and z. The term $f_\beta(mk)$ shows the force acting on the destination atom due to displacement of source atom $\delta u_\alpha(0j)$ and E is the total energy of the system. Suppose the supercell contains M primitive cells, with each primitive cell containing J atoms inside, the 3J×3J dynamical matrix elements are then constructed by the Fourier transformation of the inter-force constants.

$$D_{\alpha\beta}(0j, 0k; \boldsymbol{q}) \approx \frac{1}{\sqrt{M_j M_k}} \sum_{m=0}^{M-1} \Phi_{\alpha\beta}(0j, mk)\, e^{i\boldsymbol{q}.\boldsymbol{R}(\boldsymbol{m})} \tag{4.12}$$

The phonon dispersion relation can be found from the above dynamical matrix. The dynamical matrix is used to solve the eigenvalue problem, $\boldsymbol{\varepsilon}(\boldsymbol{q})$ is the eigenvector of the phonon.

$$\frac{1}{M}D(q)\boldsymbol{\varepsilon}(\boldsymbol{q}) = \omega^2\, \boldsymbol{\varepsilon}(\boldsymbol{q}) \tag{4.13}$$
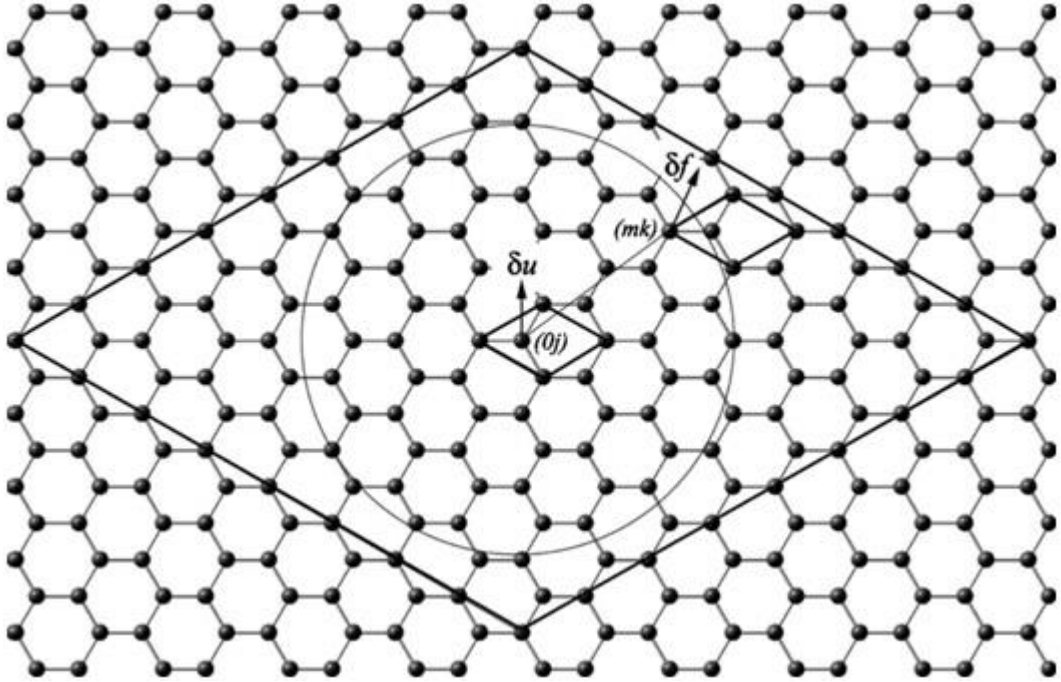
Figure 4-1:The supercell approach for the calculating of dynamical matrices (Ye et al., 2004)

4.4.   Possible Error in Supercell Method

In the supercell calculation, the k-points set (detailed is given in section 3.4) and the FFT grid are a potentially serious source of error in the calculation, both in unit cell and the supercell. Since the supercell consists of unit cells, k-points must be in proportion. In graphite and CNTs systems, two different types of k-points grid were chosen due to difference in dimensions of these crystals.

However, the FFT grid deals with the number of grid points necessary to determine the oscillations in the density. The density needs a grid with twice the linear size of the grid required by the wave function, because the squaring of the wave function to obtain the density doubles the frequencies of the Fourier component. Thus for an exact calculation the FFT-mesh must contain all wave vectors up to $2G_{cut}$ if $E_{cut} = \frac{\hbar^2}{2m} G_{cut}^2$, E_{cut} being the cut-off energy. Increasing the FFT-mesh beyond this value does not change the results, except for a possibly very small change due to the exchange-correlation potential. An insufficient FFT-mesh can cause of 'wrap around' errors (Cote, 2004). The coarse grid (a grid size of the half the spacing of the standard grid) represents the soft density and practically has a

45

spacing 1/1.75 of that of the standard grid. The description of the augmentation charge in ultrasoft pseudopotential needs a finer grid due to high frequency components. We need special care when choosing the FFT grid for the supercell, in all dimensions. For example, if the unit cell is doubled to create the supercell, we must also double the grid for the supercell in order to have an equivalent representation of the system.

Ackland et al. (1997) mentioned the following source of errors which may lead to violation of the sum rule:

- Computational rounding errors and interpolation errors due to use of a discrete grid on which the wave function is represented, as the total energy is not conserved under a rigid shift of entire crystal. Typically, theoretical limit about 10^{-5} (eV/Å) is set by interpolation between FFT grid points.
- Errors to do with evaluating forces using a finite basis set and finite k-point set. Typically these are converged to 10^{-3} (eV/Å).
- Errors may occur in finite convergence of structural parameters. If the structure contains free parameters then relaxation should be performed until the forces on the atom reach a suitable minimum value.
- Errors due to anharmonicity as the forces are calculated using the finite displacement. The minimum possible displacement for which the force can be calculated is checked by the errors in force calculation. The degree of anharmonicity depends on structure.

This understanding about the error in the supercell approach will be utilized to demonstrate the errors in our modelling which is described in results section 7.2.

4.5.   Phonon Density of States

The vibrational or phonon density of states is defined as (Ashcroft and Mermin, 1976;p.464);

$$g(\omega) = \sum_v \int \frac{dk}{(2\pi)^3} \delta(\omega - \omega_v(k)) \tag{4.14}$$

where $g(\omega)\,d\omega$ is the number of the modes in the frequency range $\omega \rightarrow d\omega$ and the integral over the surface of the first Brillouin zone on which $\omega_v(k) \equiv \omega$. Normally, it is convenient to define the density of normal modes per unit volume. Practically, the integration over k is approximated by a sum, where the delta function can be broadened using a Gaussian, so the VDOS becomes

$$g(\omega) = \sum_{v,k} \frac{1}{\sqrt{2\pi}\sigma} \exp\left(-\frac{(\omega - \omega_v(k))^2}{2\sigma^2}\right) \tag{4.15}$$

where σ is a standard deviation. The projected density of states is then obtained by summation of these contributions over all the phonon bands. All the projected phonon DOS add up to the true phonon DOS

Phonon density of states (or vibrational density of states) can be described in analogy with the electronic density of states. The partial (or projected) phonon density of states is determined as a contribution from the given atom to the total phonon DOS. This concept is useful to understand the nature of various branches in the phonon spectrum.

4.6.   Free Energy Calculation

The partition function determines a significant role in thermodynamical calculations (in the present study, namely internal energies and ultimately free energies). The partition function "Z" establishes, as given (4.16), how the particles within the system distribute themselves over the accessible quantum states.

$$Z = \sum_j e^{-E_j/K_B T} \tag{4.16}$$

In the above relation the sum is taken over all over all different quantum states of the system. Z is an abbreviation of German word 'Zustandssumme' which means sum over the states. The Helmholtz free energy is defined as;

$$F = -k_B T ln(Z) \tag{4.17}$$

The partition function is just the product of the partition functions for the translational, rotational and vibrational states of molecule.

$$Z = Z_{trans.} \times Z_{rot.} \times Z_{vib.} \tag{4.18}$$

Thus free energy expression is modified as

$$F = -k_B T ln(Z_{trans.}) - k_B T ln(Z_{rot.}) - k_B T ln(Z_{vib.}) \tag{4.19}$$

In order to calculate the thermodynamics of the gaseous phases that is needed to find the hydrogen release temperature, the translation and rotational contributions are also considered. For diatomic gases, the translational partition function can be written as (Bowley and Sanchez, 1999;p.105,111);

$$\boldsymbol{Z}_{trans.} = V \left(\frac{(m_1 + m_2)k_B T}{2\pi\hbar^2} \right)^{\frac{3}{2}} \tag{4.20}$$

The Free energy relation for translation partition function can be calculated as

$$\boldsymbol{F} = -k_B T ln(\boldsymbol{Z}_{trans.}) \tag{4.21}$$
$$= -k_B T \left\{ ln(V) + \frac{3}{2} ln\left(\frac{(m_1+m_2)k_B T}{2\pi\hbar^2} \right) \right\}$$

where V is molar volume of a diatomic gas.

The pressure for molecules can be written as

$$P = \frac{k_B T}{V} \tag{4.22}$$

The rotational partition function for a rigid rotor is given by

$$\boldsymbol{Z}_{rot.} = \sum_{J=0}^{\infty} (2J + 1) e^{\frac{-\hbar^2 J(J+1)}{2Ik_B T}} \tag{4.23}$$

The Rotational energy of the molecule in free space is

$$E_J = BJ(J + 1) \tag{4.24}$$

Where, J is a quantum number J=0, 1, 2..........

B is a rotational constant calculated from the moment of inertia I.

$$B = \frac{\hbar^2}{2I} \tag{4.25}$$

and
$$I = 2\left(\frac{r}{2}\right)^2 m$$

Rotational free energy can be calculated using the rigid rotor approximation and is given by the relation

$$\boldsymbol{F} = -k_B T ln(\boldsymbol{Z}_{rot.})$$

$$= -k_B T \, ln\left(\frac{2Ik_BT}{\hbar^2}\right)$$

(4.26)

The vibrational partition function is a geometric series which can be summed as (Bowley and Sanchez, 1999;p.112);

$$Z = \sum_{n=0}^{n=\infty} e^{\frac{-\hbar\omega(n+\frac{1}{2})}{k_BT}}$$

$$= \frac{e^{-\frac{\hbar\omega}{2k_BT}}}{1-e^{-\frac{\hbar\omega}{k_BT}}}$$

(4.27)

The vibrational free energy can be written as

$$F = \frac{\hbar\omega}{2} + k_B T \, ln\left[1 - \exp(-\frac{\hbar\omega}{k_BT})\right]$$

(4.28)

Zero Point Energy (ZPE) is the lowest possible energy that a quantum mechanical physical system may have; it is the energy of its ground state. All quantum mechanical systems undergo fluctuations even in their ground state and have an associated zero point energy. ZPE is fundamentally related to the Heisenberg Uncertainty Principle. The relation for zero point energy is given by

$$E_{zp} = \frac{\hbar\omega}{2}$$

(4.29)

Harmonic Approximation leads to thermodynamic properties including the zero point energy and free energy as a function of temperature. In thermodynamics calculations, important points are

- Geometry is fully converged.
- Eigenvalues must be real and non-negative.

The free energy F including the vibrational free energy calculated by CASTEP code can be written as

$$F(T) = E_{tot} + E_{zp}$$

$$+ k_B T \int g(\omega) ln\left[1 - \exp(-\frac{\hbar\omega}{k_BT})\right] d\omega$$

(4.30)

From the Helmholtz energy, F(V,T) and the pressure, the Gibbs energy, can then be evaluated as :

$$G\,(p,T) = F(V,T) + pV \qquad\qquad (4.31)$$

The molar Gibbs energy of an ideal gas is related to Helmholtz energy through $G = F + RT$.

4.7.   Summary

Lattice dynamics can be modelled using the supercell method in order to calculate the phonon properties. The supercell method is an extension of finite displacement method for these calculations. The possible errors in modelling of the supercell phonon method have also been described. The vibrational density of states has also been marked out to get the complete vibrational information of the system. The statistical physics relations have been identified to find the translational, rotational and vibrational properties of the system. The free energy calculations can be used to find the stability of bonds in a system. The free energy calculations play an essential role in determining the hydrogen release temperatures.

Chapter 5. Structural and Vibrational Properties of Graphite

5.1.   Introduction

In previous chapters, computational methods were described to perform the structural and vibrational studies of systems. Here, those methods have been implemented in detail for structural and vibrational studies in graphite systems. Ab initio computational methods which are used in this chapter are combined in the Cambridge Serial Total Energy Package (CASTEP) (Clark et al., 2005). It uses plane waves and its important factors include the pseudopotentials (Norm conserving and ultrasoft pseudopotentials), and various methods of minimization to perform full structural relaxation. Dispersion corrected density functional calculations have been performed to study the structure and vibrational properties of the graphite system. The supercell approach has been applied to study the ab initio dynamical properties.

5.2.   Aims

The main aims of our calculations on the graphite systems are:

- To perform the DFT and DFT-D calculations to investigate the structure of hexagonal graphite.
- To study the band structure of graphite to investigate its semi-metallic nature using a PBE+TS (Pedrew and Yue, 1986, Tkatchenko and Scheffler, 2009) functional.
- To investigate the performance of DFT-D functionals over the DFT functionals to investigate vibrational properties of graphite and study the vibrational density of states for the graphite system using PBE+TS (Tkatchenko and Scheffler, 2009) functional.
- To investigate the structural and vibrational properties of rhombohedral graphite using the PBE+TS (Tkatchenko and Scheffler, 2009) functional.

5.3.   Static Calculation

The hexagonal unit cell of graphite containing four atoms was initially considered in performing the static calculations. The coordinates of those atoms are listed in Table 5-1. The atoms in graphite are arranged in AB stacking layered with hexagonal basal planes of sp^2 hybrid bonded ($\sigma - bonded$) carbon as shown in Figure 5-1, with interatomic spacing along the hexagonal side of 1.42 Å and the inter-planar ($\pi - bonded$) spacing between adjacent planes of 3.35 Å.

Table 5-1:   The relative atomic coordinates of the starting (non-optimised) 4 atom hexagonal unit cell. The lattice parameter a_0 =2.465 Å and $c_{0\ =}$ 6.710 Å are for an un-optimized cell (Trucano and Chen, 1975).

0.000000	0.000000	0.250000
0.333333	0.666667	0.250000
0.000000	0.000000	0.750000
0.333333	0.666667	0.750000
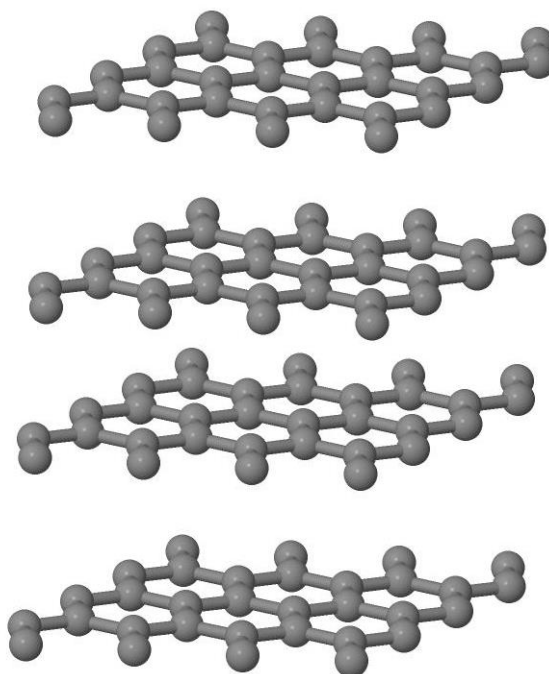
Figure 5-1: The supercell of size $4\times 4 \times 2$ for graphite system as AB layers stacking.

It was initially considered to employ norm conserving pseudopotentials and Vanderbilt   pseudopotentials   for   the   graphite   system.   Norm   conserving

pseudopotentials are considered accurate but these are an expensive method of calculation in large simulation cells. Therefore, ultrasoft pseudopotentials (Vanderbilt, 1990) were applied finally in a supercell approach for the graphite system, as this scheme minimised computational cost.

As there are various choices for ultrasoft pseudopotentials for the graphite in CASTEP libraries, we carried out a number of tests on the primitive cell using various combinations. The convergence properties were verified and it was decided to use on-the-fly (OTF) pseudopotentials in the framework of LDA, GGA-PBE, GGA-D (D=TS, G06) functionals for the graphite system.

5.4.   Convergency Tests

The convergency tests were performed to find the optimum parameters for the graphite structure. By fixing the cut off energy, k points were varied to sample the Brillouin zone. Table 5-2 displays the k-point convergence testing for the graphite system using OTF pseudopotential. The total energy per atom was converged within 1meV for these k-points. Therefore, Monk-Pack (Monkhorst and Pack, 1976) grid of size $16 \times 16 \times 8$ has been used to sample the Brillouin zone having 288 k-points. To determine the optimum E_{cut} needed, single point calculations were performed on the graphite unit cell while systematically increasing the values of cut off energy. The optimum value of cut off of energy 500 eV was determined by fixing the k-points as shown in Figure 5-2 so that values of total energies per atom were converged within 1meV. Thus required accuracy and convergency was achieved, so all calculations on graphite have been performed with the same value of cut off energy and k-points grid.

Table 5-2: Calculated energies of graphite system using different k-points while fixing E_{cut} = 500 eV.

Number of k-points	Total Energy (eV)	Total Energy per atom (eV)
1	-610.67733	-152.66933
3	-623.47543	-155.86886
5	-624.38009	-156.09502
24	-624.43019	-156.10755
40	-624.41363	-156.10341
126	-624.41598	-156.104
188	-624.41377	-156.10344
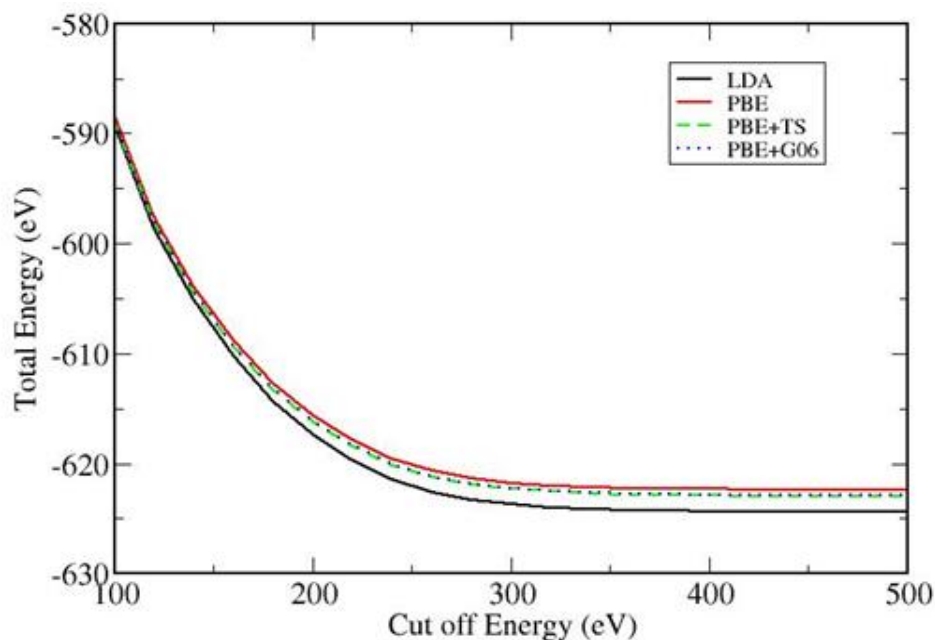
Figure 5-2: Total energy of graphite system with respect to cut-off energy.

5.5.   Crystal Geometry Optimization

We used the BFGS minimization technique to optimize the graphite structure. The forces were zero due to symmetry arising from the p6/mmm (D_{6h}^4) space group. A series of geometry optimization calculations were performed to find the C-C distance in a 4-atom graphite optimized cell. The calculated C-C distance is in good agreement with the value 1.42 Å given in literature (Mohr et al., 2007, Falkovsky, 2008). The LDA overbinds the bond so underestimates the bond length. GGA-PBE

corrects it but slightly overestimates the bond length. The calculated values of lattice constant given in Table 5-3 for LDA and GGA-PBE are comparable with the quoted values by Mounet and Marzari (2005) using LDA and PBE functionals. The calculated values of parameters for dispersion corrected schemes PBE +G06 and PBE+TS seem to be a better choice and more closer to the actual bond length. For the G06 and TS scheme, default values of the parameter for a PBE functional (as implemented in CASTEP code 7.0) have been used. The theoretical details of dispersion corrected parameters have been provided in section 2.14. The calculated values of lattice constants given in Table 5-3 are quite interesting as values of lattice constants improve after adding dispersion corrections with PBE-GGA functional. Experimental values of lattice constants given in Table 5-3 were reported by Hanfland et al. (1989) and Zhao and Spain (1989) who measured these lattice constants using X-ray diffraction. It is clear from Table 5-3 that TS scheme is better for a static calculation as it improves C-C bond lengths and inter-planar distance. In calculation of both these parameters, an error less than 1% was found for the TS scheme as compared with experimental values.

Table 5-3:   Structural parameters of graphite obtained for an optimized structure.

	LDA	PBE	PBE+G06	PBE+TS	Experimental
In-plane lattice constant a_0	2.445 Å	2.467 Å	2.459 Å	2.456 Å	2.460 Å
Interlayer distance/a_0	1.342	1.621	1.295	1.355	1.36
c_0/a_0	2.6826	3.239	2.6007	2.714	2.725
Inter planer distance	3.28 Å	4.0 Å	3.2 Å	3.33 Å	3.35 Å
Bond Length C-C (Å)	1.41339	1.42424	1.42020	1.41836	1.42

The cohesive energy (crystal energy per atom – energy of a single carbon atom) of graphite was calculated using the PBE+ TS functional. The value of cohesive energy was found to be 7.325 eV for the graphite. The calculated value has less than 1% error as compared with the experimental value of the cohesive energy 7.37 eV as cited in Dunlap and Boettgar (1996).

Following the geometry optimization of the graphite structure, the effect of pressure on inter layer distance was investigated using the PBE+TS functional. The values of interlayer distances decrease with an increase in pressure. Such trends are clear from Table 5-4 and comparable with the XRD data given by Wang et al. (2012) who also studied the compression behaviour of graphite. The calculated error in values of inter layer distance was about 1% and the maximum error was about 2.6% at P=19.2 GPa.

Table 5-4: Pressure vs Interlayer distance for a graphite system by PBE+TS functional.

Pressure (GPa)	Interlayer Distance d (Å)	Experimental (Å)
0	3.33	3.35
16.9	2.81	2.75
19.2	2.77	2.70
24.9	2.69	2.69
31	2.66	2.65

5.6.   Band Structure of Graphite and Graphene

Following the geometry optimizations, the ab initio band structures of hexagonal graphite and graphene have been calculated using CASTEP (Clark et al., 2005) for the periodic system. The band structure of graphite shown in Figure 5-4 was calculated using the PBE+TS functional in order to include the VdW interactions. However, no significant difference is found between the calculated band structures from the GGA-PBE functional and PBE+TS functionals.

Band Structures are usually drawn along the symmetry path $\Gamma - M - K - \Gamma$ of the Brillouin zone. The shape of the Brillouin zone for the hexagonal graphite system is shown in Figure 5-3. The π and π^* bands cross each other at K-point at the Femi Level. The band curvature around the K-point is parabolic and it becomes linear away from the K-point. In both graphite and graphene structures, the band gap vanishes at K–point as shown in Figure 5-5 and Figure 5-6 respectively. The crossing

of bands transformed to anti-crossing along K- Γ direction in graphite structure which was also reported by Partoens et al. (2006) who investigated the band structure of graphite and graphene using the tight binding approach. Thus, present findings confirm the semi-metallic character of graphite and zero band gap semi-conductor behaviour for graphene by GGA-PBE approximation (Pedrew et al., 1996). The calculated value of the energy gap for outer π/π^* bands was about 1.48 eV for graphite system at the K-point of Brillouin zone. The calculated value was found to be comparable with the value 1.45 eV for the energy gap of graphite given by AlZahrani and Srivistava (2009) who performed a DFT calculation to investigate the electronic band structure from graphene to graphite. In graphene, the interaction of neighbouring p_z orbitals create delocalized π-bonding and π^* anti-bonding states, which determine the energy bands around the Fermi energy
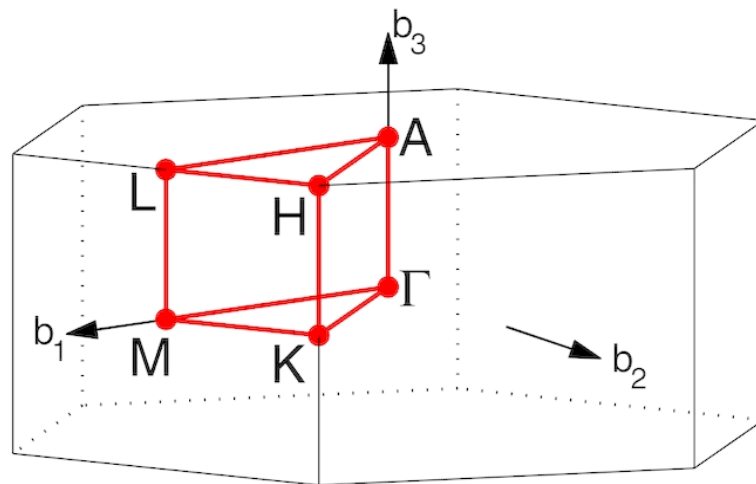
Figure 5-3: The first Brillouin zone of a hexagonal lattice, with high symmetry k-points marked and b_1, b_2 and b_3 are reciprocal lattice vectors (Setyawan et al., 2010; DOI:10.1016).
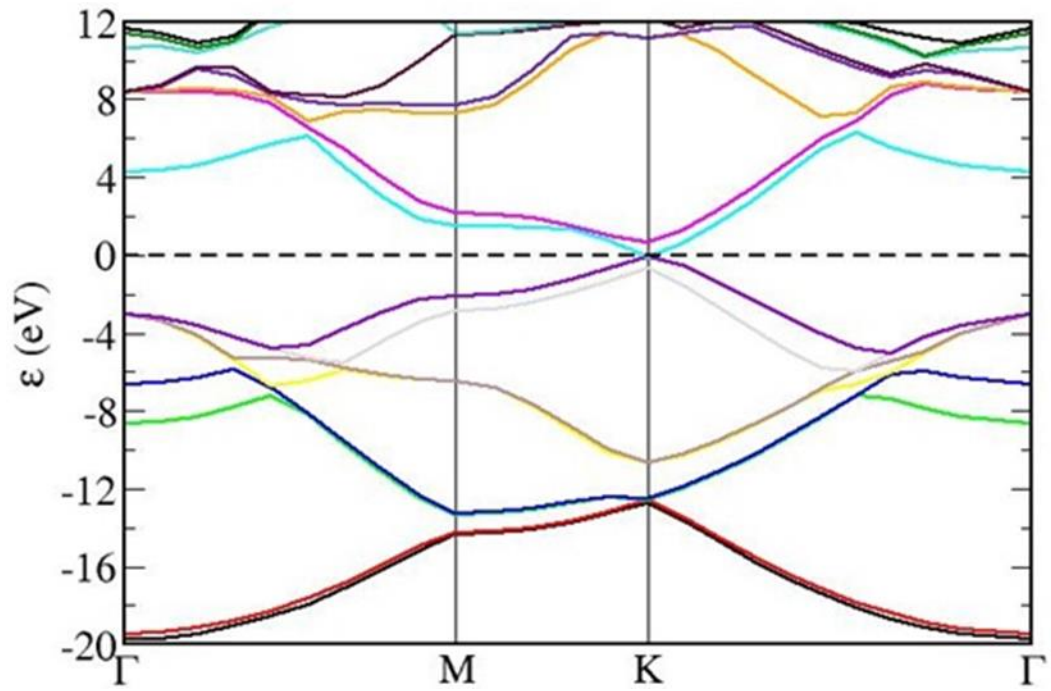
Figure 5-4: Band Structure of graphite using PBE+TS functional along high symmetry direction.
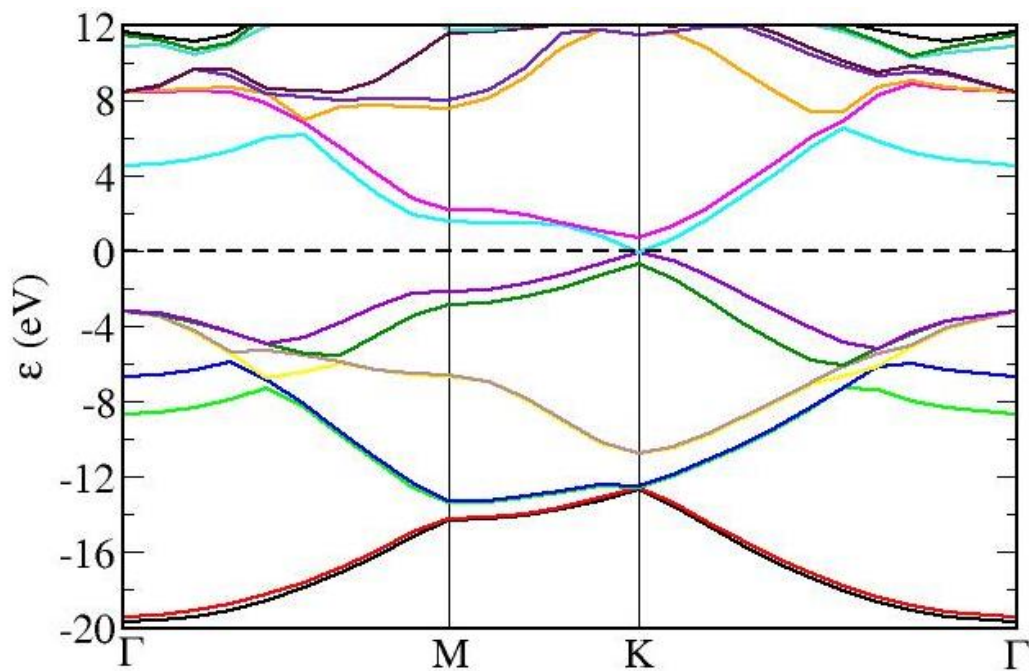
Figure 5-5:   Band Structure of graphite using PBE along the high symmetry direction.
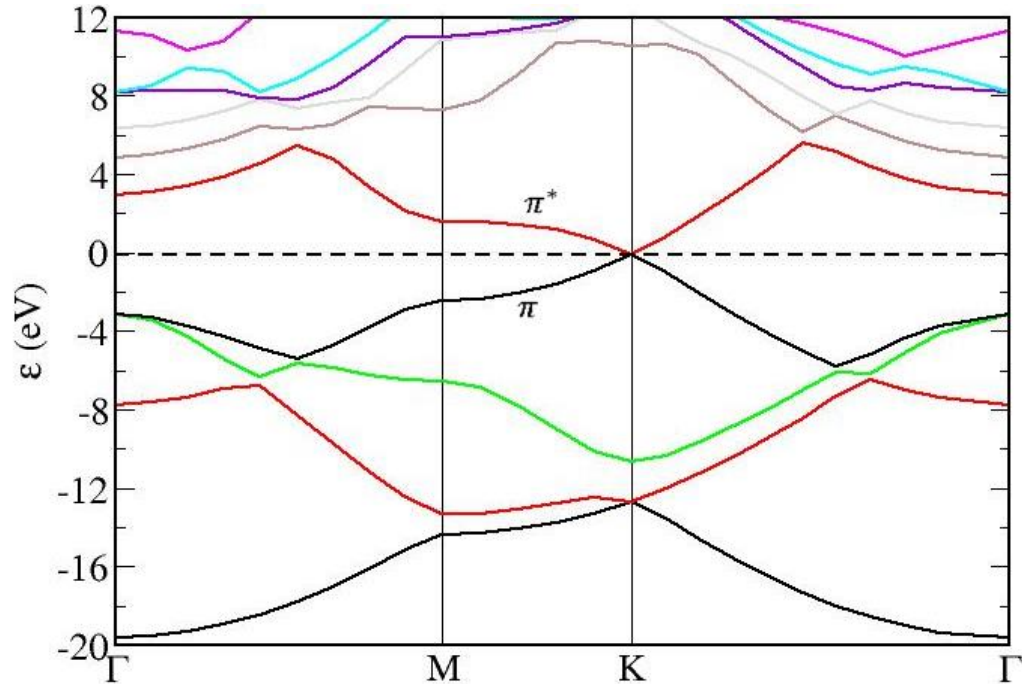
Figure 5-6:   Band Structure of graphene using PBE along the high symmetry direction.

5.7.   Vibrational Study of Graphite using the Supercell Approach

The dispersion curves of phonons for the graphite system were calculated using ultrasoft pseudopotentials (Vanderbilt, 1990)   and the finite displacement method. The supercell of size $4 \times 4 \times 2$ for the graphite system was used and the PBE functional was applied. The atom was displaced 0.01 Å within the cut off radius 10 Å to find the force constant and dynamical matrices and sum rules were also applied (Ye et al., 2004). The selected value of displacement was used to remove imaginary frequencies and anharmonic effects but other factors like un-optimized structure may still cause the imaginary frequencies, too small a displacement magnifies numerical errors in forces and too large a displacement moves into the anharmonic displacement regime.

The twelve force constants were generated in the CASTEP output file along one direction corresponding to one atom for the graphite unit cell having 4-atoms. The atoms that are covalently attached to each other have the largest force constants

due to strong interaction. The force constants can be described in longitudinal and transverse directions. The force constants in our calculation decay rapidly after the value of 2.465 Å i.e. the distance of second nearest neighbour. Dispersion curves including interaction with up to four neighbours are shown in Figure 5-7. It is obvious that bands do not have dispersion for first nearest neighbours which have the distance equal to 1.42 Å. This is due to the fact that the cut off radius is too small for the calculation. The second neighbour has a flat LO band in the dispersion curve. The fourth neighbours have same values of frequencies as compared with frequencies of the third neighbour.
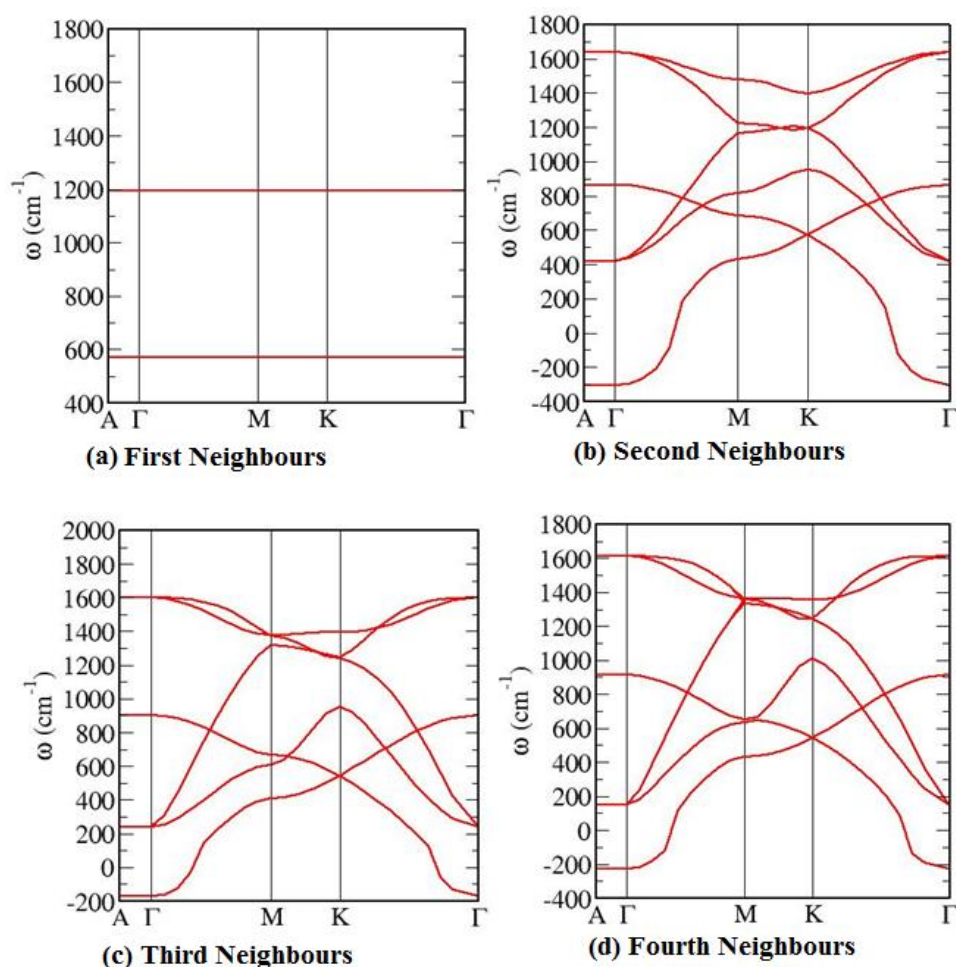
Figure 5-7: Calculated phonon dispersion relation of graphite from 128 atoms supercell by PBE functional to minimize the effect of the periodic boundary condition. The effect of truncating the range of force constants up to four nearest neighbours is shown. Calculations were performed with the experimental lattice parameters.

The imaginary frequencies for lower acoustic branches may be due to un-optimized geometry, pseudopotential error and the wrong selection of k-points for Brillouin zone integration. However, no significant difference is found in the values of frequencies up to four nearest neighbour for the properly optimized graphite structure. For this purpose, the phonon frequencies were converged with respect to k-points sampling after adjusting the smearing parameter at 0.4 eV. The values of smearing between 0.2-0.4 eV can change frequency within 1 cm^{-1}. The final cut-off energy of the value about 500 eV was used for this system.

The First BZ of the hexagonal cell is shown in Figure 5-3. The irreducible wedge is called a subset of BZ k-points after the symmetry has been applied and identifies the practical region of the reciprocal space that must contain all the information of the crystal. We only need to consider k-points in the irreducible part and usually the vibrational energies/frequencies are specified in that region. Dispersion curves are commonly projected along the lines of symmetry ΓA, ΓM, and ΓK. It is clear that the relative coordinates in reciprocal space of points of the special symmetry are $\Gamma = (0,0,0)$, $A\left(\frac{1}{2}, 0, 0\right)$, $M = (0, \frac{1}{2}, 0)$ and K = (-1/3,2/3,0).

Following the geometry optimization and properly relaxed graphite structure, dispersion curves for the graphite system are calculated using the PBE functional as shown in Figure 5-8. The graphite unit cell has twelve modes of vibration. Three modes are zero due to translational degree of freedom. Three are called acoustic modes {acoustic: LA, TA, ZA} and rest of six optical modes {optical: LO, TO, ZO, LO′, TO′, ZO′} are being explained in dispersion curves shown in Figure 5-8 and Figure 5-9. Graphite is a non-polar crystal and has in plane LO/TO modes at Γ, in plane LO/LA modes at K-point, and the out–of-plane ZA/ZO modes at K-point due to symmetry. These modes are also in agreement with the study of Mounet and Marzari (2005) who calculated the modes of vibration using density functional perturbation theory. At the M -point, the LO branch is at higher frequency than the LA, as a result, the two branches do not cross each other between the M-point and K-point. The crossing of TA and ZO branches are found near the M-point. This study is consistent with the study of Mohr et al. (2007) who measured the modes of vibration using inelastic x-ray scattering. Low frequency modes move in phase in one layer but in the opposite direction with the other layer along the A- Γ

direction as shown in Figure 5-9. These out of phase and out of plane modes have been labelled by LO′and TO′ respectively. There are two Kohn anomalies found in graphite system. First the frequency at the Γ-point is lowered due to interaction of the phonon with the electronic system. The second Kohn anomaly in graphite can be found for the TO derived phonon branch at the K-point.
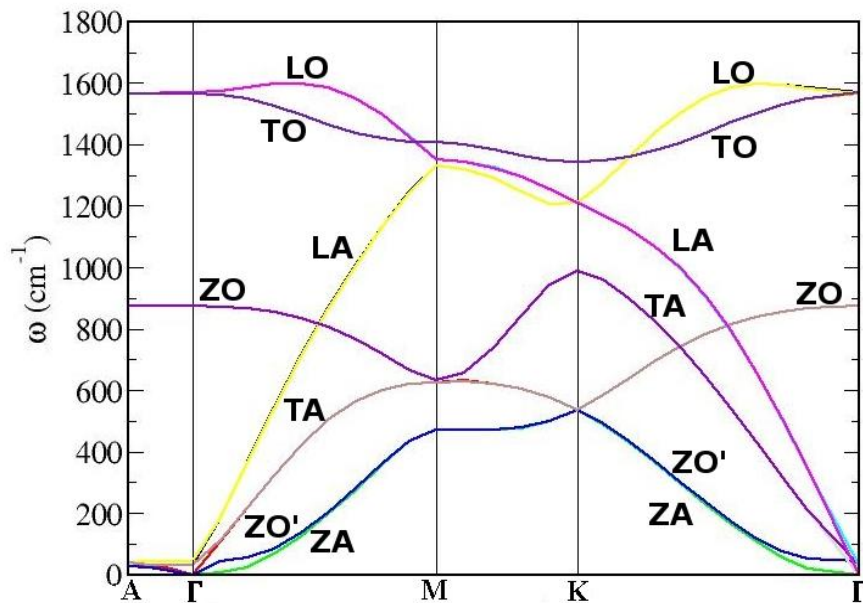
Figure 5-8: Dispersion curve of graphite supercell of 4×4×2 using ultrasoft pseudopotential and finite displacement scheme by PBE functional.
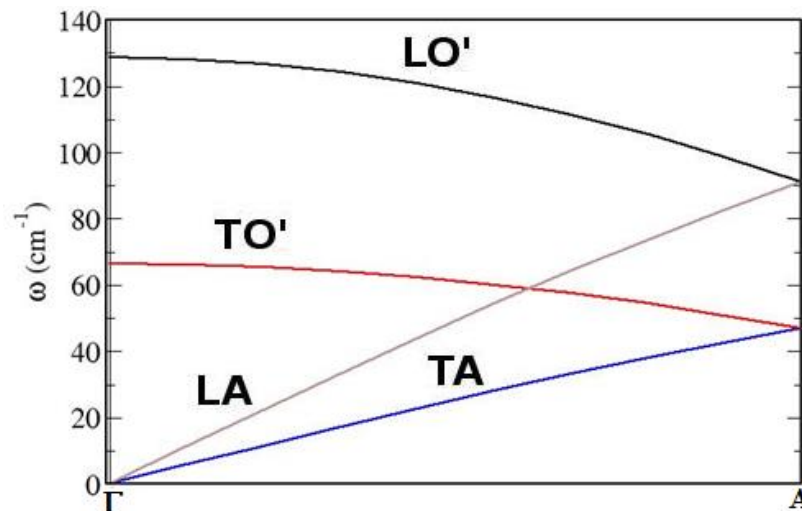
Figure 5-9: Low frequency dispersion curve of graphite supercell of size by 4×4×2 using the PBE functional and the geometry optimised structure.

Dispersion curves as shown in Figure 5-10 and Figure 5-11 are plotted using the LDA functional for graphite. A supercell of size 4×4×2 has been used to perform

the calculations. The finite displacement method was applied to perform the dynamical calculations. The atom was displaced 0.01 Å to find the dynamical matrix and sum rules were also applied. Yan et al. (2008) also mentioned the discrepancy between the LDA and experimental modes of vibration for graphite. This supports the present findings for the low frequency modes of vibrations in the graphite system.
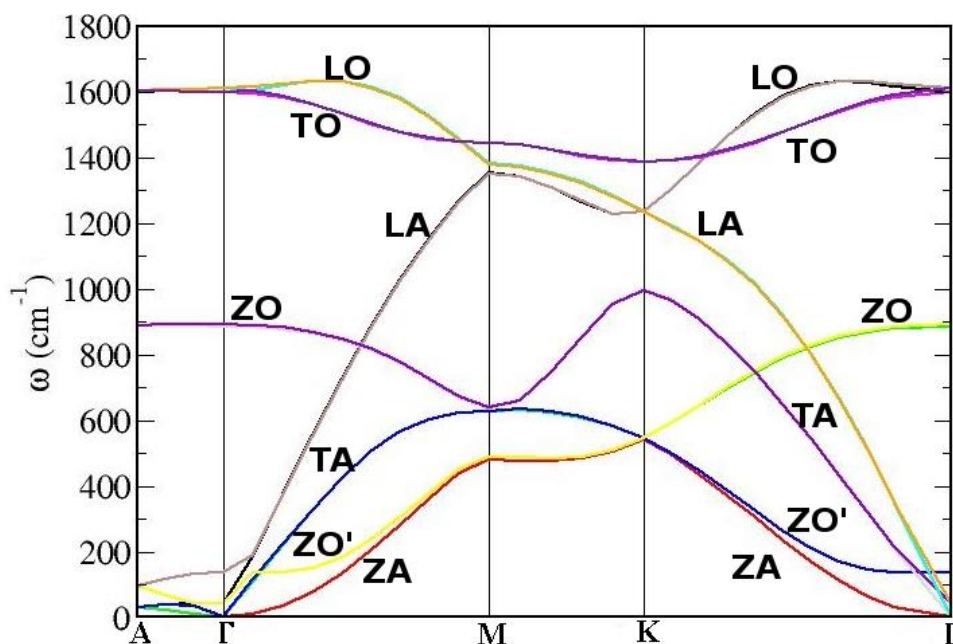
Figure 5-10: Dispersion curve of graphite supercell of size 4×4×2 using LDA functional and finite displacement scheme.
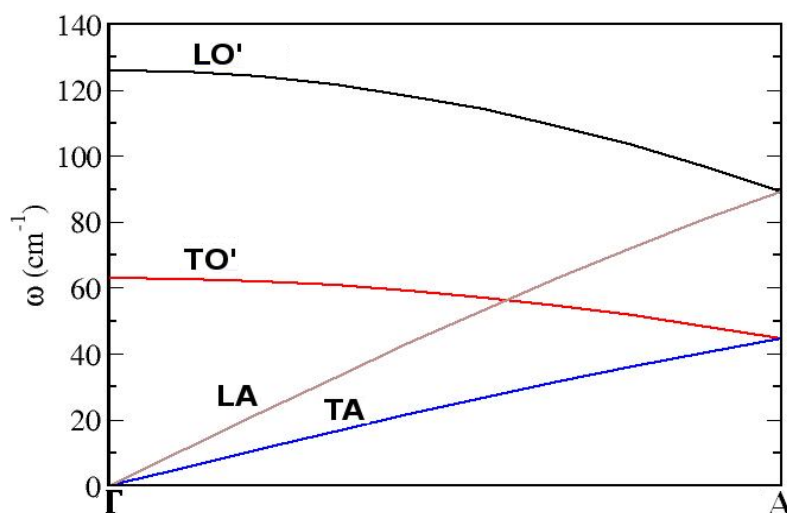
Figure 5-11: Low frequency dispersion curve of graphite supercell of size 4×4×2 using the LDA functional.

To compare the results of the LDA and GGA functionals, dispersion curves are plotted in Figure 5-12 . It is projected from the figures that LDA frequencies have high values compared with PBE functionals. Surprisingly, the low frequency modes of vibration for PBE shown in Figure 5-13 have higher values than the LDA. In dynamical calculations of graphite, underestimation and overestimation of frequency are not specific for PBE and LDA functionals. The GGA gives better results than LDA but GGA needs further improvement. Now it is believed that both LDA and GGA functional have been failed to describe the vibrational frequencies due to lack of long range interlayer interactions in various region of Brillouin zone. The calculated values for the LO′ mode for the LDA and PBE are 125 cm^{-1} and 128 cm^{-1} and compare well with the available experimental value of 127 cm^{-1}. The error for this mode in LDA and PBE calculations was found to be 1.5% and less than 1% respectively. The present study supports the findings of a great deal of the previous work in this field.
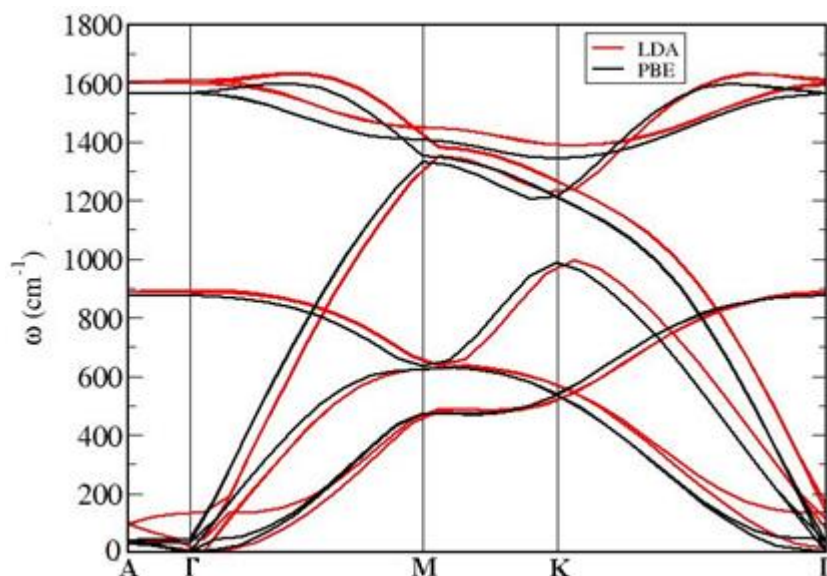
Figure 5-12: Dispersion curve of graphite using ultrasoft pseudopotential and finite displacement scheme for PBE and LDA functionals.
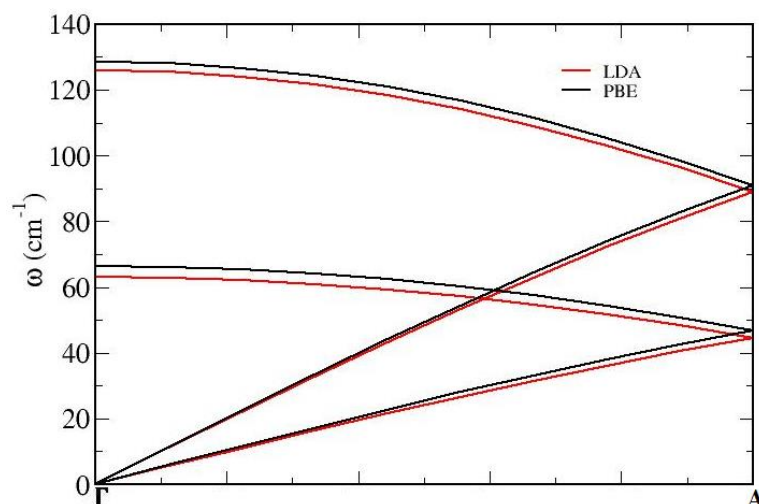
Figure 5-13: Low frequency dispersion curve using the LDA and PBE functionals.

These modes of vibration for PBE functional were visualized using Jmol software. The low frequency optical modes as shown in Figure 5-14 and Figure 5-15 are only found in graphite and are due to the weak VdW interaction. The arrows in figures indicate the direction of the modes of vibration.
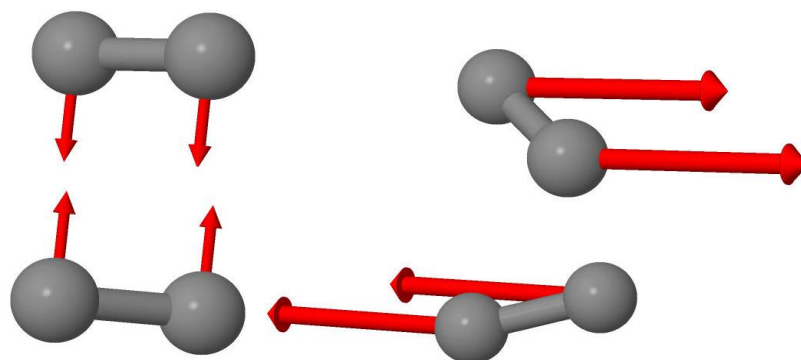
Figure 5-14: (Left) low out of plane mode for frequency 128 cm^{-1}; (Right) out of phase for the frequency 66 cm^{-1} at $\Gamma -$ point the centre of Brillouin zone.
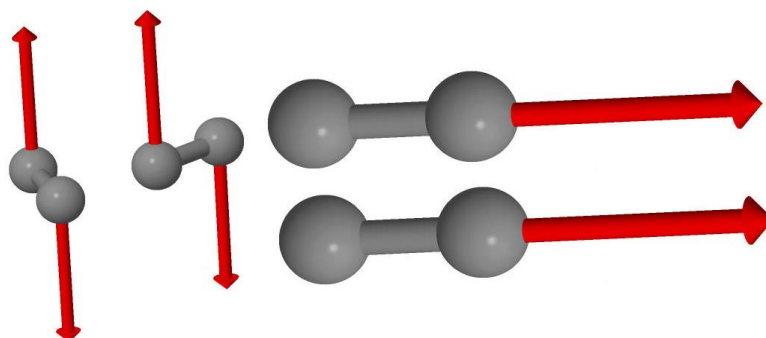
Figure 5-15: (Left) side outer mode for the frequency 879 cm^{-1} ; (Right) inner mode for the frequency 1585 cm^{-1} at $\Gamma -$ point the centre of Brillouin Zone.

65

Phonon frequencies of graphite are given in Table 5-5 to compare the theoretical results with experimental values measured by Nicklow et al. (1972) and Mohr et al. (2007) using inelastic neutron scattering and inelastic x-ray scattering approaches. Our calculated modes of vibration for graphite have been also compared with the theoretical ab initio findings of Mounet and Marzari (2005) and semi empirical calculations which were performed by Zimmermann et al. (2008). These findings do not only strengthen the previous studies of graphite but also give an insight into vibrational properties of graphite. However, the LDA and GGA functional could not produce the accurate vibrational frequencies in graphite as the long range interaction parts were missing in these functionals. To improve these drawbacks, VdW corrections have been considered along with the GGA-PBE and LDA functionals. The details of dispersion corrected modes of vibration will be discussed in section 5.9.

Table 5-5 : Phonon frequencies of graphite by supercell appraoch.

Experimental values were cited in reference of Mounet and Marzari (2005).

Modes	Ab initio PBE (cm⁻¹)	Ab initio LDA (cm⁻¹)	Experimental (cm⁻¹)
$A_{LA/LO'}$	90	89	89
$A_{TA/TO'}$	46	44	35
A_{LO}	879	891	-
A_{TO}	1585	1622	-
$\Gamma_{TO'}$	66	62	42
$\Gamma_{LO'}$	128	125	127
$\Gamma_{LO/TO}$	1585	1609	1581
Γ_{ZO}	874	889	868
$\Gamma_{ZO'}$	129	201	148
M_{ZA}	474	467	471,465,451
M_{TA}	644	629	630
M_{ZO}	651	650	670
M_{LA}	1334	1356	1290
M_{LO}	1354	1373	1321
M_{TO}	1358	1393	1388,1389
K_{ZA}	544	538	482,517,530
K_{ZO}	549	547	588,627
K_{TA}	995	1004	-
$K_{LA/LO}$	1224	1247	1184,1202
K_{TO}	1325	1363	1313,1291

5.8.   Vibrational Study of Graphene

We have used the same lattice input parameters for the graphene system as calculated for the graphite in section 5.5. The structure of the graphene sheet is properly relaxed to attain the equilibrium values of lattice parameters. The calculated

values of lattice constants were about a= 2.443 Å and c= 6.710 Å for LDA and a = 2.465 Å and c = 6.710 Å for PBE respectively. Calculated values of C-C bond lengths for LDA and PBE were 1.4104 Å and 1.4234 Å respectively. The cut off energy 500 eV was used to ensure the convergence of total energies within the value of 1meV. The Monk-Pack k-points grid $16 \times 16 \times 1$ (72-kpoints) was used to make certain the convergence of total energies within 1meV. The calculated dispersion curve of graphene looks similar to graphite except the low frequency modes of vibrations are missing. Actually, low modes splitting have been found due to VdW interactions in graphite only below 400 cm[1]. LDA overbinds the bond length in graphene so frequency in the optical region for LDA is higher than the PBE functional as shown in Figure 5-16.
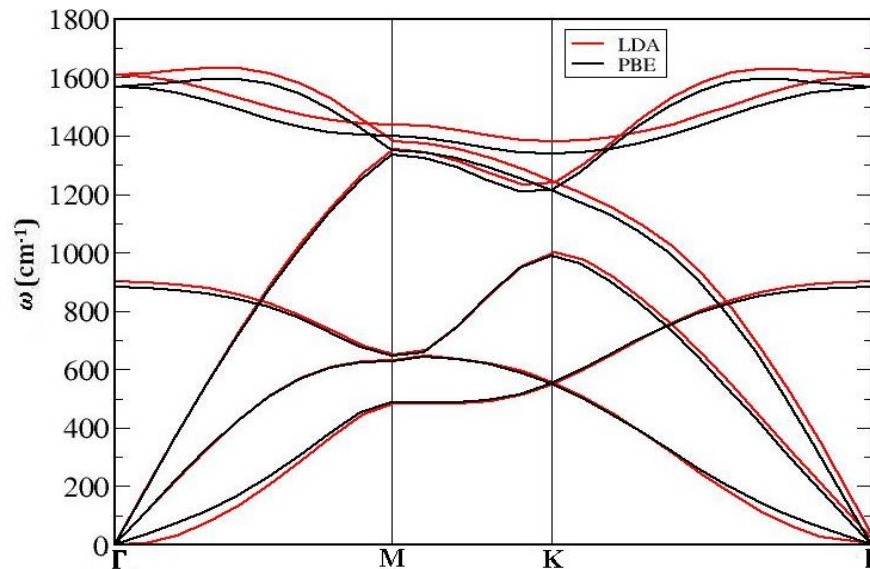
Figure 5-16 : Dispersion curve of graphene using PBE and LDA functional for 4×4×2 supercell along the high symmetry direction.

The calculated values of frequencies for the PBE functional given in Table 5-6 looks close to the experimental values as cited by Mohr et al. (2007) using inelastic x-ray scattering technique. However, values of frequencies using LDA were found to be higher than the experimental values. Wirtz and Rubio (2004) also compared the LDA and GGA with experimental results. According to Wirtz and Rubio (2004), values from LDA were found to be larger than PBE. This is in excellent agreement with our study for LDA and PBE functionals.

Table 5-6 : Phonon frequencies of graphene by supercell appraoch.

Experimental values are taken from the reference (Mohr et al., 2007).

Modes	Ab initio LDA (cm^{-1})	Ab initio PBE (cm^{-1})	Experimental (cm^{-1})
Γ_{ZO}	901	881	867
$\Gamma_{LO/TO}$	1608	1568	1581
M_{ZA}	484	487	480
M_{TA}	631	628	627
M_{ZO}	648	646	670
M_{LA}	1354	1334	1290
M_{LO}	1381	1350	1340
M_{TO}	1439	1400	1398
K_{ZA}	551	551	542
K_{ZO}	551	551	588
K_{TA}	1000	989	1007
$K_{LA/LO}$	1240	1213	1217
K_{TO}	1381	1339	-
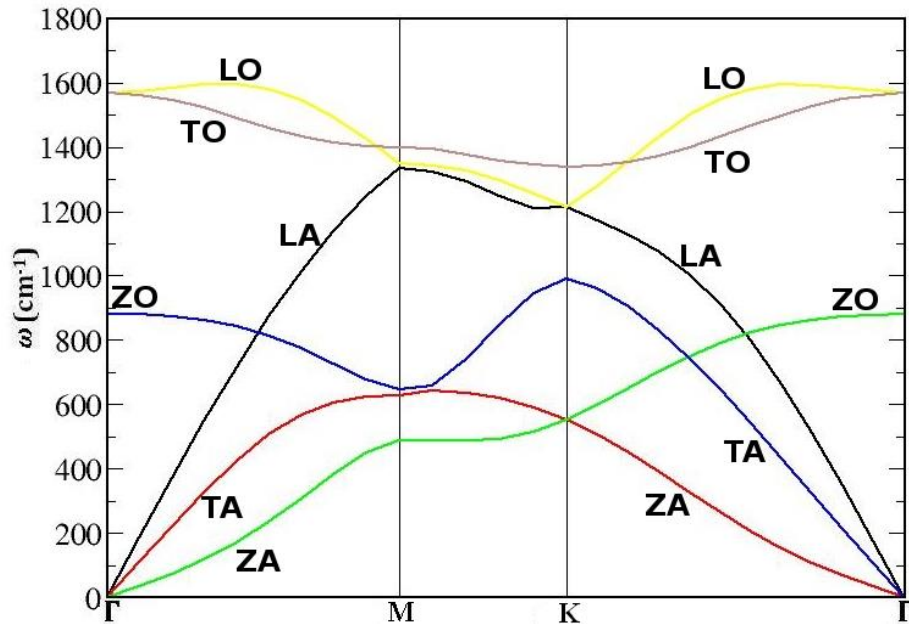
Figure 5-17: Dispersion curve of graphene using PBE functional by 3×3×1 supercell along the high symmetry direction.
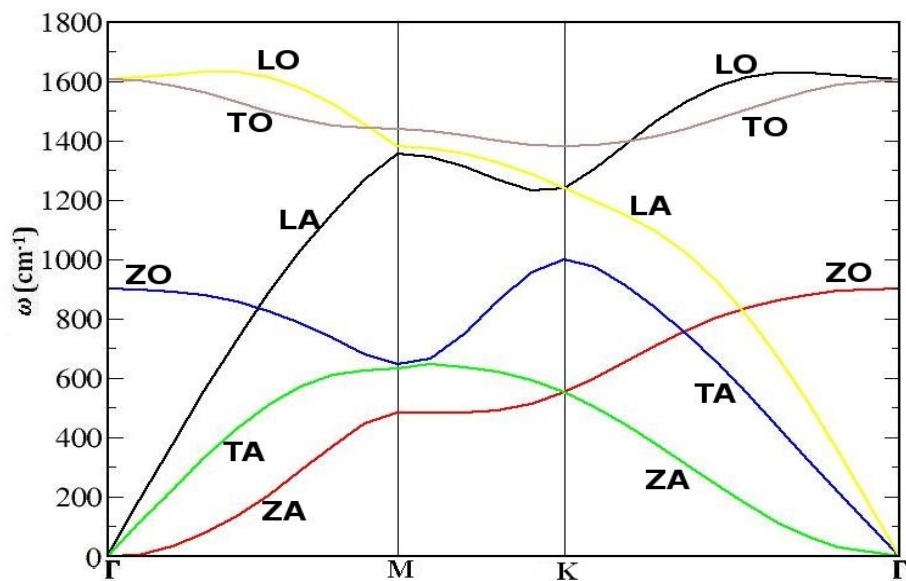
Figure 5-18: Dispersion curve of graphene using LDA functional by 3×3×1 supercell along the high symmetry direction.
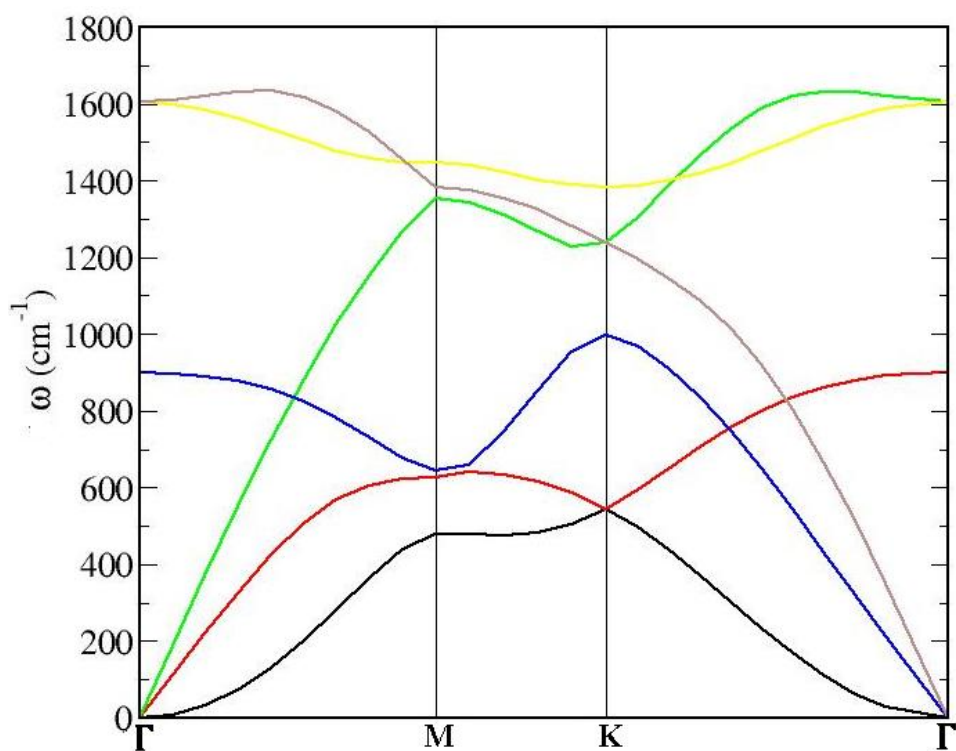
Figure 5-19: Dispersion curve of graphene using LDA functional by 4×4×2 supercell along the high symmetry direction using grid 16×16×1.
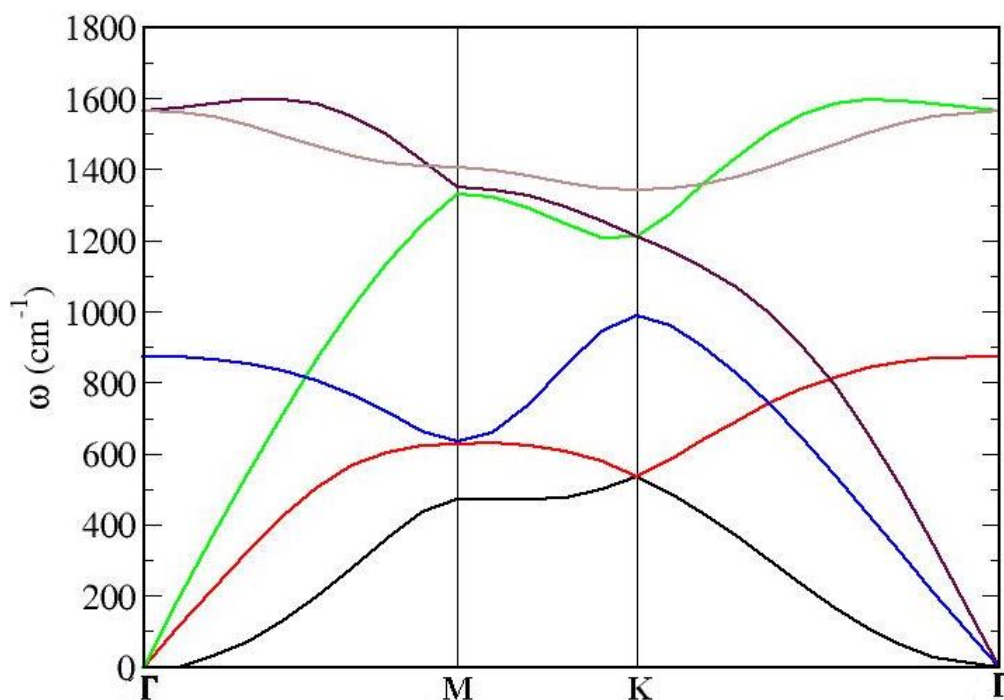
Figure 5-20: Dispersion curve of graphene using PBE functional by 4×4×2 supercell along the high symmetry direction using grid 16×16×1.

5.9.   Dispersion Corrected Study of Phonons

Following the geometry optimization, phonon calculations for graphite were performed using the dispersion corrected schemes. In reviewing the literature, no vibrational study was found for graphite using dispersion corrections. Therefore we performed the vibrational study by including G06 and TS dispersion corrections (Grimme, 2006, Tkatchenko and Scheffler, 2009). Initially, the graphite primitive cell was hexagonal but it was converted into a cubic super cell of size $4 \times 4 \times 2$ containing 128 atoms. The values of frequency were ensured to converge within $1cm^{-1}$ for the k-points. Smearing parameters of value 0.2 eV, 0.3 eV and 0.4 eV were tested and values of frequency were found to be converged within $1cm^{-1}$. The smearing parameter was adjusted to a value of 0.4 eV to converge the frequency. The cut-off radius, 10 Å for the force constant matrix was selected to allow the interaction of large number of atoms. A cut off energy value of 500 eV was used for the phonon calculations. Vibrational frequencies were calculated using the finite displacement method (Ye et al., 2004). To choose the atomic displacement, different types of tests

71

were performed to reduce the negative frequencies and anharmonic effects. The best option was to displace the atom about 0.01 Å.

The functional dependent global scaling factor s_6 and damping function steepness d for the G06 scheme were adjusted to the values 1.50 and 20 in order to get the desired low frequency. The functional dependent scaling factor s_r and damping function steepness d were adjusted for TS scheme. The values of s_r and d were set at 0.86 and 15 to optimize the vibrational properties of graphite. For the choice of these parameters, various tests have been performed (see Appendix A.1). These parameters were found to be sensitive with respect to inter-planar distance. The inter-planar distance increases with the increase of scaling factor s_r and damping function steepness d. These parameters were also found to be sensitive with respect to frequency. The frequency decreases with the decrease in steepness of damping function d and scaling factor s_r. In our calculations, sum rules were enforced to find the dynamical matrix. TS and G06 dispersion were applied with the PBE functional to find the dispersions curves as shown in Figure 5-21 and Figure 5-23.

Table 5-7 shows that in medium and high range of frequency both dispersion schemes produce the values close to the available experimental data. The low frequency optical modes of vibration for PBE+G06 and PBE+TS functionals shown in Figure 5-22 and Figure 5-24 have an excellent comparison with the available experimental data as cited by Nicklow et al. (1972). Both dispersion corrected G06 and TS schemes include the dispersion interaction in graphite system and thus give much better results compared with the previous local and semi-local density functionals studies. The low frequencies out of phase modes of vibration for the TS scheme are found to be closer to the experimental Raman active mode as compared to its value with the G06 functional. Both TS and G06 schemes give accurate values for the out of plane modes but G06 gives high values for the out of phase modes of vibration. The TS scheme can be considered as an accurate scheme as it gives much better results for all ranges of frequencies in graphite system.

The efficiency of calculations increases in dispersion corrected schemes. The time for the calculation was noted from the CASTEP output file and it was found that dispersion corrected G06 the time by 25% as compared with the calculation using

only the PBE functional. The G06 scheme is also slightly faster than the dispersion corrected TS scheme. However, on the basis of vibrational studies, it can be mentioned that the more advanced and self-consistent TS scheme should be considered as a better choice for the graphite system.

Table 5-7 : Phonon frequencies of graphite by supercell appraoch.
Experimental values were cited in reference of Mounet and Marzari (2005).

Modes	PBE+TS (cm^{-1})	PBE+G06 (cm^{-1})	Experimental (cm^{-1})
$A_{LA/LO'}$	90	90	89
$A_{TA/TO'}$	32	39	35
A_{LO}	893	867	-
A_{TO}	1575	1576	-
$\Gamma_{TO'}$	41	55	42
$\Gamma_{LO'}$	127	128	127
$\Gamma_{LO/TO}$	1576	1596	1581
Γ_{ZO}	893	873	868
$\Gamma_{ZO'}$	123	209	148
M_{ZA}	478	485	471,465,451
M_{TA}	652	638	630
M_{ZO}	656	649	670
M_{LA}	1320	1333	1290
M_{LO}	1355	1357	1321
M_{TO}	1356	1360	1388,1389
K_{ZA}	554	543	482,517,530
K_{ZO}	559	560	588,627
K_{TA}	1004	992	-
$K_{LA/LO}$	1213	1226	1184,1202
K_{TO}	1302	1330	1313,1291
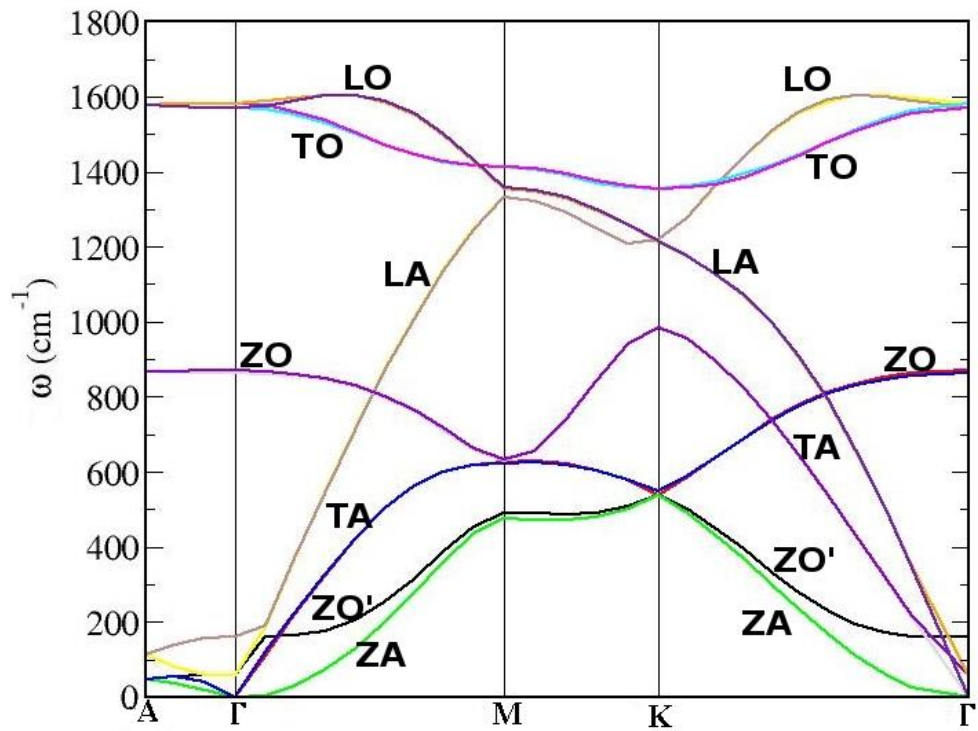
Figure 5-21: Dispersion curve of graphite using PBE+G06 functional for ultrasoft pseudopotential and finite displacement scheme.
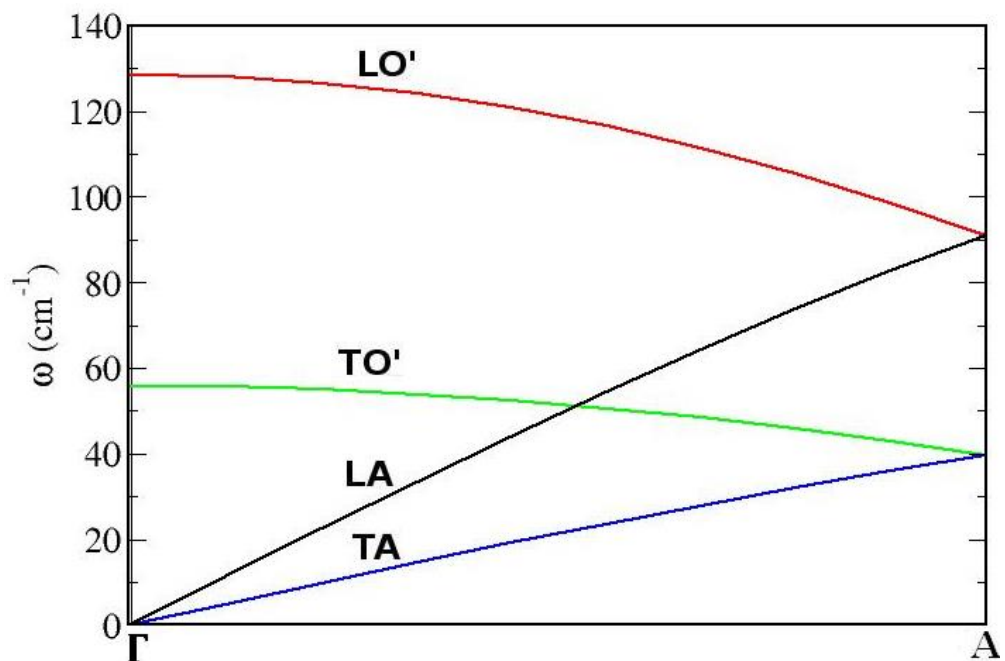
Figure 5-22: Low frequency dispersion curve using the PBE+G06 functional.
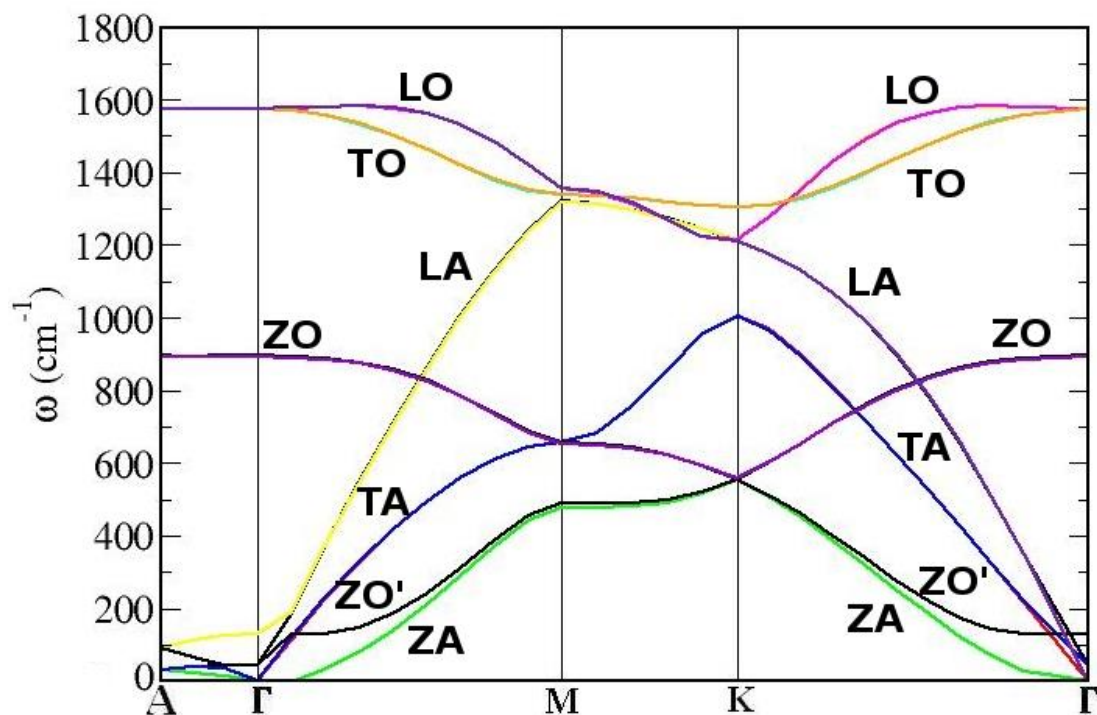
Figure 5-23: Dispersion curve of graphite using PBE+TS functional along high symmetry directions.
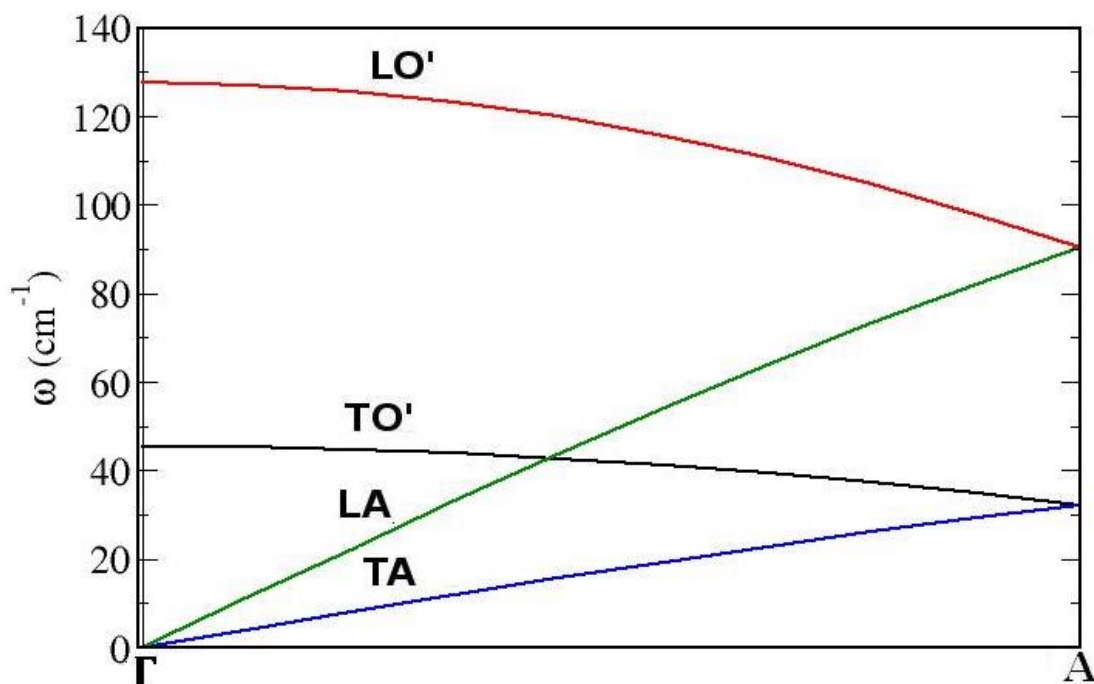
Figure 5-24: Low frequency dispersion curves using the PBE+TS functional.

The calculated values for out of plane (127 cm^{-1}) and out of phase (41 cm^{-1}) modes shown in Figure 5-25 are found to be in good agreement with the experimental values 127 cm^{-1} (15.7 meV) and 42 cm^{-1} (5.2 meV) as cited by Mohr et al. (2007). The out of phase mode of vibration has 2% lower frequency than the experimental value of frequency but the out of plane mode of vibration has exactly the same frequency as reported by experimental studies. This is the first accurate ab initio study of dispersion corrected low frequency modes of vibration. The calculated low frequency modes of vibration also seem to be consistent with the study of Reich and Thomsen (2009) who measured the modes of vibration for the graphite system using Raman spectroscopy.
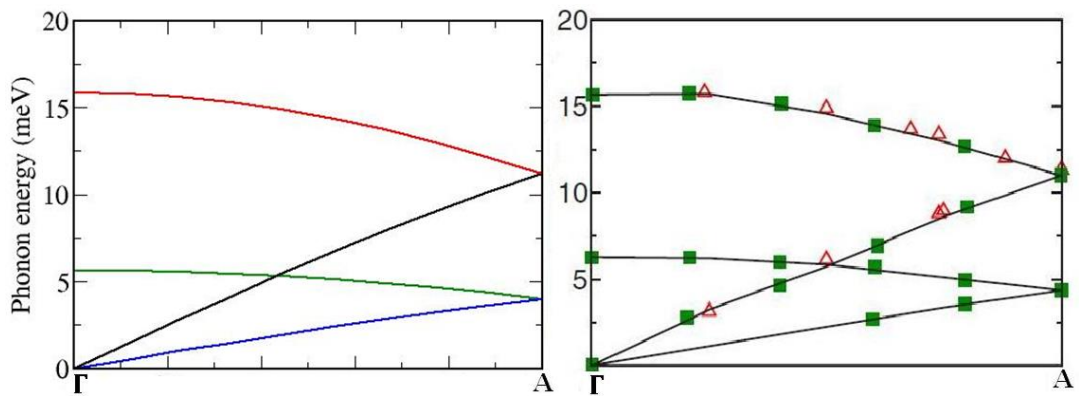
Figure 5-25: (Left) Low frequency dispersion curve using the PBE+TS functional along $\mathbf{\Gamma} - \mathbf{A}$ direction; (Right) Open triangles represent the inelastic x-ray scattering data and full squares are present neutron scattering data (Nicklow et al., 1972, Mohr et al., 2007).

Figure 5-26 shows dispersion curves for a $3 \times 3 \times 1$ supercell along high symmetry directions ΓA, ΓL, and ΓH of the Brillouin zone. The dispersion curve for a $4 \times 4 \times 2$ supercell shown in Figure 5-27 has been calculated using the high symmetry directions different from the above study in order to complete the study in Brillouin zone. Here, the relative coordinates in reciprocal space of points of the special symmetry are $\Gamma = (0,0,0)$, $A\left(\frac{1}{2},0,0\right)$, $L = (0,\frac{1}{2},\frac{1}{2})$ and H = (-1/3,2/3,0).
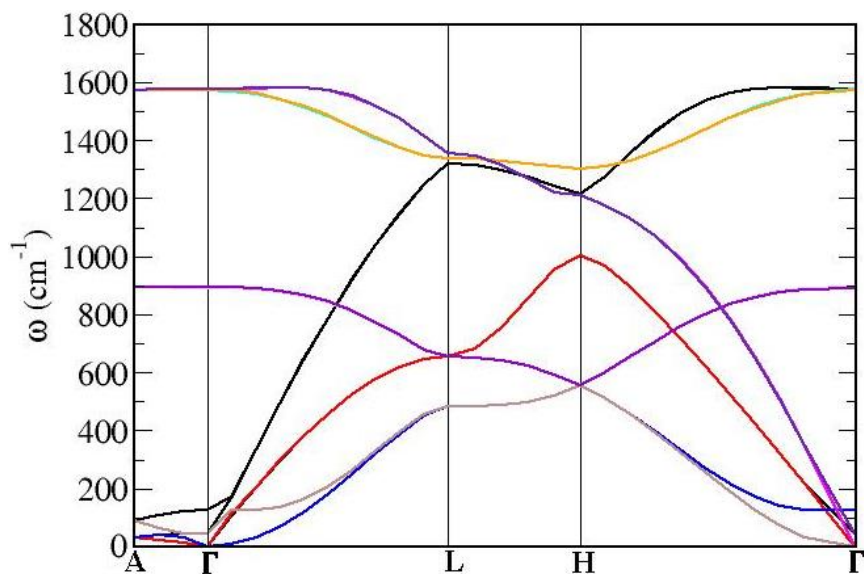
Figure 5-26: Dispersion curve of graphite using the using $3 \times 3 \times 1$ supercell by PBE+TS functional along high symmetry direction.
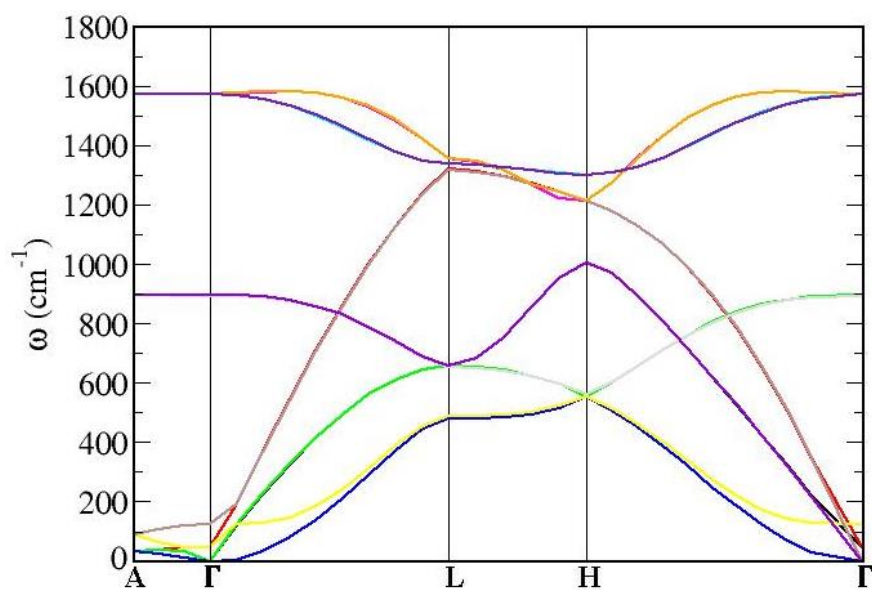
Figure 5-27: Dispersion curve of graphite using $4 \times 4 \times 2$ supercell by PBE+TS functional along high symmetry direction and k points mesh $16 \times 16 \times 8$.

5.10.   Vibrational Density of States

The vibration density of states for hexagonal graphite was calculated using the equation (4.14) for the PBE+TS functional. The system was geometry optimized before performing the calculation of density of states. The frequencies were broadened using a Gaussian function of half width half maximum ($1 cm^{-1}$) and integrated over the Brillouin Zone using a fine k-point mesh having 288 k-points. We repeated the calculation by varying the k-points grid to ensure the convergence of the frequencies. The calculations were repeated at denser k-points grid in order to reduce the noise in density of states. The smearing parameter was also adjusted to value of 0.4 eV to facilitate convergence of the frequencies. The same calculation was performed using the Gaussian broadening of $2 cm^{-1}$, $5 cm^{-1}$, $10 cm^{-1}$ and $50 cm^{-1}$. The smooth density of states was found at the larger Gaussian broadening.
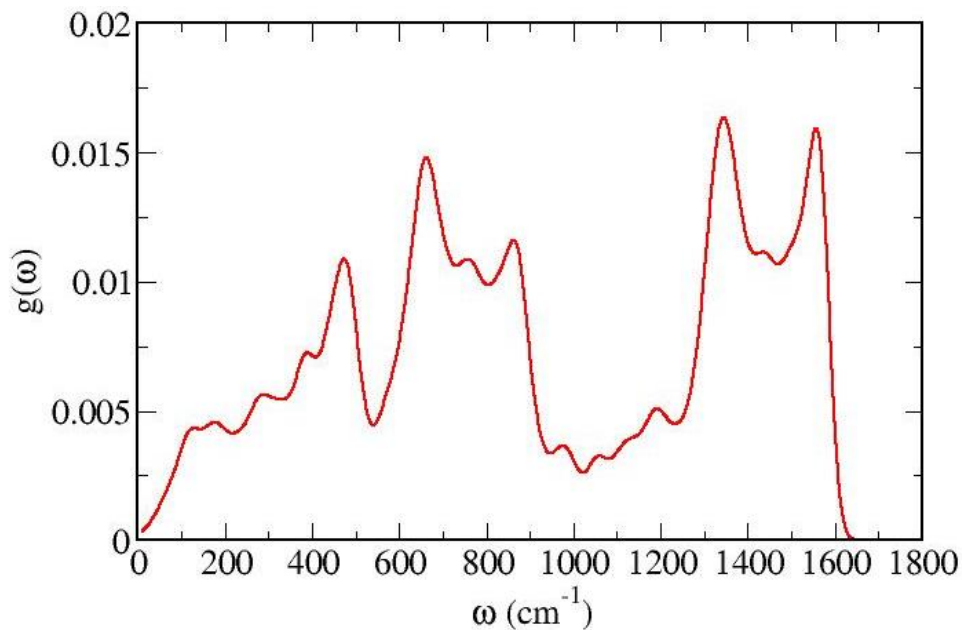
Figure 5-28: Vibrational density of states of graphite system using the PBE+TS functional.

Two important peaks were found at the $1574 cm^{-1}$ and $474 cm^{-1}$ which could be compared with the values $1601 cm^{-1}$ and $466 cm^{-1}$ given by Nicklow et al. (1972) on the basis of an axially symmetric model. The typical D band peak for graphite was calculated at $1344 cm^{-1}$. Moreover, peaks were also calculated at the values $178 cm^{-1}$,

660 cm^{-1} and 862 cm^{-1}. The calculated trend of peaks compares well with those reported by Vitali et al. (2004) using LDA–DFT.

5.11.   Structural and Vibrational Study of Rhombohedral Graphite

The graphite rhombohedral unit cell consists of two atoms. The atoms were placed at the positions A(0.16400 0.16400 0.16400) and B(-0.16400 -0.16400 -0.16400) respectively in a box. The rhombohedral graphite structure (Lipson and Stokes, 1942) has an ABC stacking, with half of the atoms directly below the atoms in adjacent planes and directly above the hexagonal ring centre, while the other half of the atoms directly above the atoms and below the hexagonal ring centres as shown in Figure 5-30. The lattice parameter and bond angles used in calculations were a=b=c=3.635 Å and $\alpha = \beta = \gamma$=39.49^0. On-the-fly (OTF) pseudopotentials were generated by CASTEP and determined at a cut-off energy 350 eV, which guaranteed the convergence of lattice parameters and total energies to less than 1meV per atom. The ultrasoft pseudopotential (Vanderbilt, 1990) was employed to model the electron-ion interactions. Brillouin zone sampling was obtained using the Monk-Pack (Monkhorst and Pack, 1976) k-points grid of size 8×8×8. The structure of symmetry group C$_i$ was geometrically optimized using the BFGS method. Forces were zero due to symmetry of structures. The dispersion corrected TS scheme (Tkatchenko and Scheffler, 2009) along with the PBE functional (Perdew et al., 1996) was also applied to perform the geometry optimization.

Following the geometry optimization, the calculated value of inter planar distance was about 3.34 Å at P = 0 GPa. A less than 1% error was found between calculated and experimental values. The system was fully relaxed to optimize all the atomic position of atoms until maximum force and stress had values less than 0.05 ($\frac{eV}{Å}$) and 0.1 GPa respectively and each atom is moved less than 10^{-3} Å. The effect of pressure on inter layer distance for rhombohedral graphite was determined by performing further optimization. Table 5-8 shows good agreement with the XRD data given by Wang et al. (2012) who investigated the structures of carbon by applying the compression and decompression at room temperature. It was found that interlayer distances have been decreased with increase in pressure.

Table 5-8: Interlayer distance corresponding to pressure for graphite using PBE+TS functional.

Pressure (GPa)	Interlayer Distance d (Å)	Experimental d (Å)
0	3.34	3.35
14.1	2.9	3.0
23.8	2.74	2.9
29.3	2.67	2.8

The vibrational frequencies of a graphite supercell $2\times2\times2$ were performed using the ab initio supercell method (Ye et al., 2004). The atom was displaced 0.01 Å within the cut off radius 10 Å to find the force constant and dynamical matrices. The smearing parameter was also adjusted to 0.4 eV for the convergence of the frequency. The dispersion corrected TS scheme (Tkatchenko and Scheffler, 2009) along with PBE functional (Perdew et al., 1996) was also applied to include the long range interaction in calculating the vibrational frequencies. The dispersion curve of rhombohedral graphite along the high system direction is shown in Figure 5-29.
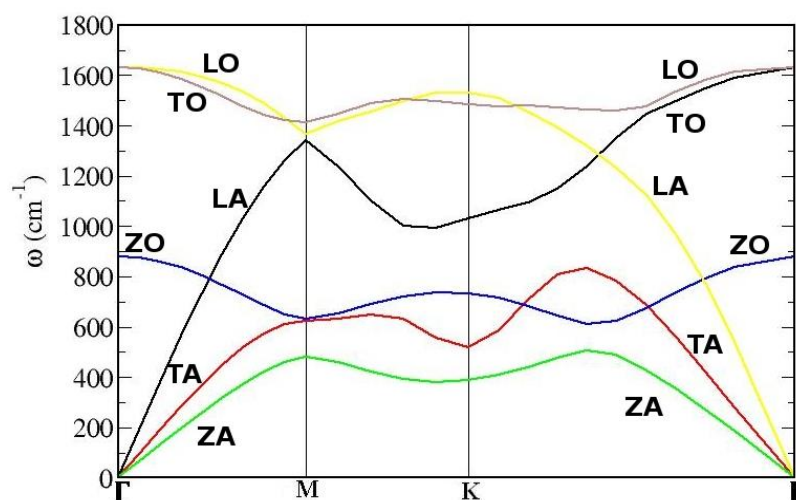
Figure 5-29: Dispersion curve of rhombohedral graphite using PBE+TS functionals along high symmetry direction.

Unlike the hexagonal graphite, rhombohedral graphite has no crossing ZA and ZO modes at K-point of the hexagonal Brillouin zone. LA and LO modes coincide at the M-point. Unlike the hexagonal graphite, LA and LO modes do not the cross at the K-point. This is due to different geometrical structures for the hexagonal and rhombohedral graphite. The LA and TA modes of vibrations have been calculated along $\Gamma = (0,0,0)\ to\ \mathbf{Z} = \left(\frac{1}{2},\frac{1}{2},\frac{1}{2}\right)$ along the symmetry direction of Brillouin zone shown in Figure 5-30 for rhombohedral graphite. The frequencies of LA and TA modes are 154 cm^{-1} and 47 cm^{-1} respectively at Z-symmetry point are shown Figure 5-31 and the arrows in Figure 5-32 show the direction of vibration of these modes.
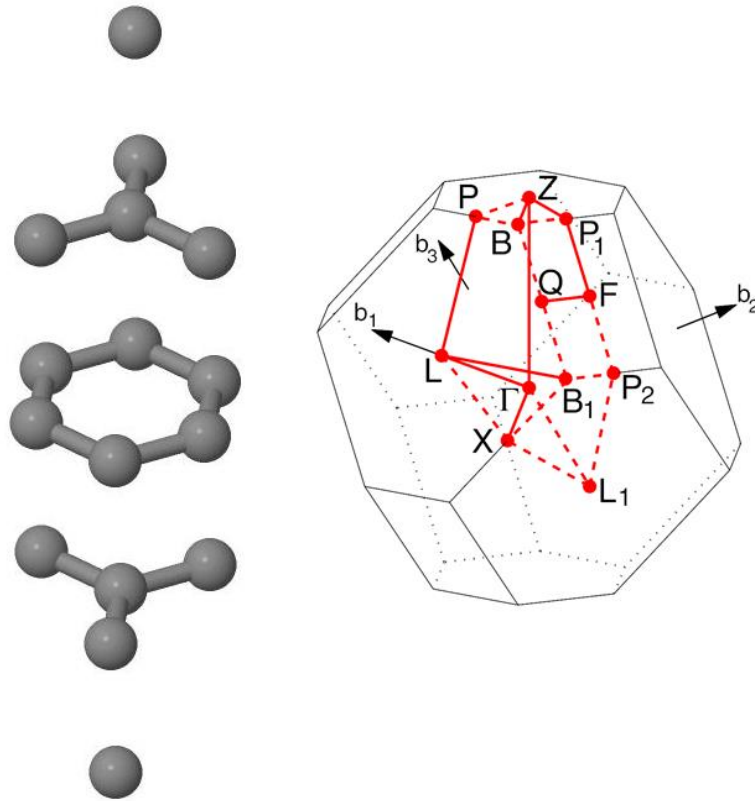
Figure 5-30: (Left) ABC-Stacking rhombohedral graphite; (Right) The Brillouin zone of rhombohedral lattice, with high symmetry k-points marked and b$_1$, b$_2$ and b$_3$ are reciprocal lattice vectors (Setyawan et al., 2010).
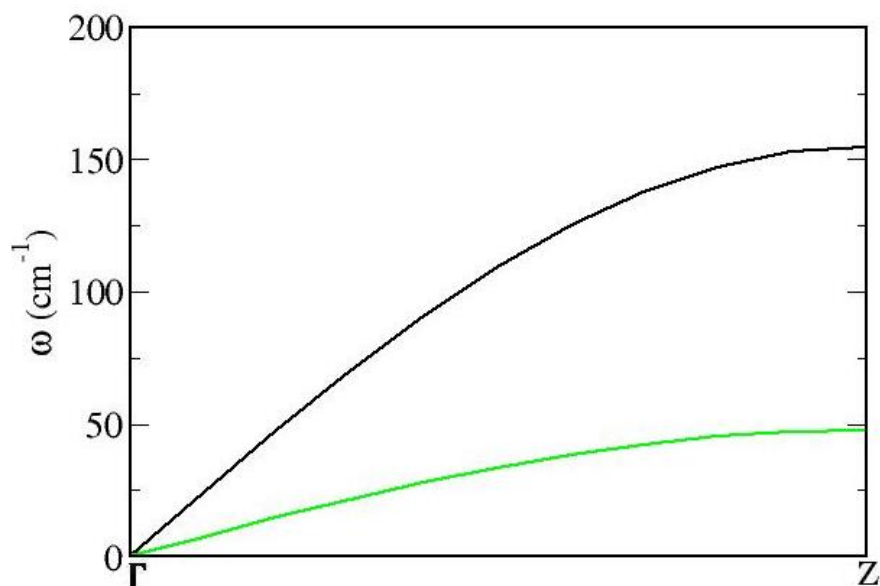
Figure 5-31: Frequency of rhombohedral graphite along the $\mathbf{\Gamma - Z}$ direction.

Figure 5-32: (Left) LA mode of vibration of frequency 154 cm^{-1}; (Right) TA mode of vibration of frequency 47 cm^{-1}.

5.12.   Summary

Following the geometry optimization of graphite system using the pseudopotential method, structural geometries have been determined. The band structure of graphite and graphene has been studied using the generalized gradient approximation. The LDA and GGA exchange and correlation functionals have been used to find the vibrational frequencies of graphite using the ab initio finite displacement method.

The vibrational frequencies of graphite have been found using the dispersion corrected functionals in order to include the long range interactions. The vibrational density of states has been explored using the PBE+TS functional. The structural and dynamical properties of graphite have also been studied using the PBE+TS functional.

5.13.   Conclusions

The utilization of DFT-D functionals leads to an improved C-C bond length and inter layer distance in hexagonal graphite. The errors in calculated structural parameters were found to be less than 1% compared with experimental results. The band structure has confirmed that graphite is a zero band gap semi-conductor material. The DFT-D functional also produced better results for the frequencies in graphite compared with the results without dispersion corrected functionals. The TS dispersion corrected scheme was found to be better than the G06 dispersion corrected scheme in evaluating the phonon dispersion curve of graphite. The structural and vibrational properties were also evaluated for the rhombohedral graphite using TS dispersion corrected scheme. The calculated value of interlayer distance was found to be comparable with the experimental value. The low frequency rhombohedral modes were investigated but no experimental study was found for comparison.

Chapter 6. Carbon Nanotubes for Hydrogen Storage

6.1.   Introduction

CNTs are considered as potential candidates to store hydrogen. The reaction energies of hydrogen in atomic and molecular forms with carbon nanotubes has been calculated using the generalized gradient approximation. The interaction of atomic hydrogen and molecular hydrogen with CNTs is vital in calculating the binding energies and band gaps in hydrogenated CNTs. In the present study, each hydrogen atom has been externally bonded with carbon to investigate chemisorption with a value of gravimetric density at 7.74 wt. %. This first principles study has been carried out to investigate the chemisorption of hydrogen with respect to diameters and chirality of CNTs. The vibrational study of hydrogenated CNTs is also used to explore the C-H modes of vibration.

The harmonic approximation was used to study the thermodynamic properties of the materials. The partition functions of statistical physics have been used to investigate the rotational and translational free energy of diatomic gases like H_2. Following the optimized geometry and phonon calculations, free energy has been investigated to determine the hydrogen release temperatures.

6.2.   Aims

The following are the aims in this study of hydrogenated CNTs.

- To determine the binding energies and band gaps of exo-hydrogenated zigzag and armchair CNTs using DFT PBE-GGA (Perdew et al., 1996) functional.

- To study the complete vibrational information of hydrogenated CNT by means of vibrational density of states and dispersion curves using PBE-GGA (Perdew et al., 1996) functional.

- To utilise the results of phonon calculations and statistical thermodynamics to determine the vibrational, rotational and translational free energies of hydrogen molecule.

- To utilise the results of phonon calculations and statistical thermodynamics to predict hydrogen releasing temperatures in hydrogenated armchair and zigzag CNTs.

6.3.   The Convergence Tests

Convergence testing was carried out to determine the optimum computational parameters to use for geometry optimization of structure. As the number of k-points and E_{cut} has been increased, the calculated ground state moves towards the actual ground state energy of system. However, increasing the number of k-points and E_{cut} can increase the computational expense. In this study, a convergency criterion of less than 1meV per atom has been used. These tests were performed with the same k-point grid and cut off energy for the reactants and product. Here, convergence tests of only one type of CNT were being discussed and calculations of other CNTs were also studied before calculating the binding energies of these systems.

6.4.   Hydrogenated CNT(4,4)

The hydrogenated CNT(4,4) was placed in a cell with dimensions $a = 13.6797$ Å, $b = 13.6797$ Å and c = 2.4630 Å and corresponding angles were $\alpha = 90^0$, $\beta = 90^0$ and $\gamma = 120^0$. In order to avoid the interaction between the CNTs, the closest distance between H-H atoms for the two adjacent CNTs was about 8.2 Å. The convergence tests with respect to both k-point sampling and E_{cut} were carried out. First, the number of k-points were varied by fixing the E_{cut} (540 eV) and single point energy calculations were performed using various sets of k-points. Table 6-1 displays the k-point convergence testing for the hydrogenated CNT using the OTF pseudopotential. The 10 k-points from $1 \times 1 \times 20$ Monk-Pack grid (Monkhorst

and Pack, 1976) were used to sample the Brillouin Zone. The total energy converged for the CNT(4,4) system within the range of 1meV. To find the optimum E_{cut} required, a series of single point energy calculations were performed by fixing the k-points. The total energies of CNT (4,4)H were converged within 1meV as shown in Figure 6-1. Hence a value of cut-off energy of 540 eV was a better choice in our calculation.

Table 6-1: Calculated energies of CNT(4,4)H using different k-points while fixing $E_{cut} = 540$ eV.

Number of k-points	Total Energy (eV)	Total Energy per atom (eV)
1	-2720.0443	-85.001386
3	-2757.9194	-86.18498
5	-2757.9531	-86.18603
8	-2757.9562	-86.18613
10	-2757.9564	-86.18614
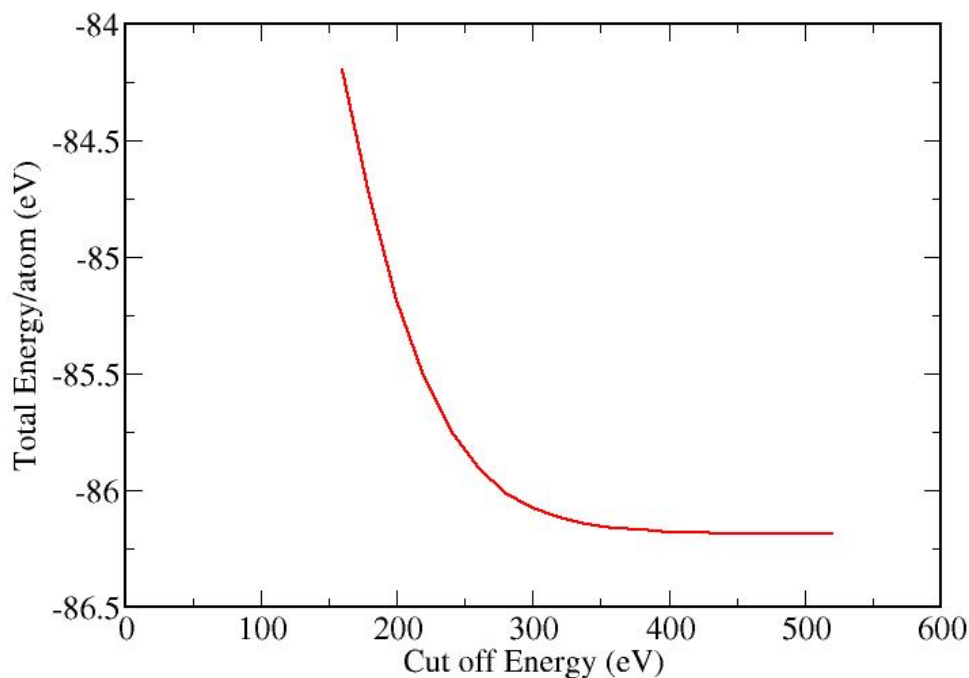
Figure 6-1: Cut-of energy versus total energy per atom of CNT (4,4)H.

6.5.   CNT(4,4) and the Hydrogen Molecule

In order to choose the fine grid scale, single point calculations were performed by varying the size of the grid. The fine grid scale parameter defines a denser grid necessary to deal with the addition of hard augmented charge densities to the smoother valence charge density in the ultra-soft pseudopotential method. The values of total energy are shown in Figure 6-2 and these values were found to be converged within the value of 1meV when changing the fine grid scale from 2.0 to 3.0. Thus a 2.0 fine grid scale has been used in the calculations of CNTs.
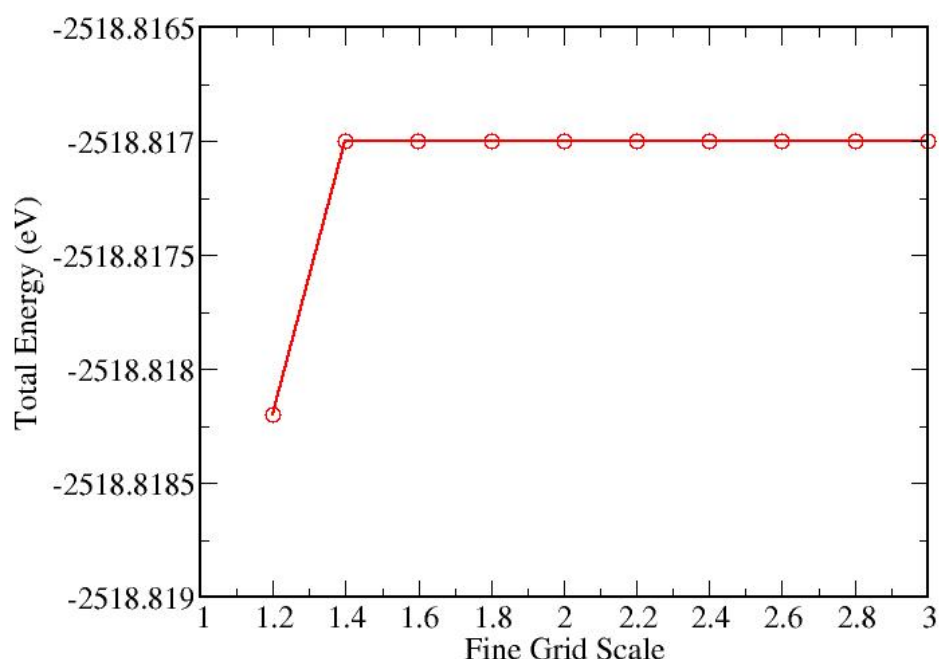
Figure 6-2: Choice of fine grid scale corresponding to total energy of CNT (4,4).

The number of k-points were changed by fixing E_{cut} (540 eV) and single point energy calculations were carried out using various sets of k-points.

Table 6-2 displays the k-point convergence testing for the hydrogenated CNT using an OTF pseudopotential. The Brillouin Zone was sampled using Monk-Pack grid (10 k-points) $1 \times 1 \times 20$ (Monkhorst and Pack, 1976).

Table 6-2: Calculated energies of CNT(4,4) using different k-points while fixing E_{cut} = 540 eV.

Number of k-points	Total Energy (eV)	Total Energy per atom (eV)
1	-2503.0021	-156.438
3	-2518.9024	-157.431
5	-2518.8545	-157.428
8	-2518.8283	-157.427
10	-2518.8170	-157.426

Table 6-3 displays the k-point convergence testing for the hydrogen molecule using an OTF pseudopotential. The Brillouin Zone was sampled by the Monk-Pack grid $1 \times 1 \times 20$ (10 k-points) (Monkhorst and Pack, 1976) for the hydrogen molecule.

Table 6-3: Calculated energies of hydrogen using different k-points while fixing E_{cut} = 540 eV.

Number of k-points	Total Energy (eV)	Total Energy per atom (eV)
1	-31.5481114	-15.774056
3	-31.5481088	-15.774054
5	-31.5481087	-15.774054
8	-31.5481112	-15.774056
10	-31.5481133	-15.774057

To find the optimum E_{cut} required, a series of single point energy calculations were carried out by fixing the k-points. The total energies of CNT (4,4) were converged within 1meV as shown in Figure 6-3. Similarly, optimum E_{cut} = 540 eV was also found for hydrogen molecule as shown in Figure 6-4. The total energy of CNT(4,4) converged within a range of 1meV/atom as shown in Figure 6-5 for fixing the dimension of cell. The inter layer distances have increased to reduce the interaction between the CNTs. Lattice parameters were determined in order to construct the isolated CNTs.
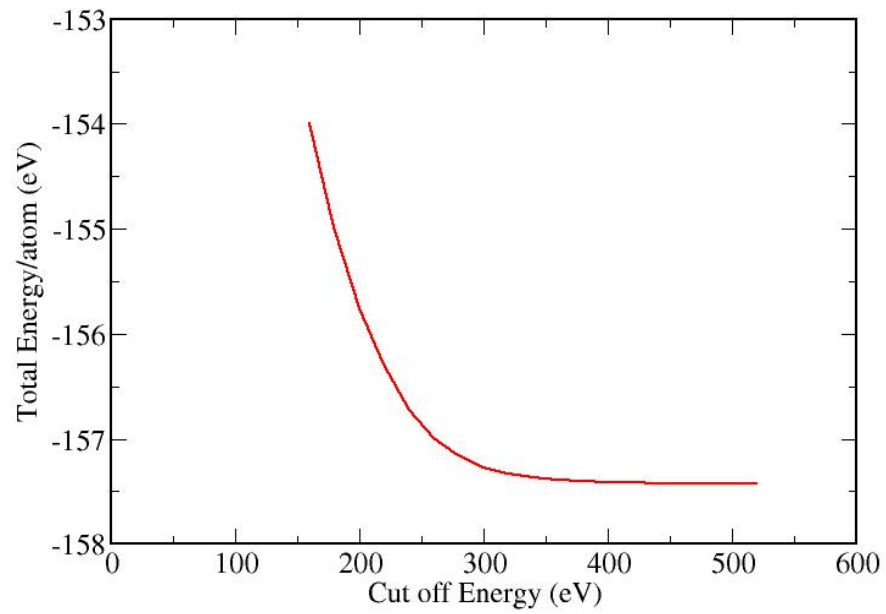
Figure 6-3: Cut of energy versus total energy per atom of CNT (4,4) .
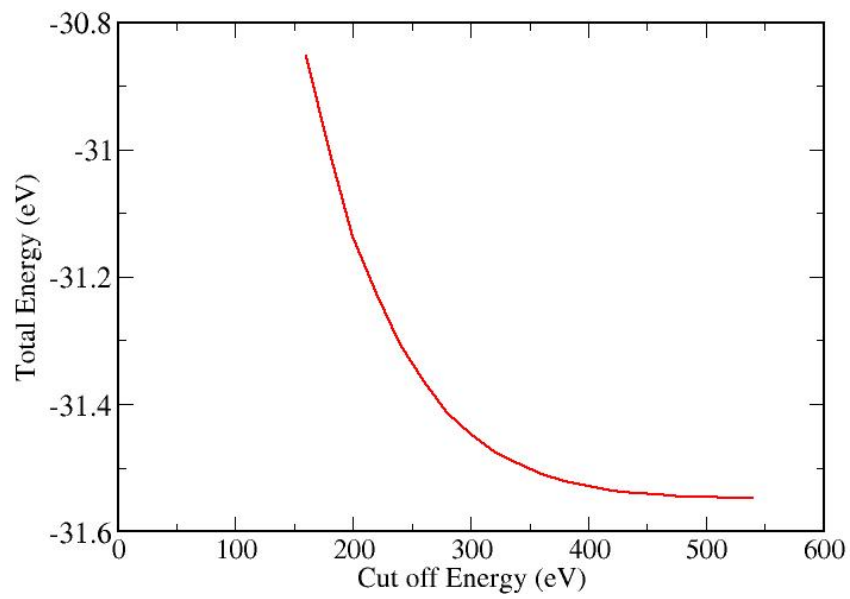
Figure 6-4: Cut off energy for the convergency of H_2 molecule.
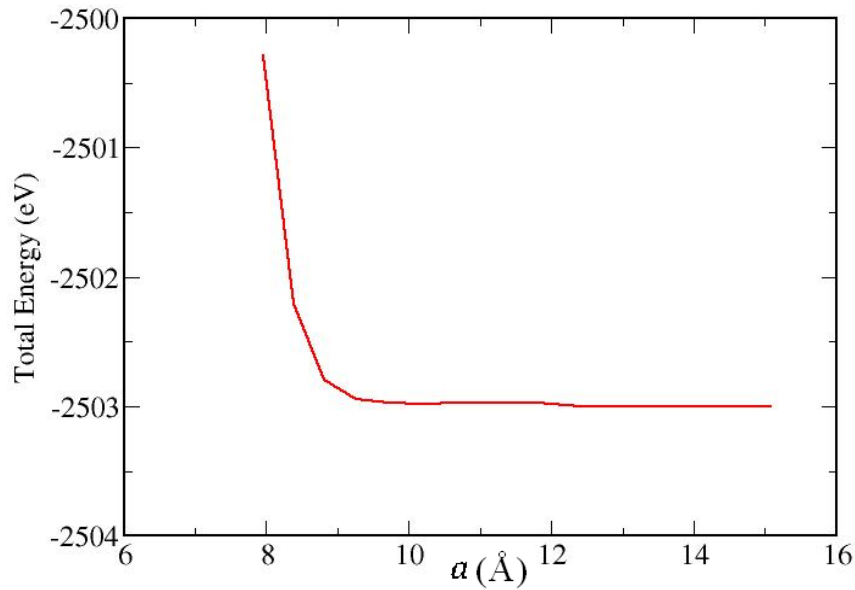
Figure 6-5:   The Convergency of the electronic energy of CNT (4,4) with respect to lattice parameter a.

6.6.   Binding Energy Calculations of Exo-Hydrogenated CNTs

In order to calculate the binding energy, initial geometries were generated using the Tube Gen tool (Frey and Doren, 2011) based on the hexagonal unit cell. The hydrogen was attached externally with each carbon atom and the length of the C-H bond is 1.10 Å. This study is based on the assumption that all carbon atoms in a nanotube are hybrid with hydrogen atoms from outside as shown in Figure 6-6. The cut off energy used in these calculations is 540 eV. The Brillouin zone was sampled using a Monk-Pack (Monkhorst and Pack, 1976) grid of 1×1×20 of k-points. An ultrasoft pseudopotential (Vanderbilt, 1990) was used along with a GGA-PBE functional (Perdew et al., 1996) to perform these calculations and on the fly (OTF) pseudopotentials were generated by CASTEP code. For the pseudopotential, the cut off radii $r_{c,H}$ and $r_{c,C}$ have the values 0.423 Å and 0.741 Å respectively. The distance between H-H atoms for two CNTs was kept in the range of 6-9 Å in order to generate isolated hydrogenated CNTs. The CNT structure was examined to consider the CH rotation along the high symmetry direction as shown in Figure 6-6. Single point energy calculations were performed to find the optimum orientation of CNT (4,4)H. Our calculated local CCH-bond angles (α_{CCH}) curve in Figure 6-7 are comparable with the previous calculations of Yildirim et al. (2001), who obtained the optimum orientation when the CH bond is tilted about c-axis in arm chair CNTs.
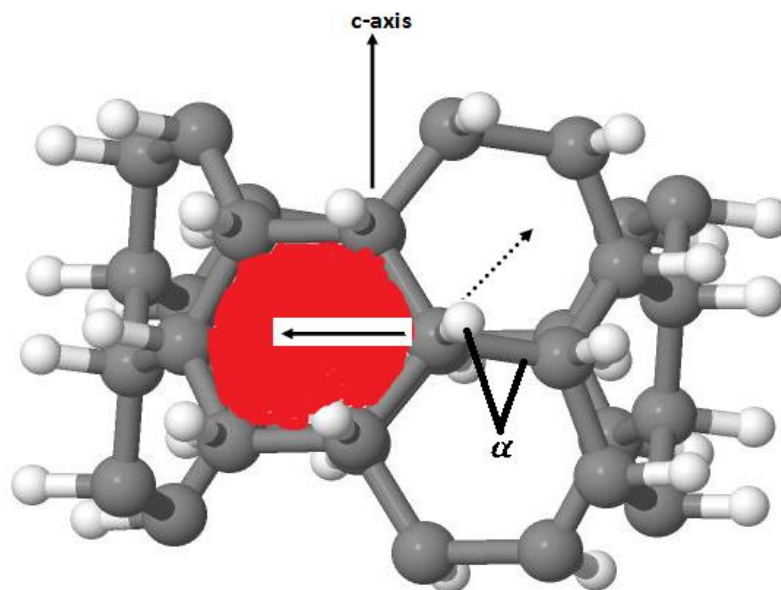
Figure 6-6: Optimized structure of CNT(4,4)H, direction of arrows show the rotation of CH bond along the symmetry direction. The arrows indicate the possible directions of rotations of CH bond (Yildirim et al., 2001).
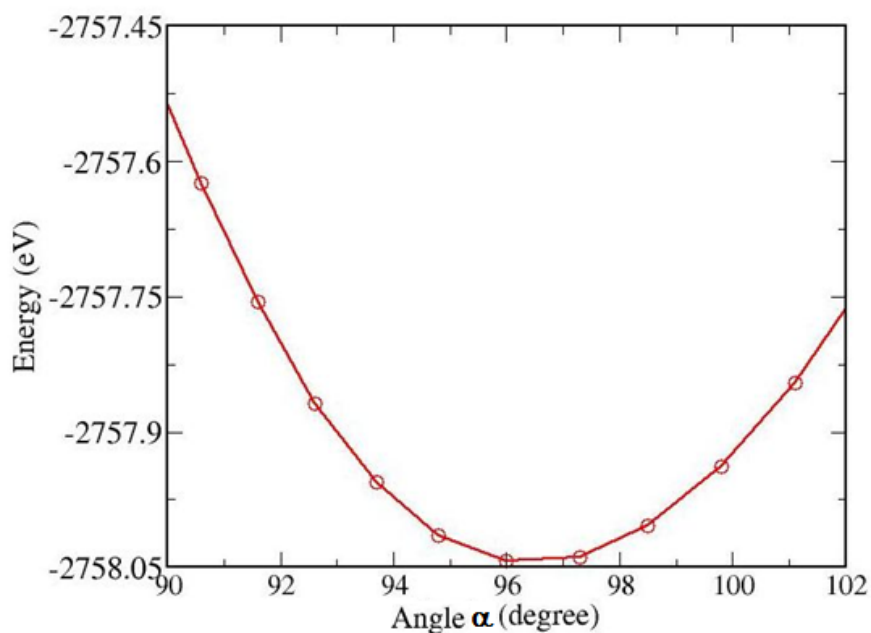
Figure 6-7: The minimum energy curve of CNT(4,4)H as CH is rotated along high symmetry direction.

Similarly, optimum orientation was also obtained for hydrogenated zigzag CNT(4,0)H along the c-axis when CH bond tilted along the positive and negative direction. The structure in is drawn in Figure 6-8 to show the CH bond tilt along the

z-axis. The single point calculations were carried out to find the optimum bond angle for the CNT(4,0)H as shown in Figure 6-9.
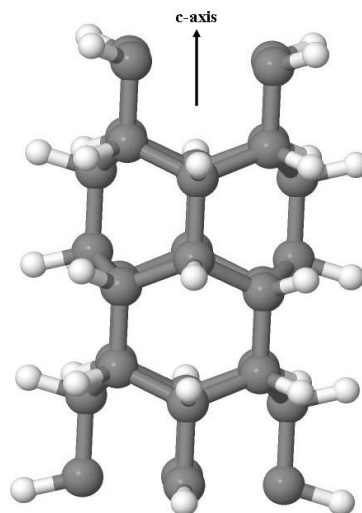
Figure 6-8: Optimized structure of CNT(4,0)H, tilting of CH bond along c-axis.
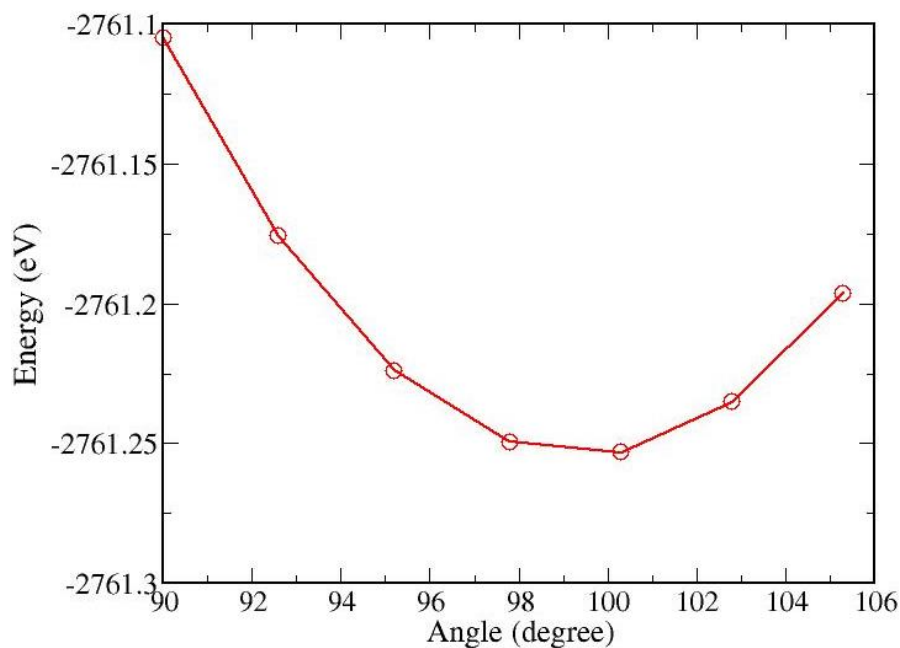
Figure 6-9: The minimum energy curve of CNT(4,0)H as CH is rotated along high symmetry direction.

All the attached hydrogen atoms were shifted by small displacement along the z-axis and the structures were relaxed to ensure the equilibrium orientation of bonds along the z-axis. All the structures of hydrogenated CNTs were fully relaxed

by optimizing all the positions along the tube axis until maximum force and stress are less than 0.05 $(\frac{eV}{\AA})$ and 0.1 GPa respectively and each atom was moved less than 10^{-3}Å. The H-H distance between two CNTs was calculated in the range of 6-9Å in order to generate isolated hydrogenated CNTs as shown in Figure 6-10. Table 6-4 displays the calculated total energies of CNTs and hydrogenated CNTs.
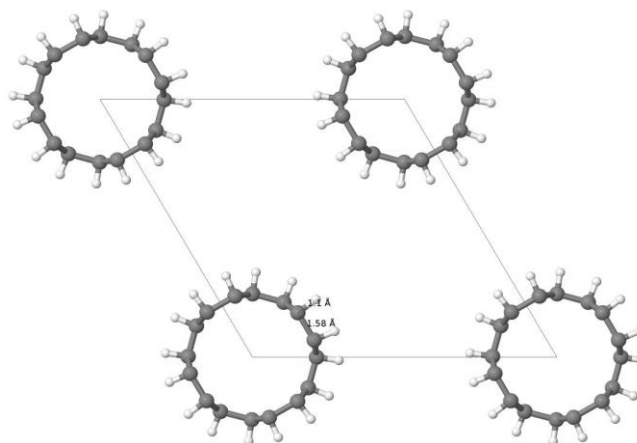
Figure 6-10: Geometry optimized structure CNT(4,4)H to measure the H-H distance.

Table 6-4: Total energy of CNTs and Hydrogenated CNTs for optimized structure.

CNT(n,m)	Total Energy (eV)	CNT(n,m)H	Total Energy (eV)
(4,4)	-2518.847863266	(4,4)H	-2770.619520289
(5,5)	-3150.494817047	(5,5)H	-3459.679605947
(6,6)	-3781.849060137	(6,6)H	-4148.377912475
(8,8)	-5044.146708149	(8,8)H	-5525.326431653
(9,9)	-5675.154497031	(9,9)H	-6213.630535465
(10,10)	-6306.135001431	(10,10)H	-6901.929519107
(4,0)	-2511.175834208	(4,0)H	-2777.295780610
(5,0)	-3143.855111284	(5,0)H	-3468.826404637
(6,0)	-3776.233255247	(6,0)H	-4159.271076588
(7,0)	-4408.196140036	(7,0)H	-4848.981140956
(8,0)	-5039.896379711	(8,0)H	-5538.267078178
(9,0)	-5671.346285029	(9,0)H	-6227.255952379
(10,0)	-6302.782187364	(10,0)H	-6916.030402765

Bond lengths and bond angles given in Table 6-5 are determined for the optimized zigzag and armchair nanotubes structures. Two types of bond lengths have

been calculated. In the first type the CC-bond length (d_{CC}) was found to increase with increase in diameters and in the second type the CC-bond length (d_{CC}) was observed to decrease with increases in diameters for zigzag CNTs. On the other hand, the length of both types of d_{CC} were observed to decrease with an increase in diameters (D) for arm chair CNTs. CCC bond-angles in both types of CNTs increase with the increase in diameters of CNTs.

Table 6-5: Optimized parameter of zigzag and armchair CNTs.

Materials	D (Å)	d_{CC} (Å)	CCC (degree)
CNT(4,0)	3.37	1.338,1.477	107.5,119.2
CNT(5,0)	4.14	1.408,1.452	111.1,119.9
CNT(6,0)	4.74	1.410,1.443	113.5,120
CNT(7,0)	5.98	1.418,1.434	115.2,120
CNT(8,0)	6.36	1.418,1.432	116.2,120
CNT(9,0)	7.01	1.420, 1.429	116.9,120.1
CNT(10,0)	7.89	1.423,1.426	117.4,120.1
CNT(4,4)	5.52	1.428,1.428	117.8,119.4
CNT(5,5)	6.78	1.424,1.427	118.5,119.7
CNT(6,6)	8.19	1.422,1.426	118.9,119.9
CNT(8,8)	10.88	1.421,1.424	119.3,120.1
CNT(9,9)	12.22	1.421,1.424	119.5,120.1
CNT(10,10)	13.59	1.421,1.424	119.5,121

The CNTs and hydrogenated CNTs were geometrically optimized. The Binding Energy per hydrogen was calculated using the expression (6.1) (Andreoni et al., 2012).

$$E_B(n) = (E(CNT) - E(CNT + nH))/n + E(H) \qquad (6.1)$$

In the equation (6.1), E(H) is an energy of an isolated single atom and its calculated value is in the present study about E(H) = -13.584 eV. Upon the hybridization, the value of the original CC- bond length(d_{CC}) was found to increases from 1.42 Å to 1.62 Å, which was typical for an sp^3 structure. From Table 6-6, it is seen that the CC-

bond length (d_{CC}) stretches more in arm chair carbon nanotubes than zigzag CNTs. Moreover, d_{CC} was also found to be dependent upon the diameters of CNTs. Our calculated d_{CC} was found to increase by about 9-12% for zigzag CNTs and by about 10-15% in arm chair CNTs. After hydrogenation, d_{CC} stretches more from the actual bond length 1.42 Å in zigzag CNTs as compared with arm chair CNTs. The CH-bond length (d_{CH}) is also found to have a weak dependence on the diameter of the tube. It is also observed that the value of d_{CH} decreases with the increase in diameters of CNTs.

.

Table 6-6: Various parameters of the fully optimized structures of exo-hydrogenated armchair and zigzag carbon nanotubes.

Materials	Formula	D(Å)	d_{CC} (Å)	d_{CH} (Å)	α_{CCC} (degree)	α_{CCH} (degree)
CNT(4,0)H	$C_{16}H_{16}$	3.71	1.544,1.562	1.103	112.8, 116.8	103.7, 105.5
CNT(5,0)H	$C_{20}H_{20}$	4.64	1.548,1.568	1.103	113.3, 121.8	100.3.104.2
CNT(6,0)H	$C_{24}H_{24}$	5.51	1.556,1.568	1.102	113.6, 124.5	98, 103.1
CNT(7,0)H	$C_{28}H_{28}$	6.80	1.565, 1.569	1.101	113.9, 126	96.4 ,102.3
CNT(8,0)H	$C_{32}H_{32}$	7.35	1.570,1.572	1.099	114.2, 127	95.2 ,101.6
CNT(9,0)H	$C_{36}H_{36}$	8.58	1.570, 1.579	1.097	114.4,127.5	94.4,101
CNT(10,0)H	$C_{40}H_{40}$	9.22	1.571,1.585	1.096	114.6,127.8	93.7,100.5
CNT(4,4)H	$C_{16}H_{16}$	6.29	1.558,1.583	1.099	112.5, 120.9	96.7, 98.7
CNT(5,5)H	$C_{20}H_{20}$	7.83	1.567,1.596	1.096	112.9,121.7	94.7, 97.2
CNT(6,6)H	$C_{24}H_{24}$	9.47	1.574,1.606	1.093	113.4,122	93.5, 96.3
CNT(8,8)H	$C_{32}H_{32}$	12.66	1.584,1.620	1.089	114.2, 122.2	92, 95
CNT(9,9)H	$C_{36}H_{36}$	14.04	1.587,1.625	1.088	114.5,122.2	91.5,94.6
CNT(10,10)H	$C_{40}H_{40}$	15.86	1.590,1.630	1.086	114.8,122.2	91.1,94.2
Cubane	C_8H_8	4.01	1.570	1.097	90	125.3

On the other hand, local CCH-bond angles (α_{CCH}) in arm chair CNTs deviate more than the ideal tetrahedral bond angle bond angle 109.5[0]. It is observed that CCH-bond angles (α_{CCH}) in zigzag CNTs are found to be closer to optimum

tetrahedral sp^3 bonding than those armchair CNTs. These results are comparable with the previous ab initio study of exo-hydrogenated CNTs which was performed by Yildirim et al. (2001).
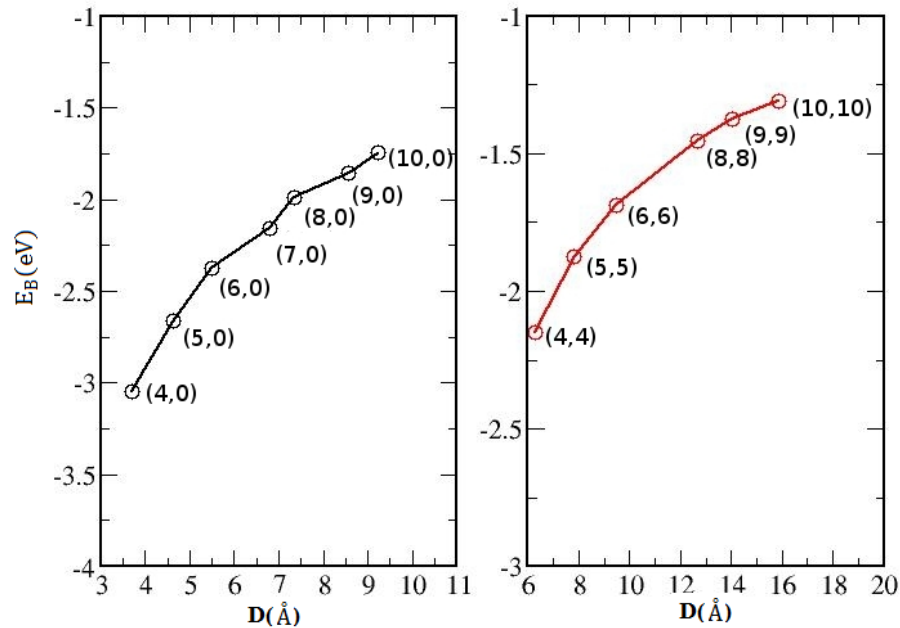
Figure 6-11: Binding energy as a function of diameters D of zigzag and arm chair CNTs.

The binding energies are proportional to the inverse of diameter (1/D) for the zigzag and armchair CNTs. The calculated values of binding energy for zigzag CNTs are found to be lowered compared with arm chair CNTs as shown in Figure 6-11. The calculated values of the binding energies are also found to be negative which indicate the energetically favourable adsorption. The values of binding energy are found to decrease with increase in diameters of CNTs. The present study is different than the study of Yilidirim's study regarding the treatment of zigzag CNTs. Yildirim et al. (2001) only considered the large diameter zigzag CNTs, however, small diameters CNTs produced the highest values for binding energies. Therefore, the present study was set out to perform the calculations from the small diameters to large diameters zigzag CNTs.

The hydrogen-carbon interaction has also been studied in cubane (C_8H_8) (Eaton and Cole, 1964). The cut off energy value 540 eV and Γ-point Brillouin zone were opted to perform geometry optimization. In this system, CCC-bond angles are 90^0 rather than 109.5^0 as for the tetrahedral sp^3 bonded system. The calculated values of C-C =1.570 Å and C-H = 1.097 Å were found to comparable with the experimental

values 1.570 Å and 1.097 Å respectively as cited in Maslov et al. (2009). The total energy for the optimized structure of cubane has a value -1383.2885 eV. The calculated value of binding energy of 4.01 eV/atom for cubane is less than the experimental value 4.42 eV/atom as cited in Maslov et al. (2009). The polyhedral molecule (cubane) represents the zero-dimensional case. However, we mainly focus on the properties of the hydrogen-carbon interaction in CNTs due to their unique one-dimensional nature and curvature.

The reaction energy per H as given in Table 6-7 was calculated using the relation (6.2) (Stojkovic et al., 2003) in order to find the stability and energetics of CH-bond formation.

$$E_r = E_{CNT-H} - E_{CNT} - \frac{n}{2}E_{H_2} \qquad (6.2)$$

where n is the number of hydrogens. In above relation, E_{CNT-H} is the total energy of chemisorbed hydrogenated CNT, E_{CNT} is the total energy of pristine CNT, and E_{H_2} is the total energy of an isolated hydrogen molecule.

Table 6-7 presents the values of binding energies of exo-hydrogenated CNTs by interaction of molecular hydrogen with CNTs. The electronic energy E_{H_2} of an isolated hydrogen molecule is calculated to be about -31.74 eV. The reaction energy has negative and positive values for molecular hydrogen in the gas phase. It is found that that reaction energies of hydrogenated zigzag CNTs have energetically favourable values at pressure p = 1bar for only small diameter nanotubes up to diameter 5.71 Å. At larger diameters zigzag CNTs and armchair CNTs have a reaction energy which becomes unfavourable for the hydrogen molecule. These findings can be compared with the experimental study of Talyzin et al. (2011) in which it was reported that molecular hydrogen could not react with nanotube walls at H_2 pressure of a few mega Pascal at moderately high temperatures. On the other hand, the reaction energy for atomic hydrogen was found to be highly favourable for zigzag and armchair CNTs. This study produced results which confirm the findings of a great deal of the previous work in this field.

Table 6-7: Reaction energy per Hydrogen for zigzag and arm chair CNTs.

Materials	E_r/H (eV)
CNT(4,0)	-0.7625
CNT(5,0)	-0.3785
CNT(6,0)	-0.0899
CNT(7,0)	0.1277
CNT(8,0)	0.2960
CNT(9,0)	0.4281
CNT(10,0)	0.5388
CNT(4,4)	0.1344
CNT(5,5)	0.4108
CNT(6,6)	0.5980
CNT(8,8)	0.8332
CNT(9,9)	0.9124
CNT(10,10)	0.9752

6.7.   Band Structure of Hydrogenated CNTs

Following the geometry optimization, band structures of CNT(4,4) and hydrogenated CNT(4,4) were calculated using the GGA-PBE functional. The k-point path was selected along symmetry $\Gamma - Z$ direction for the self-consistent band calculations. Figure 6-12 shows that the valence band and conduction band cross each other at Fermi level for CNT(4,4). This confirms the metallic nature of armchair CNT(4,4). Armchair CNTs are metallic. Zigzag CNTs have both metallic and semiconductor behaviour. The small diameter zigzag CNTs up to 4.74 Å are found to be metallic in nature due to high curvature. These findings seem to be consistent with the study of Zólyomi and Kürti (2004) who performed band structure calculations for small diameters CNTs using the LDA functional. However, Figure 6-13 shows that hydrogenated CNT(4,4) has a band gap between the top of valence band and bottom of the conduction band as shown in the band structure and corresponding density of states. This shows that hydrogenated CNT changes from metallic to semiconcuctor behaviour due to hydrogenation. The direct band gap at the Γ-point is calculated to

be 2.4505 eV for the hydrogenated CNT(4,4). The calculated value is found to be comparable with the value reported by Yildirim et al. (2001).
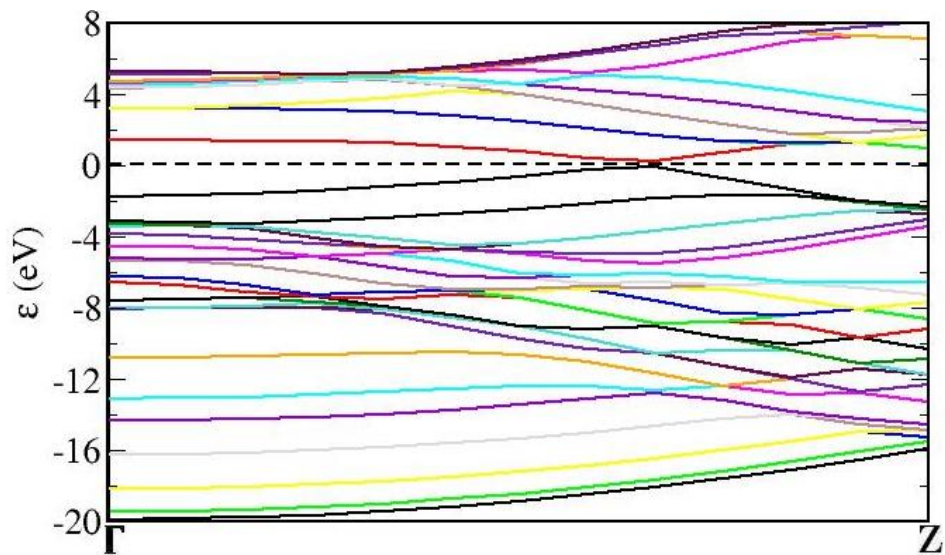
Figure 6-12: Band structure of CNT (4,4) using GGA-PBE functional.
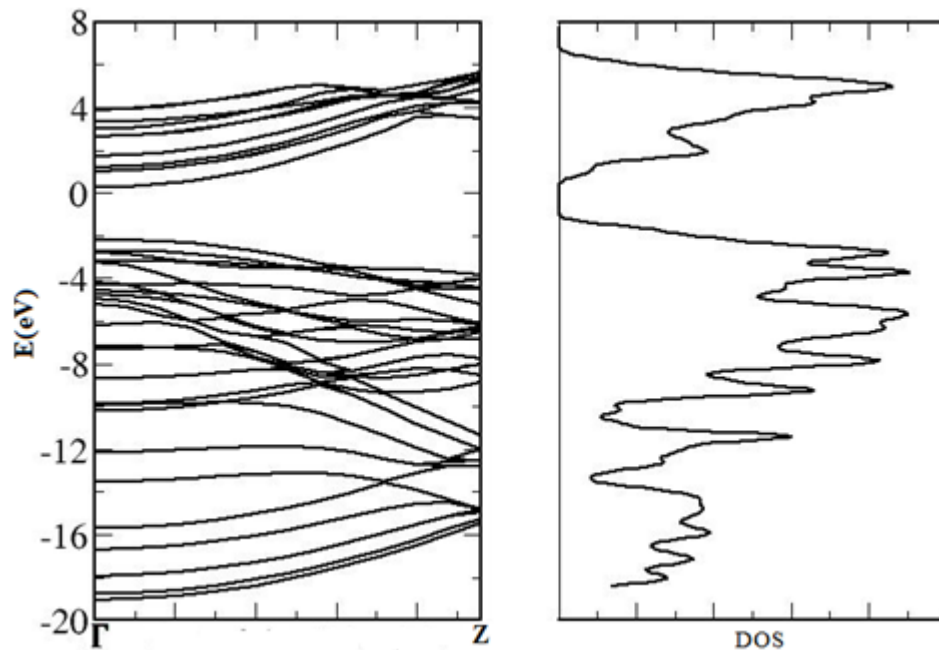
Figure 6-13: Band structure and density of states of CNT(4,4)H using GGA-PBE functional

The band gaps as a function of tube diameter are plotted in Figure 6-14 for hydrogenated zigzag and armchair CNTs. The values of band gap in zigzag and armchair hydrogenated CNTs decrease with increase of diameter. It is interesting to note that small diameter hydrogenated zigzag CNTs are found to be more stable

compared to large diameters. Contrary to findings of Yilidrim et.al (2001), band gaps of zigzag CNTs have relatively large values in the present study. This point was missing in Yilidrim's study as only large diameters of zigzag were considered.
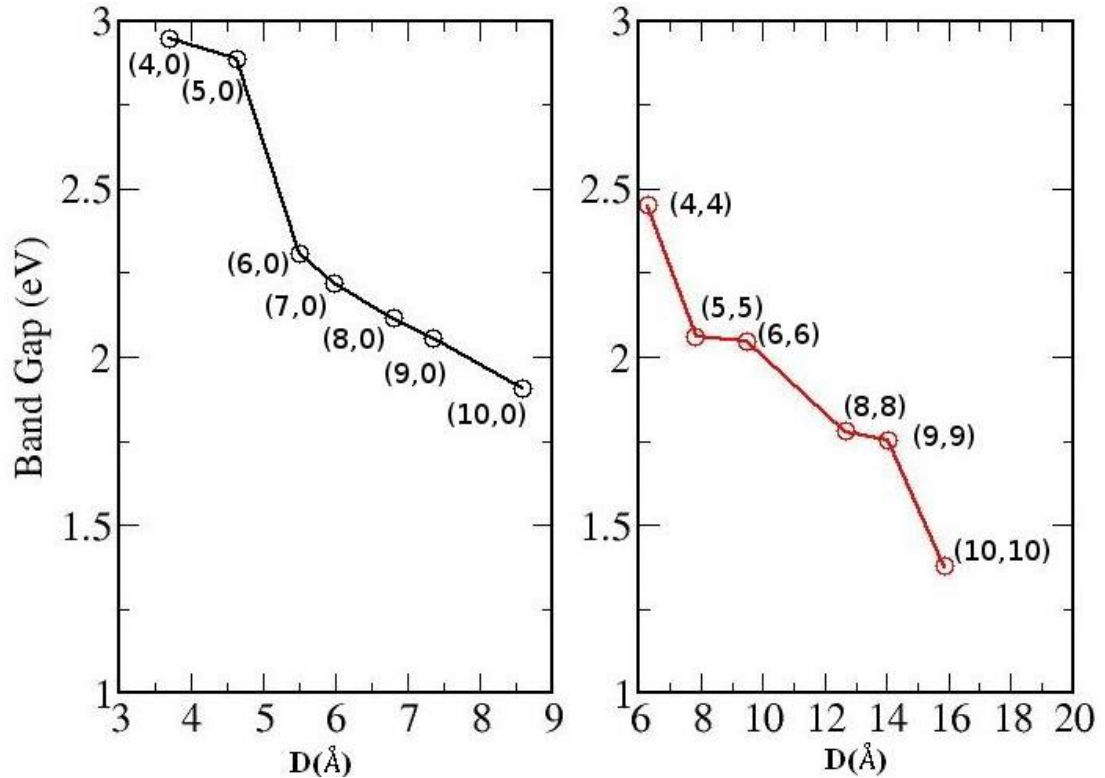
Figure 6-14: Band gap as a function of hydrogenated nanotubes diameters D.

6.8.   Vibrational Study of CNT(4,4)H

The vibrational density of states of hydrogenated carbon nanotubes have been calculated using CASTEP (Clark et al., 2005). For these calculations, the supercell approach was used to construct the dynamical matrix and the PBE–GGA functional was applied. A supercell of size $1 \times 1 \times 4$ was chosen. After this, q-points of $1 \times 1 \times 25$ mesh were chosen to integrate the Brillouin zone for the calculation of vibrational density of states. The value of geometry force tolerance was increased up to 0.1 $(\frac{eV}{\mathring{A}})$ in order to avoid imaginary frequencies. It is found that the peaks lie in the region 2875-2963 cm^{-1} (356-367 meV) due to sp^3 hybridization and C-H stretching modes as shown in Figure 6-15. This study seem to be consistent with study of Meletov et al. (2007) who mentioned the C-H stretching modes in a frequency region 2800-3000 cm^{-1} using Raman spectroscopy for hydrogenated CNT. The G band peak was found

at 1547 cm^{-1} for the vibrational density of states. The peak at 1423 cm^{-1} was due to a bending mode of vibration. A more intense D band in spectrum at the value of 1310 cm^{-1} was due to the structural disorder of hydrogenated CNT. The ratio of intensities from G/D bands decreases in hydrogenated CNT due to structural disorder as compared with the ratio of the peaks in pristine CNTs.
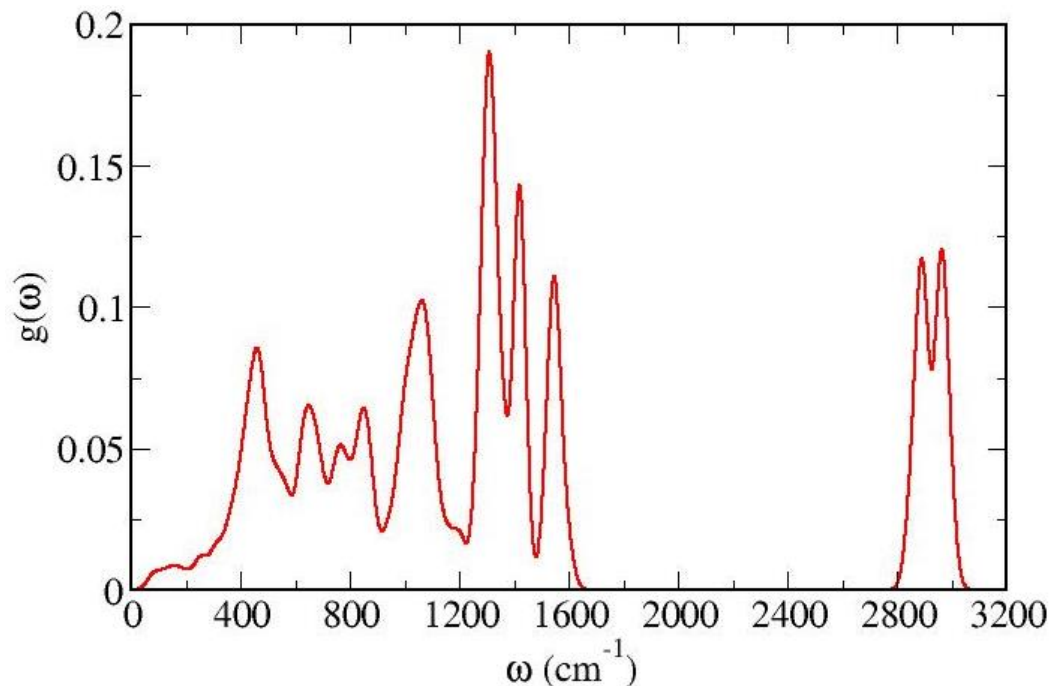
Figure 6-15: Vibrational density of states of hydrogenated CNT using PBE functional.
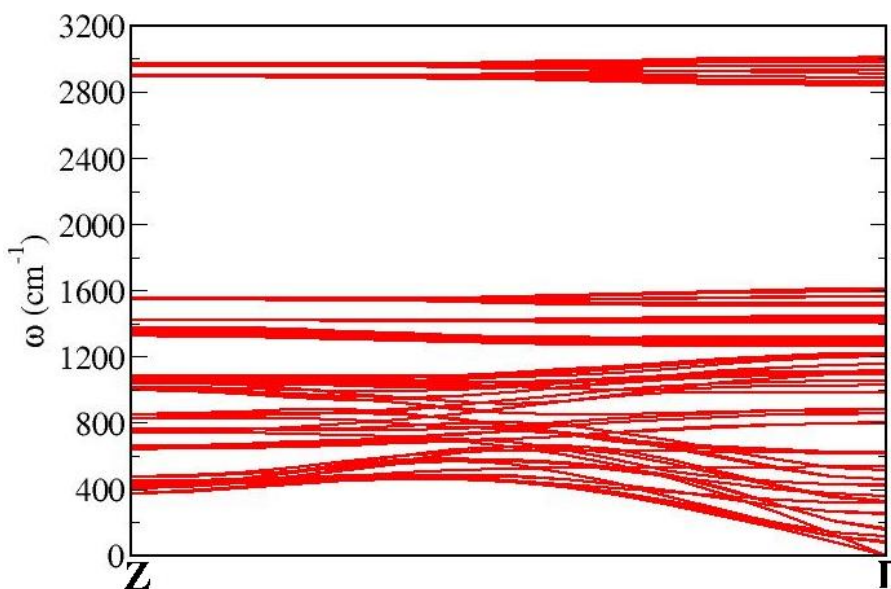
Figure 6-16: Dispersion curve of hydrogenated CNT(4,4)H using PBE functional.

The dispersion curve along z-axis was calculated using the supercell approach shown in Figure 6-16 for the hydrogenated carbon nanotube CNT(4,4)H. A

total of 96 modes of vibration were generated by hydrogenated CNT. Among these, three modes of vibrations were acoustic and the rest modes were Raman and IR active between the frequency regions 73-3006 cm^{-1}. Figure 6-17 represents the modes of vibration for hydrogenated CNT. The low frequency modes between the ranges 73-160 cm^{-1} can be called longitudinal "rocking modes", where the opposing halves of the tube were found to be in anti-phase. The "radial breathing mode" was found near at the value of 381 cm^{-1}. The modes between the ranges from 799-984 cm^{-1} were the "outer planar" modes and modes between the frequencies ranges 1026-1444 cm^{-1} are known as "bending modes" of atoms. The modes between the ranges of frequency from 1562 cm^{-1} to 1610 cm^{-1} are called "tangential" modes of vibration. The flat bands between the frequency regions 2838-3006 cm^{-1} are due to C-H "stretching modes" of vibration in hydrogenated CNT. The arrows in Figure 6-18 show the C-H stretching modes of vibrations. The vibrational density of sates and dispersion curves are drawn for six armchair CNTs and zigzag CNTs (see appendix B.4 and B.5).
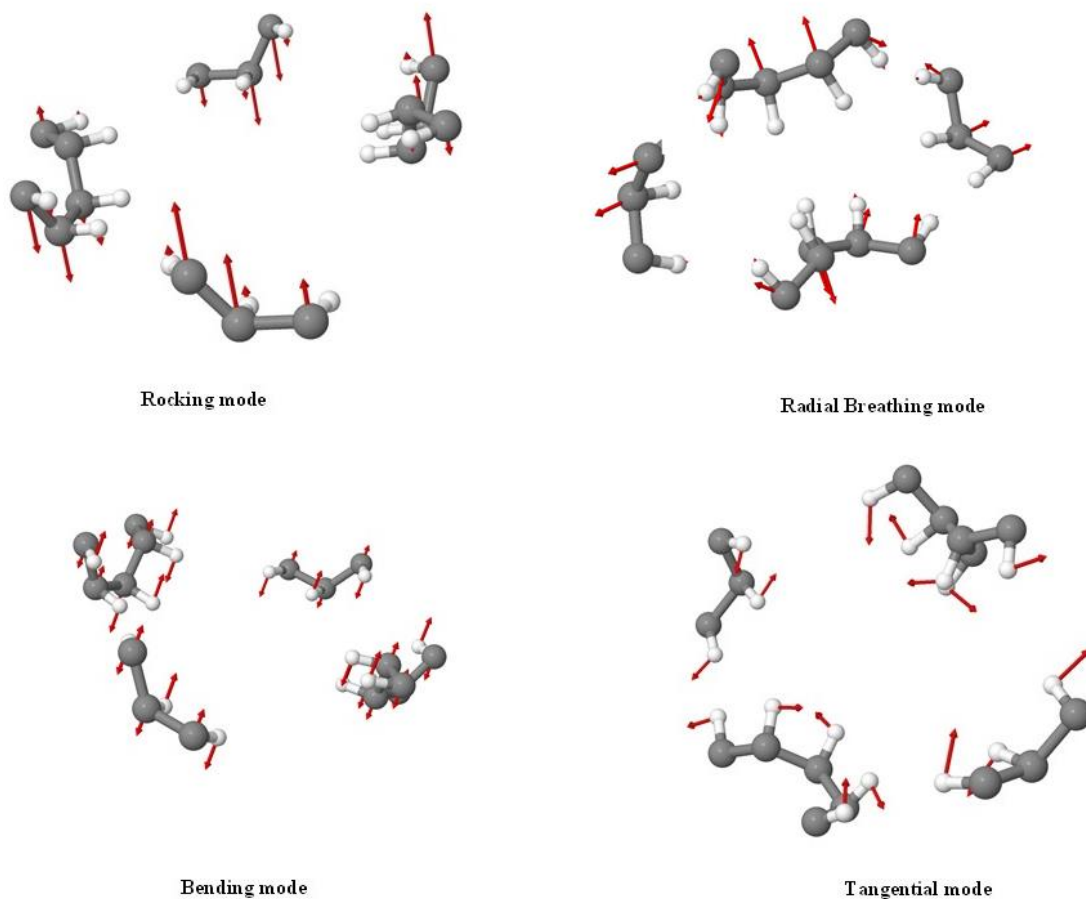
Figure 6-17: Vibrational modes for hydrogenated CNT(4,4).
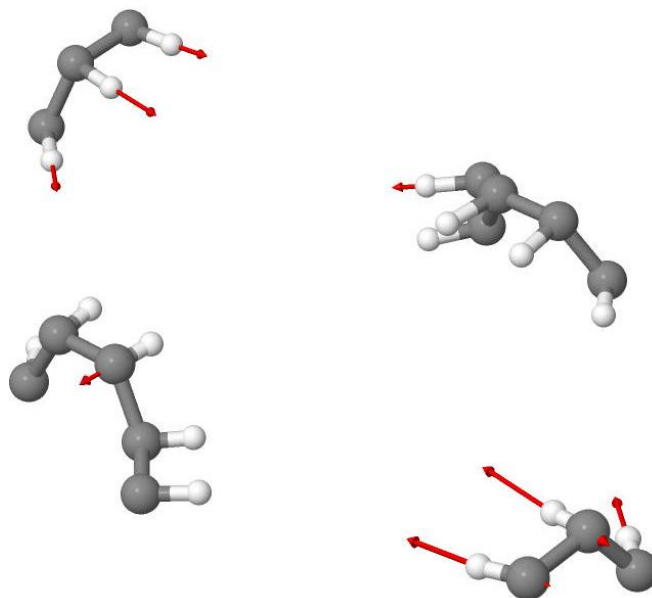
Figure 6-18: Stretching mode of vibration for hydrogenated CNT(4,4).

6.9.   Free Energy Contributions of the Hydrogen Molecule

The translational and rotational free energy of hydrogen in the gaseous phase were performed using statistical thermodynamics (Bowley and Sanchez, 1999) with equations (4.21) and (4.26) respectively. Following the phonon calculation of the optimized hydrogen molecule using finite displacement method, vibrational energy was calculated using the CASTEP (Clark et al., 2005). The hydrogen molecule has only one mode of vibration and its calculated value was 4330 cm^{-1} at value of H-H bond length 0.751 Å. The calculated value of frequency and hydrogen bond was found to be comparable with reported experimental values (ω = 4160 cm^{-1} at H-H = 0.750 Å) given by Stoicheff (1957) as cited in Okamoto et al. (1997). The calculated value of bond length and frequency has an error less than 1% and 4% compared with the available experimental values.
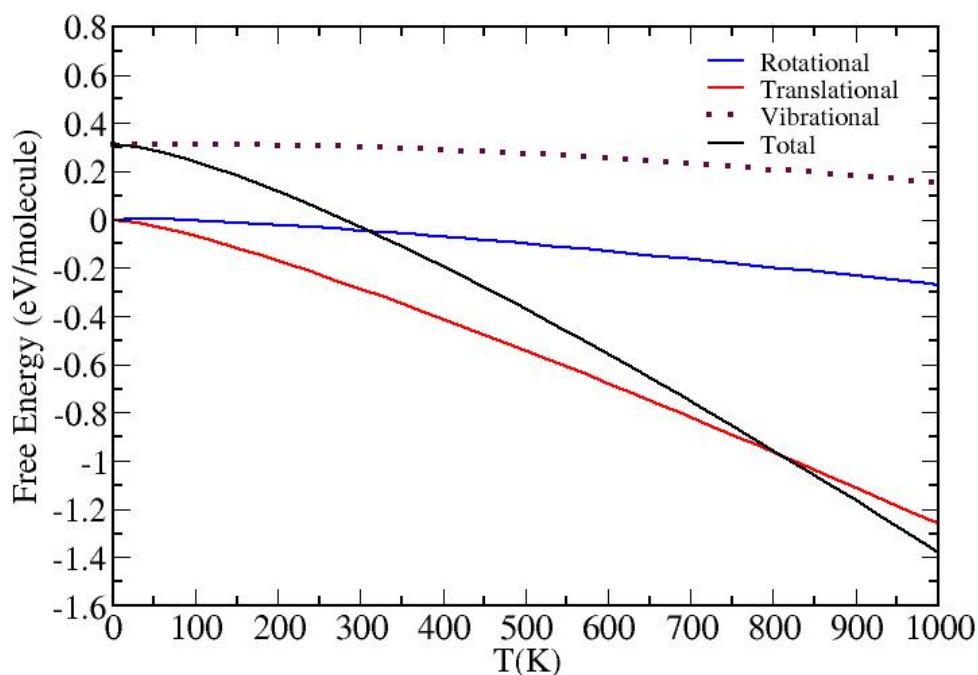
Figure 6-19: Break down contributions of free energies for H$_2$ molecule.

The calculated value of ZPE = 0.3119 eV for the hydrogen molecule is also included in the values of vibrational energy. These calculations were performed at the standard pressure of 1 bar and at this pressure, the Helmholtz free energy can be considered equal to the Gibbs free energy (Moser et al., 2011). The behaviours of translational, rotational and vibrational free energy for the hydrogen molecule is shown in Figure 6-19. In the total free energy, all three contributions (translational,

rotational and vibrational) plus ZPE were included. It can be seen that the contribution of the vibrational free energy is low as compared with rotational and translational energies of the hydrogen molecule in the gaseous phase.

6.10.   Hydrogen Releasing Temperature in Carbon Nanotubes

To calculate the free energy, initial geometries have been generated using the Tube Gen tool (Frey and Doren, 2011) based on the hexagonal unit cell. The single point calculations were carried out for carbon nanotubes to investigate the convergence parameters. The distance between H-H atoms for two adjacent CNTs was calculated in the range of 6-9Å in order to generate isolated hydrogenated CNTs. For CNTs, a constraint was applied to vary the c-axis coordinates only.

The single point calculations were carried out for both systems of the CNTs and hydrogenated CNTs in order to find the lattice parameters. The ultrasoft (Vanderbilt, 1990) on the fly (OTF) pseudopotentials were generated to model the ion-electron interactions with the generalized gradient approximation (GGA) for the exchange and correlation functional in the formalism of Perdew, Burke and Ernzerhof (PBE) (Perdew et al., 1996). The values of cut off energy for all structures were selected so that the total energy should be converged with in 1meV. All the reactants and product should have the same value of cut-off energies in all calculations. The Brillouin Zone was sampled by 1×1×20 Monk-Pack mesh (Monkhorst and Pack, 1976) of k-points. The total energy of systems was converged within 1meV. In Section 6.3, details of convergence tests for CNTs and hydrogenated CNTs have been provided.

All the systems were fully relaxed in order to attain equilibrium until the maximum force on each ion reached the value 0.05 (eV/Å) and the calculated maximum value of the stress was found about 0.01 GPa. Each atom had moved about 10^{-3} Å from the previous step. The relaxed structure of hydrogenated CNT(4,4)H is shown in Figure 6-20 and the C-C bond length has increased to attain an sp^3 hybrid structure.
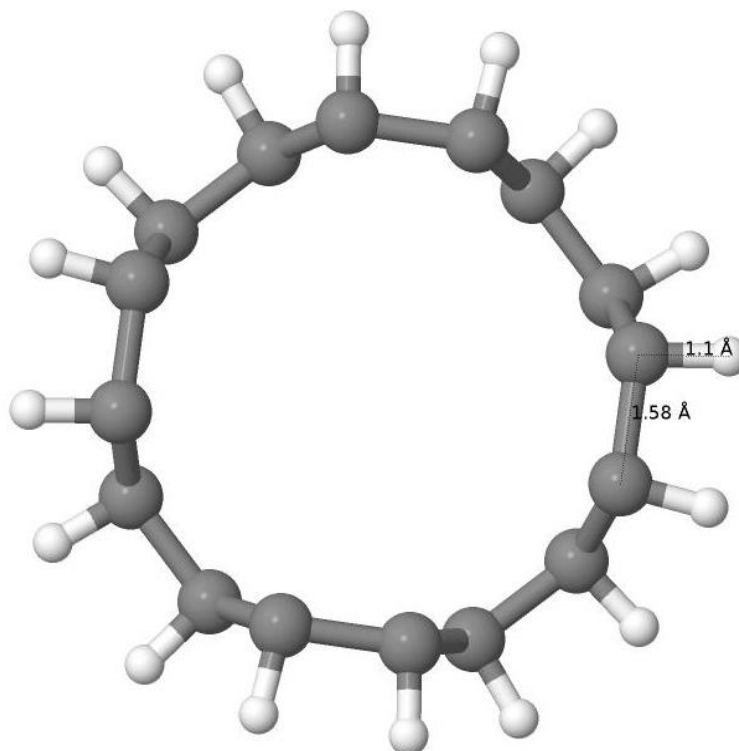
Figure 6-20: Geometry optimized structure of chemisorbed hydrogen with CNT(4.4)H.

The vibrational free energies have been calculated for pristine and hydrogenated carbon nanotubes using CASTEP. The Phonon q-points grid for $1\times1\times25$ was used for dynamical calculations along the tube axis. The transition temperatures of zigzag and arm chair nanotubes were calculated in order to investigate the stability of hydrogenated carbon nanotubes.

In the present study of CNT(4,4) with H_2 and hydrogenated CNT(4,4) ($C_{16}H_{16}$), hydrogen releasing temperature has value 259 K and the calculated value of Gibbs energy was about -0.0158 (eV/atom). The crossing point in Figure 6-21 indicates the hydrogen releasing temperature of CNTs and hydrogenated CNTs. At this temperature, sp^2 to sp^3 conversion takes place due to re-hybridization of the C-C π bond. The Gibbs energy of systems was used to determine the temperature of the release and the effect of pressure on the hydrogen releasing temperatures. The effect of pressure on the Gibbs free energy of CNT(4,4)H was found to be negligible over a pressure range 0 bar to 100 bar in hydrogenated CNT(4,4). However, Figure 6-22

shows that the hydrogen release temperature becomes larger with increase in pressure.
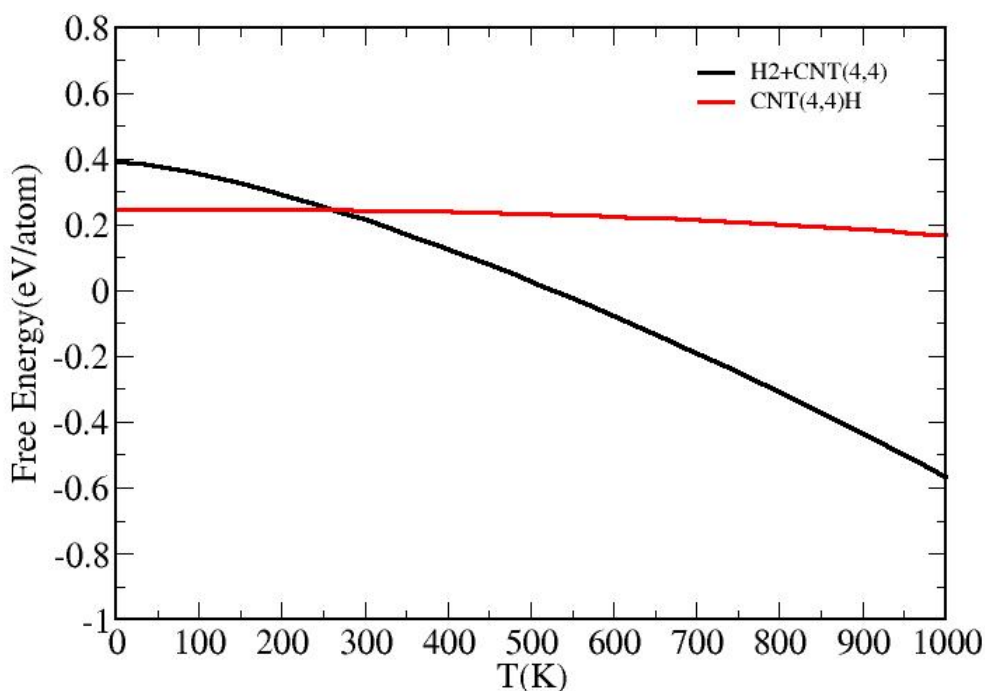
Figure 6-21: Hydrogen releasing temperature for CNT(4,4)H.
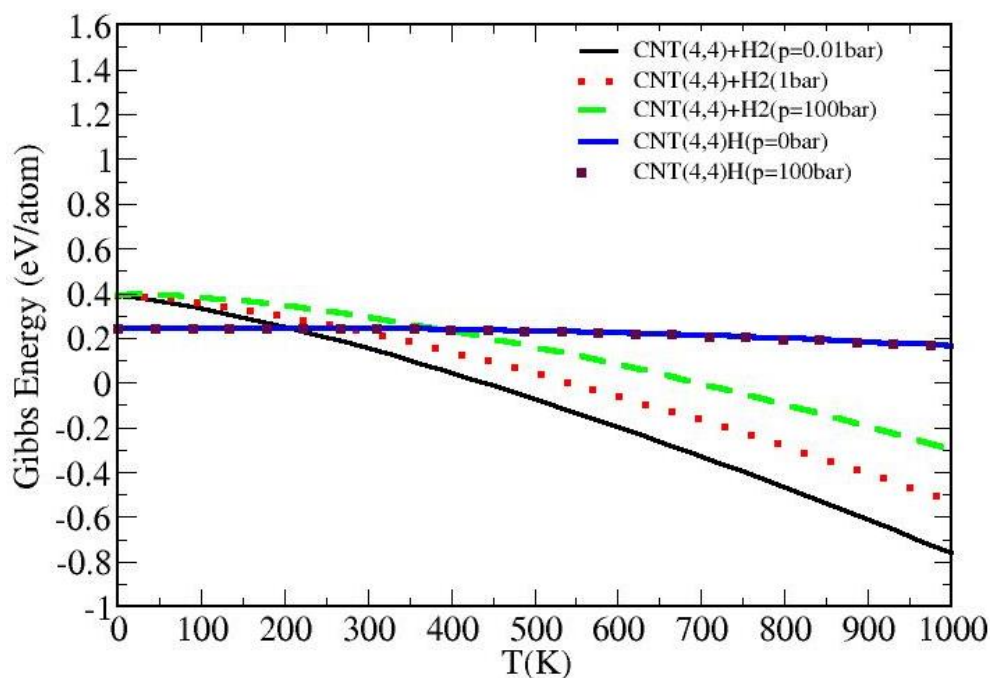
Figure 6-22: Temperature of dissociation at different H_2 pressures. Pressures up to 100 bar have negligible effect on the Gibbs energy of CNT(4,4)H.

After performing the calculation of one hydrogenated CNT, the study of hydrogen release temperatures was extended to six different zigzag and armchair CNTs. Table 6-8 displays the hydrogen release temperatures at p = 1bar for zigzag and armchair CNTs. In order to predict the hydrogen release temperatures, the electronic energy H_2 was included along with zero point energy, translational, rotational and vibrational free energies (See Table 6-7). In our calculations, hydrogen release temperatures decrease with increase in diameters of zigzag CNTs. Surprisingly, calculated values for hydrogen release temperatures rises with increase with diameters for armchair CNTs. The calculated range of temperatures can be significantly compared with Nikitin et al. (2008) 's experimentally determined range (473-573K) for the stable C-H using experimental spectroscopic techniques.

Table 6-8: Hydrogen releasing temperatures for zigzag and arm chair CNTs.

Reactants	Product	Hydrogen Releasing Temperature (K)
CNT(4,0) + 8H_2	$C_{16}H_{16}$	611
CNT(5,0) + 10H_2	$C_{20}H_{20}$	415
CNT(6,0) + 12H_2	$C_{24}H_{24}$	240
CNT(8,0) + 16H_2	$C_{32}H_{32}$	170
CNT(4,4) + 8H_2	$C_{16}H_{16}$	259
CNT(5,5) + 10H_2	$C_{20}H_{20}$	433
CNT(6,6) + 12H_2	$C_{24}H_{24}$	530

Further, it was also mentioned in previous work by Nikitin et al. (2005) that the C-H bond dissociated above the temperature of 873K in a reversible reaction. The current findings were found to be consistent with previous findings of Tokura et al. (2008) in which it was reported that hydrogen atomic adsorption on SWNT has been induced by structural deformation from sp^2 to sp^3 like bonding. This deformation was found to be dependent on diameters of SWCNTs. Talyzin et al. (2011) also reported the temperature 823 K for the formation of C-H bonds in hydrogenated CNT using the etching method. This temperature was matched with

the calculated hydrogen release temperatures using vibrational free energy (see Appendix B.7).
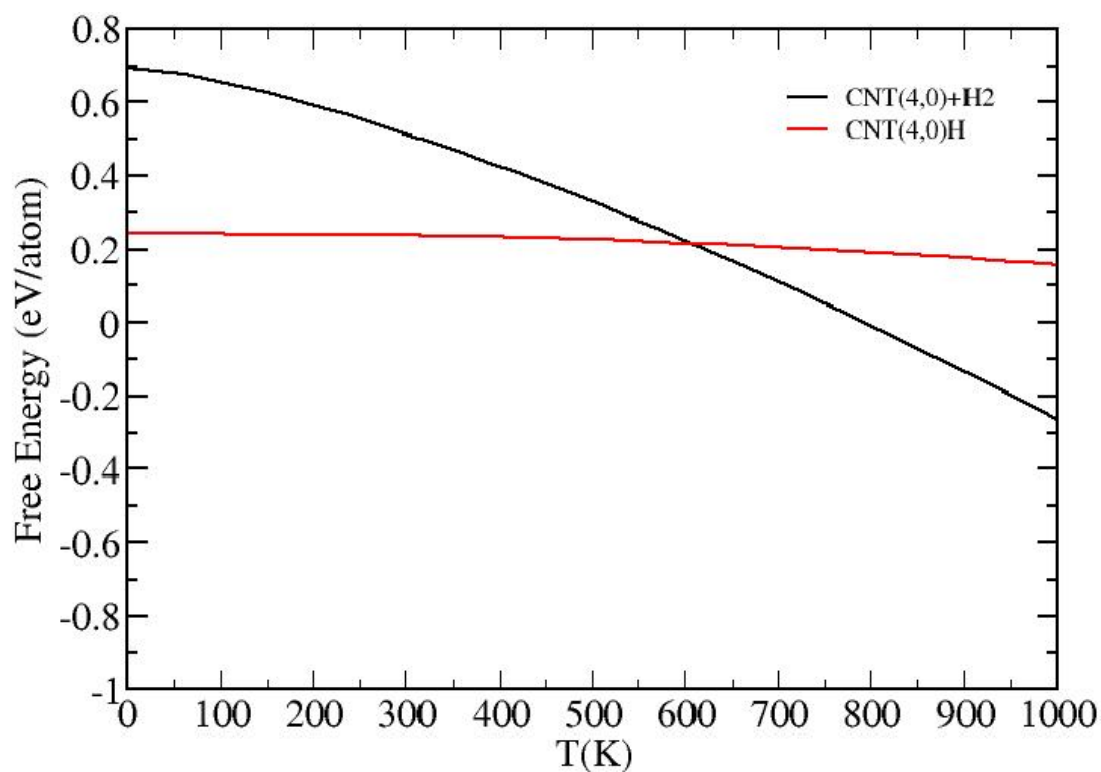
Figure 6-23: Hydrogen releasing temperature for CNT(4,0)H.
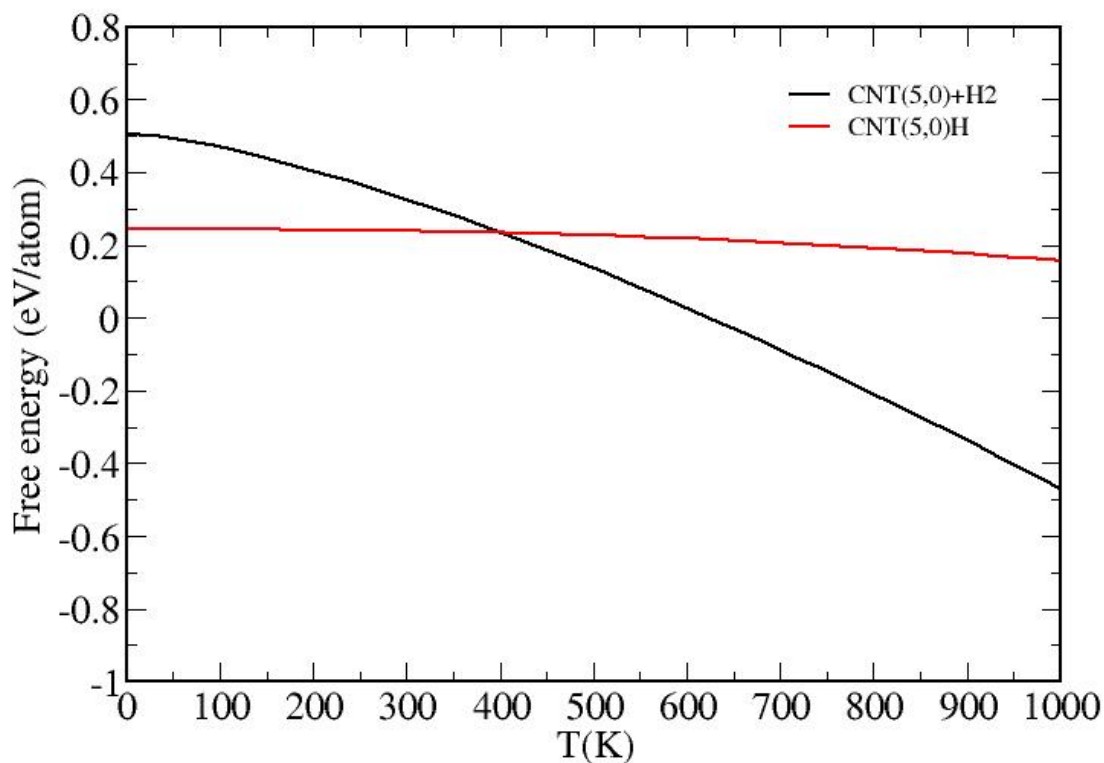
Figure 6-24: Hydrogen releasing temperature for CNT(5,0)H.
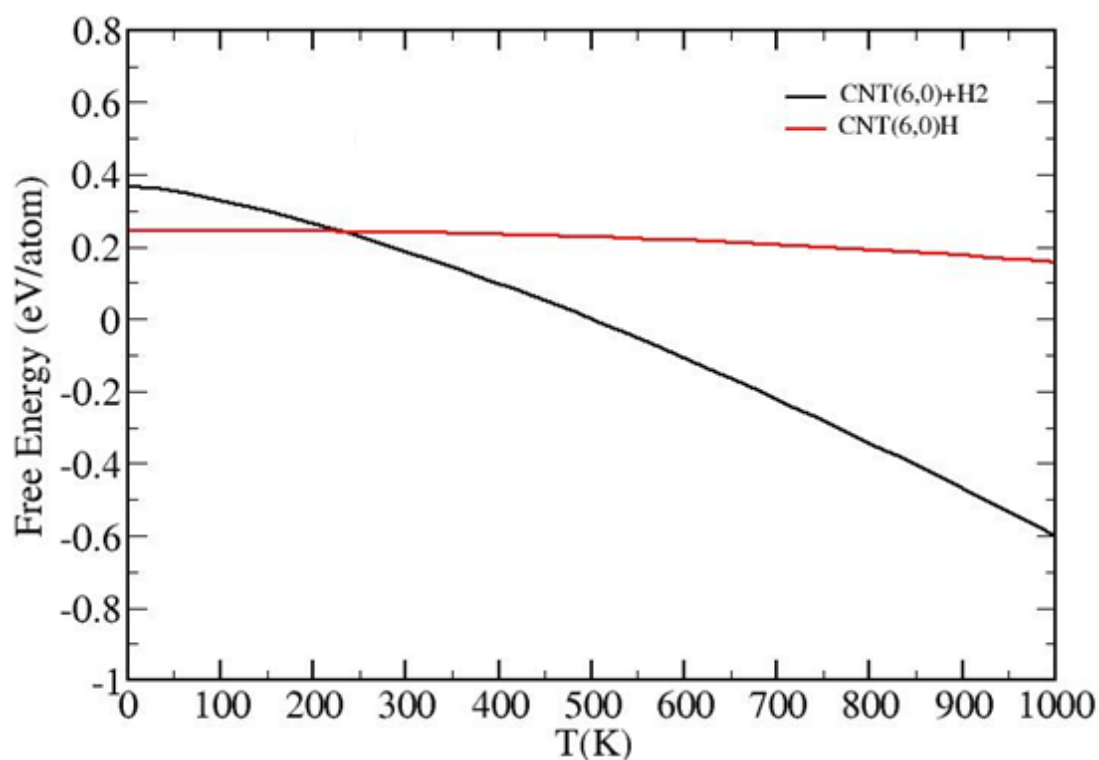
Figure 6-25: Hydrogen releasing temperature for CNT(6,0)H.
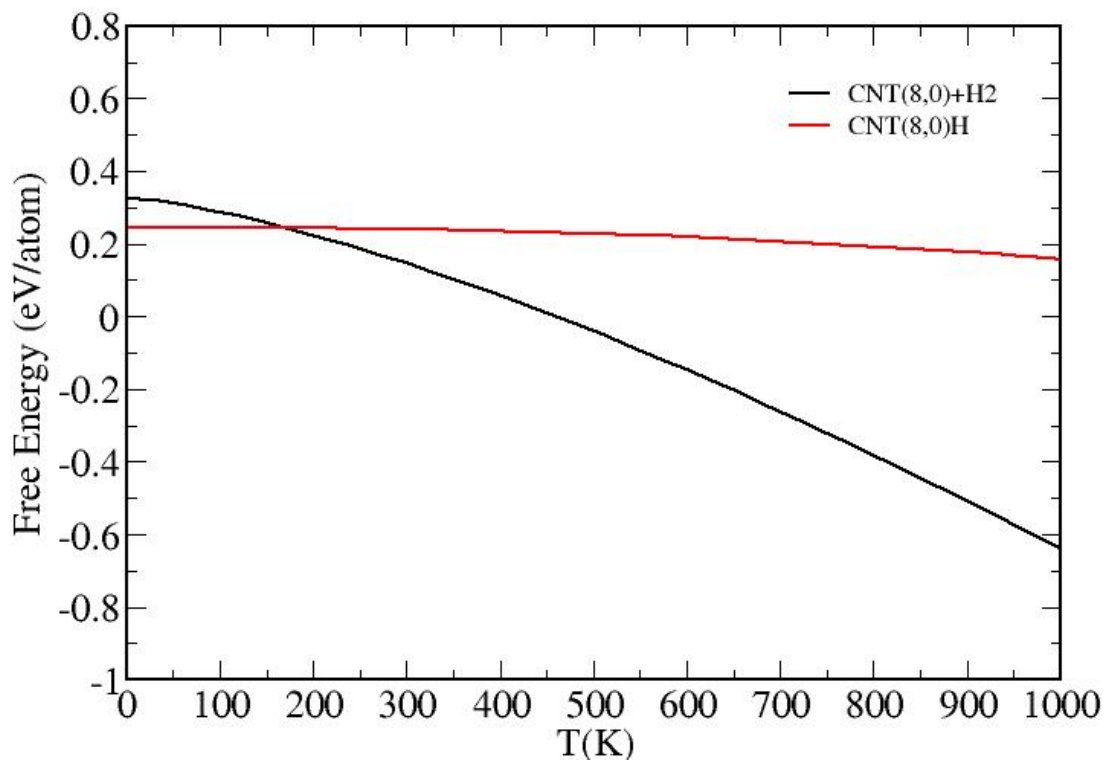
Figure 6-26: Hydrogen releasing temperature for CNT(8,0)H.
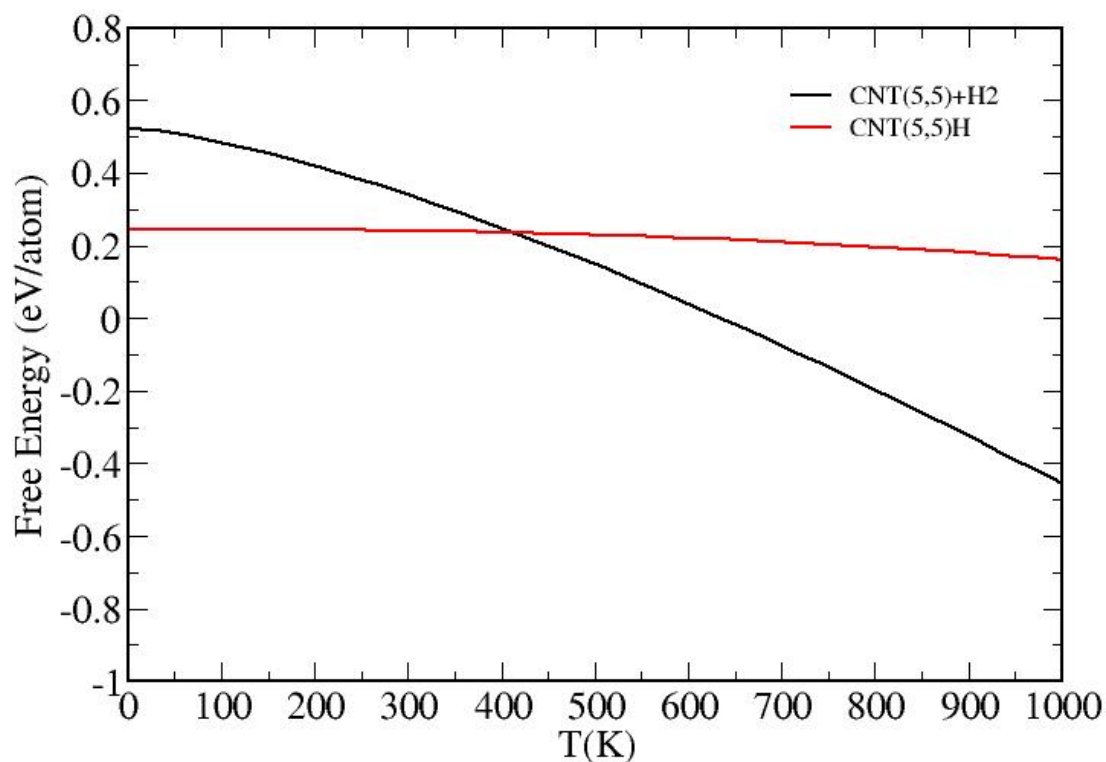
Figure 6-27: Hydrogen releasing temperature for CNT(5,5)H.
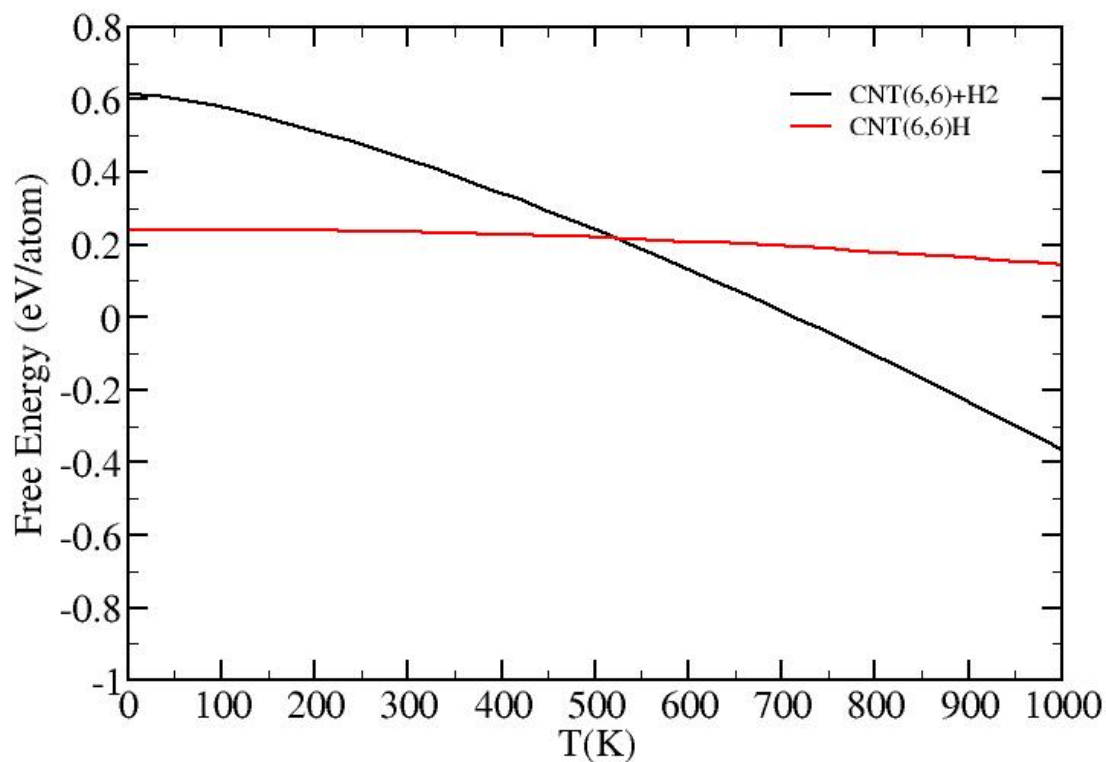
Figure 6-28: Hydrogen releasing temperature for CNT(6,6)H.

6.11.   Summary

The structural properties of CNTs and hydrogenated CNTs have been studied using the GGA-DFT. The binding energies of hydrogen and band gaps have been calculated in exo-hydrogenated CNTs with respect to their diameter. The vibrational density of states in hydrogenated CNTs has been studied to evaluate C-H modes of vibration. The C-H modes of vibrations in different regions of frequency have been studied to get complete vibrational information for the exo-hydrogenated CNTs. The hydrogen molecule free energies have been determined the using statistical physics relations. The free energies have been used to determine the hydrogen release temperature in hydrogenated CNT.

6.12.   Conclusions

The reaction energies of atomic hydrogen with zigzag CNTs were higher than armchair CNTs. Thus, zigzag CNTs were found to be more stable than armchair CNTs. The GGA-PBE functional was found to be successful in the prediction of binding energies in hydrogenated CNT. The reaction of molecular hydrogen with small diameter zigzag CNTs with high curvature were found to be more favourable compared to large diameter zigzag and armchair CNTs. The band gap in zigzag and armchair CNTs was determined to find the stability and it was found that lower diameter zigzag CNTs have larger values of band gap so these were more stable than the armchair CNTs.

As for phonon calculations, the vibrational density of states (VDOS) of hydrogenated CNT has been generated to get the information about the C-H stretching mode of vibration. The contribution of translational and rotational energies was found to be higher than the vibrational energy for the hydrogen molecule. The predicted hydrogen release temperature for zigzag CNTs is found to be decreased with increase in diameters but the opposite trend was noted in arm chair CNTs. Subsequently, from the predicted hydrogen release temperatures, zigzag CNTs can be considered as a better choice for the hydrogen storage.

Chapter 7. Conclusions and Final Remarks

7.1.   Summary

This study set out to determine the static and dynamical properties of graphitic materials. Here, we explored the properties of graphite using dispersion corrected density functional theory and the pseudopotential method. Thermodynamical calculations were used to predict the hydrogen release temperature in hydrogenated arm chair and zigzag CNTs.

Vanderbilt pseudopotentials were used to study the static and dynamic properties of graphitic materials. This type of pseudopotential uses relatively low cut off energies so it is found more efficient. We performed the geometry optimization of graphite to find the lattice constants and bond length. In the graphite system, we especially used the dispersion corrected scheme to get the accurate structural parameters for the hexagonal and rhombohedral graphite. Moreover, the band gap and semi metallic behaviour of graphite was determined using the new PBE+TS functional.

The vibrational properties of graphite were investigated using the finite displacement method. The supercell method was used to extend the vibrational studies by including the interaction of large the number of atoms. The dispersion corrected functions were used to carry out the vibrational studies in graphite. In the present study, special attention has been made to investigate the dispersion curves of the graphite system by including the accurate dispersion effects at low frequency. Our calculated lower modes vibration for graphite system has an excellent agreement with available experimental data. Although significant research has been performed on graphite, the low frequency modes of interaction have not been extensively considered by previous ab initio methods. In the present study, the dispersion corrected TS scheme was found to be more efficient and reliable for the graphite system. The k-dependent phonon frequencies were determined and the

Brillouin Zone integrated density of states was also evaluated. A dynamical study of rhombohedral graphite was also performed using the dispersion corrected TS scheme. The important modes were analysed by evaluating the dispersion curve in the important region of the Brillouin zone.

The reaction energies of gaseous hydrogen in atomic and molecular form in armchair and zigzag hydrogenated CNTs were calculated using the PBE-GGA functional. The zigzag CNTs were found to be more stable than arm chair CNTs. The band gap of hydrogenated zigzag and arm chair CNTs were determined to find the stability. The band gaps have high values in low diameter hydrogenated zigzag CNTs, which, therefore, showed higher stability. Also, vibrational density of states have been studied for the hydrogenated CNT(4,4) to evaluate the C-H stretching mode of vibration using the GGA-PBE functional.

Following the geometry optimization and phonon calculations, the free energy of CNTs and hydrogenated carbon nanotubes has been calculated using the PBE-GGA functional. The partition functions of statistical thermodynamics have been used to find rotational and translational energies of the hydrogen molecule. The vibrational energies and electronic energies of hydrogenated CNTs were found using CASTEP. These calculations have been performed in order to predict the hydrogen release temperature in both zigzag and armchair CNTs. The calculated values of hydrogen release temperatures are needed to determine the stability of the C-H bond in hydrogenated arm chair and zigzag CNTs. These calculations predict that low diameter hydrogenated zigzags CNTs are more favourable and better for hydrogen storage.

7.2.   Sources of Errors in Our Model

Although many efforts have been made to reduce the errors in our calculations, we cannot get rid of all possible errors. Here we present the most probable sources of error that may affect the accuracy of calculation. Pseudopotential selection is always vital as it influences the structural parameters of materials. Although we have improved the structural parameters by including accurate VdW interactions in graphite, there may be some inherent sources of error. The GGA-functional also overestimates the bond length so it can also be a cause of error. The

main concern is the adequacy of the GGA functional in accurately modelling hydrogen bonds in a complex system such as CNTs with hydrogen. The discrete FFT grid may have of rounding errors and interpolation errors, since the total energy is not conserved under a shift of the entire crystal. Total energy calculations have errors through the use of a finite basis set and a finite k-point set. We choose different k-points sampling for the graphite and CNTs. This difference in k-points sampling is due to three dimensional graphite and one dimensional CNTs systems.

Another major source of error is due to anharmonic effects, since we are using finite displacement in calculating the forces. The degree of anharmonicity is strongly dependent on structure. In using a large supercell, noise in force calculations may become a serious error which can reduce the accuracy of phonon calculations. As we have been using the TS and G06 dispersion correction schemes, the wrong choice of steepness of damping function and scaling factor may lead to some inaccuracies.

7.3.   Future Work

The present study has thrown many questions in need of further investigation in the area of structural and dynamical properties of graphitic materials. The dynamical properties of graphite can be helpful in the calculation of heat conductivity and thermal transport phenomena. Low frequency modes play a significant role in explanation of thermal conductivity.

Experimental studies are currently limited in examining various regions of the dispersion curve in graphite. The high frequency region still needs to be explored in detail for all regions of the dispersion curves with the experimental tools so that our ab initio results could be matched with experimental results. For the CNTs, the experimental determination of phonon dispersion throughout the entire Brillouin zone would require a mono crystalline sample; this study is still unavailable so far.

In the present study, a finite displacement method has been used to investigate the dynamical properties of Graphitic materials. Another interesting way of calculating the dynamical properties is that of Linear Response Theory. In this method, force constant matrix is calculated in the harmonic approximation and the

perturbative description can be applied beyond the harmonic approximation (Baroni et al., 2001). Moreover, for a single k, the calculation of phonon frequencies can be better since there is no requirement to have a supercell. There might be some issues of convergence with linear response theory, in that the force constant matrix depends on the second derivative, thus more accurate convergence of the wave functions is needed for the finite difference approach than has been used in present study, where the dependence was only the first derivatives. Thus, it may be not suitable for large systems.

It is suggested that the association of nano particles (catalysts) with graphene and CNTs as hydrogen storage can be investigated in future studies. The transition metals and nano particles can be used as a catalyst to enhance the storage of the hydrogen in graphitic materials. The binding energy of hydrogen molecules in transition metal doped graphitic materials can be studied through a physisorption process using the density function theory.

Another interesting study might be high pressure hydrogenated CNTs, as in the present study we are limited up to 100 bar. At high pressure, a vibrational study of hydrogenated CNTs can bring interesting information about the modes of vibration. In this thesis, we mainly focus on the CNTs as hydrogen storage. This study can be extended to include graphene and graphane.

Very few experimental studies of hydrogenated CNTs have been performed to find the hydrogen release temperature to determine the stability of C-H bond. But still further experimental efforts are required to know the accurate range of hydrogen release temperatures. Therefore, the present study of the hydrogen releasing temperature is beneficial for the choice of CNTs as hydrogen storage materials and as a guide to further experiments.

Boron nitride (BN) and molybdenum disulphide (MoS_2) have a similar hexagonal structure to the graphitic materials. The ab initio supercell approach can be used to explore the structural, dynamical and thermodynamical properties of these materials. These materials may be used as hydrogen storage materials in the future.

Currently, researchers are exploring graphitic materials in detail using high performance computing but still it needs more efforts to create novel hydrogenated graphitic materials for further in depth study. The complete understanding of these materials is still a significant challenge for theoretical and experimental researchers.

References

Ackland, G. J., Warren, M. C. and Clark, S. J. 1997. Practical methods in ab initio lattice dynamics. *Journal of Physics:Condensed Matter,* 9(37)**,** 7861-7872.

Admaska, L., Lin, Y., Ross, A. J., Batziill, M. and Oleynik, I. I. 2012. Atomic and electronic structure of simple metal/graphene and complex metal/graphene/metal interfaces. *Physical Review B,* 85(19)**,** 1-8.

Alzahrani, A. Z. and Srivistava, G. P. 2009. Graphene to graphite: electronic changes within DFT calculations. *Brazilian Journal of Physics,* 39(04)**,** 694-698.

Andreoni, M., Curioni, A., Kroes, J. M. H., Pietrucci, F. and Greoning, O. 2012. Exohedral Hydrogen Chemisorption on a Carbon Nanotube:The Clustering Effect. *The Journal Of Physical Chemistry C,* 116(1)**,** 268-275.

Ashcroft, N. W. and Mermin, N.D. (eds.) 1976. *Solid State Physics*: Saunders College

Barno, S., Giannozzi, P. and Testa, A. 1987. Green's-function approach to linear response in solids. *Physical Review Letters* 58(18)**,** 1861–1864.

Baroni, S., Girononcli, S. D., Corso, A. D. and Giannozzi, P. 2001. Phonons and related crystal properties from density-functional perturbation theory. *Reviews of Modern Physics,* 73(2)**,** 515-562.

Bazhenov, A. V., Fursova, T. N., Bashkin, I. O., Antonov, V. E., Kondrat'eva, I. V., Krestinin, A. V. and M. Shul'ga, Y. 2006. Electronic and Vibration Spectra of Hydrogenated Carbon Single-Wall Nanotubes. *Fullerenes, Nanotubes, and Carbon Nanostructures,* 14(2-3)**,** 165-170.

Bhowmick, R., Rajasekaran, S., Friebe, D., Beasley, C., Jiao, L., Ogasawara, H., Dai, H., Clemens, B. and Nilsson, A. 2009. Hydrogen Spillover in Pt-Single Walled Carbon Nanotube Composites: Formation of Stable C-H Bonds. *Journal of American Chemical Society,* 133(14)**,** 5580-5586.

Bloch, F. 1928. *Zeitschrift fur Physik,* 52.

Born, M. and Oppenheimer, R. 1927. *Anal der Physik,* 84**,** 457–484.

Bowley, R. and Sanchez, M. (eds.) 1999. *Introductory Satistical Mechanics,* Oxford: Calendon Press.

Broyden, C. G. 1970. The Convergence of a Class of Double-rank Minimization Algorithms. *IMA Journal of Applied Mathematics,* 6**,** 76-90.

Buchs, G. 2008. *Local Modification and Characterization of the Electronic Structureof Carbon Nanotubes.* PHD, University of Basel ,Switzerland.

Car, R. and Parrinello, M. 1985. Unified Approach for Molecular Dynamics and Density-Functional Theory. *Physical Review Letters,* 55(22)**,** 2471-2474.

Ceperley, D. M. and Alder, B. J. 1980. Ground State of the Electron Gas by a Stochastic Method. *Physical Review Letters,* 45(7)**,** 566-569.

Chambers, A., Park, C., Bekker, R. T. K. and Rodriguez, N. M. 1998. Hydrogen Storage in Graphite Nanofibers. *The Journal Of Physical Chemistry B,* 102(22)**,** 4253-4256.

Chou, M. Y. 1992. Reformulation of generalized separable pseudopotentials. *Physical Review B,* 45(20)**,** 11465-11468.

Clark, S. J., Segall, M. D., Pickard, C. J., Hasnip, P. J., Probert, M. J., Refson, K. and Payne, M. C. 2005. First principles methods using CASTEP. *Zeitschrift fuer Kristallographie,* 220(5-6)**,** 567-570.

Cote, A. S. 2004. *AB Initio Studies on the Structure and Dynamics of H2O Ice.* PhD, University of Salford,UK.

Dillon, A. C., Jones, K. M., Bekkedahl, T. A., Kiang, C. H., Bethune, D. S. and Heben, M. J. 1997. Storage of hydrogen in single-walled carbon nanotubes. *Nature,* 386(6623)**,** 377-379.

Dirac, P. A. M. 1930. Note on Exchange Phenomena in theThomas Atom. *Mathematical Proceedings of the Cambridge Philosophical Society,* 26(03)**,** 376-385.

Dubay, O. and Kresse, G. 2003. Accurate density functional calculations for the phonon dispersion relations of graphite layer and carbon nanotubes. *Physical Reiew B,* 67(3)**,** 1-13.

Dunlap, B. I. and Boettgar, J. C. 1996. Local-density-functional study of the fullerenes, graphene and graphite. *Journal of Physics B:Atomic ,Molecular and Optical,* 29(21)**,** 4907-4913.

Eaton, P. E. and Cole, T. W. 1964. The Cubane System. *Journal of American Chemical Society,* 86(15)**,** 962-964.

Falkovsky, L. A. 2008. Symmetry constraints on phonon dispersion in graphene. *Physics Letters A,* 372(31)**,** 5189–5192.

Fermi, E. 1928. *Zeitschrift fur Physik,* 48(1-2)**,** 73-79.

Fletcher, R. and Reeves, C. M. 1964. Function minimization by conjugate gradients. *The Computer Journal,* 7(2)**,** 149-154.

Fock, V. 1930. *Zeitschrift fur Physik,* 61.

Frank, W., Elsässer, C. and Fähnle, M. 1995. Ab initio Force-Constant Method for Phonon Dispersions in Alkali Metals. *Physical Review Letters,* 74(10)**,** 1791-1794.

Frey, J. T. and Doren, D. J. 2011. TubeGen3.4 (web-interface, http://turin.nss.udel.edu/research/tubegenonline.html). Newark: University of Delware.

Fuchs, M. and Scheffler, M. 1999. Ab initio pseudopotentials for electronic structure calculations of poly-atomic systems using density-functional theory. *Computer Physics Communications* 119(1)**,** 67-98.

Geim, A. K. and Novoselov, K. S. 2007. The rise of graphene. *Nature Materials,* 06(3)**,** 183-191.

Goedecker, S. and Maschke, K. 1992. Transferability of pseudopotentials. *Physical Review A,* 45(01)**,** 88-93.

Gonze, X. 1997. First-principles responses of solids to atomic displacements and homogeneous electric fields: Implementation of a conjugate-gradient algorithm. *Physical Review B,* 55(16)**,** 10337–10354.

Grimme, S. 2006. Semiempirical GGA-Type Density Functional Constructed with a Long-Range Dispersion Correction. *Journal of Computational Chemistry,* 27(15)**,** 1787-1799.

Hamann, D. R., Schulter, M. and Chiang.C 1979. Norm-Conserving Pseudopotentials. *Physical Review Letters,* 43(20)**,** 1494–1497.

Hanfland, M., Beister, H. and Syassen, K. 1989. Graphite under pressure: Equation of state and first-order Raman modes. *Physical Review B,* 39(17)**,** 12598-12603.

Hartree, D. R. 1928. The Wave Mechanics of an Atom with a non-Coulomb Central Field. Part III. Term Values and Intensities in Series in Optical Spectra. *Proc.Cambridge Philosphical Society* 24(03)**,** 426-437.

Hohenberg, P. and Kohn, W. 1964. Inhomogeneous Electron Gas. *Physical Review B,* 136(3B)**,** B864–B871.

Iijima, S. 1991. Helical microtubules of graphitic carbon. *Nature,* 354**,** 56-58.

Jaun, Y. M. and Kaxiras, E. 1993. Application of gradient corrections to density-functional theory for atoms and solids. *Physical Review B,* 48 (20)**,** 14944-14952.

Jena, P. 2011. Materials for Hydrogen Storage: Past, Present, and Future. *The Journal Of Physical Chemistry Letters,* 02(03)**,** 206-209.

Kaxiras, E. 2003. Atomic and Electronic Structure of Solids. Cambrridge University Press,UK.

Khare, B. N., Meyyappan, M., Cassell, A. M., Nguyen, C. V. and Han, J. 2002. Functionalization of Carbon Nanotubes Using Atomic Hydrogen from a Glow Discharge. *Nano Letters,* 2(1)**,** 73-77.

Kleinman, L. and Bylander, D. M. 1982. Efficacious Form for Model Pseudopotentials. *Physical Review Letters,* 48(20)**,** 1425–1428.

Kohn, W. and Sham, L. J. 1965. Self-Consistent Equations Including Exchange and Correlation Effects. *Physical Review* 140(4A)**,** 1133–1138.

Kresse, G. and Furthmu¨Ller, J. 1996. Efficient iterative schemes for ab initio total-energy calculations using a plane-wave basis set. *Physical Review B,* 54(16)**,** 11169-11186.

Kresse, G., Furthmur, J. and Hafner, J. 1995. Ab initio Force Constant Approach to Phonon Dispersion Relations of Diamond and Graphite. *Euro Physics Letters,* 32(9)**,** 729-734.

Kresse, G. and Hafner, J. 1994. Norm-conserving and ultrasoft pseudopotentials for first-row and transition elements. *J.Condensed Matter Physics,* 6(40)**,** 8245-8257.

Kroto, H. W., Heath, J. R., O'brien, S. C., Curl, R. F. and Smalley, R. E. 1985. C60: Buckminsterfullerene. *Letters to Nature,* 318(6042)**,** 162 - 163

Lazzeri, M., Attaccalite, C., Wirtz, L. and Mauri, F. 2008. Impact of the electron-electron correlation on phonon dispersion: Failure of LDA and GGA DFT functionals in graphene and graphite. *Physical Review B,* 78(8)**,** 081406.

Li, J., Furuta, T., Goto, H., Ohashi, T., Fujiwara, Y. and Yip, S. 2003. Theoretical evaluation of hydrogen storage capacity in pure carbon nanostructures. *Journal Of Chemical Physics,* 119(4)**,** 2376-2385.

Lipson, H. and Stokes, A. R. 1942. The Structure of Graphite. *Proceedings of the Royal Society of London, Series A: Mathematical and Physical Sciences* 181(984)**,** 101-105.

London, F. 1930. On the theory and classification of molecular forces. *Zeitschrift fur Physik,* 63.

Maslov, M. M., Lobanov, D. A., Podlivaev, A. I. and Openov.L.A. 2009. Thermal stability of cubane C8H8. *The Physics of Solid State,* 51(03)**,** 645-648.

Mcnellis, E., Meyer, J. and Reute, K. 2009. Azobenzene at coinage metal surfaces: Role of dispersive van der Waals interactions. *Physical Review B,* 80(20)**,** 1-10.

Meletov, K. P., Maksimov, A. A., Tartakovskii, I. I., Bashkin, I. O., Shestakov, V. V., Krestinin, A. V., Shulga.Yu.M., Andrikopoulos.K.S., Christofilos, D. and Kourouklis, G. A. 2007. Raman study of the high-pressure hydrogenated single-wall carbon nanotubes: In search of chemically bonded and adsorbed molecular hydrogen. *Chemical Physics Letters,* 433(04-06)**,** 335–339.

Mohr, M., Maultzsh, J., Dobardzic, E., .Milosevic, I., Damnjanovic, M., Bosak, A., Krisch, M. and Thomsen, C. 2007. Phonon dispersion of graphite by inelastic x-ray scattering. *Physical Review B,* 76**,** 1-7.

Monkhorst, H. J. and Pack, J. D. 1976. Special points for Brillouin-zone integrations. *Physical Review B,* 13(12)**,** 5188-5192.

Morrison, I., Bylander, D. M. and Kleinman, L. 1993. Nonlocal Hermitian norm-conserving Vanderbilt pseudopotential. *Physical Review B,* 47(11)**,** 6728-6731.

Moser, D., Baldissin, G., Bull, D. J., Riley, D. J., Morrison, I., Ross, D. K., Oates, W. A. and Noreus, D. 2011. The Pressure-temperature phase diagram of MgH2 and isotopic substitution. *Journal of Physiics:Condensed Matter,* 23(30)**,** 1-9.

Mounet, N. and Marzari , N. 2005. First-principles determination of the structural, vibrational and thermodynamic properties of diamond, graphite, and derivatives. *Physical Review B,* 71(20)**,** 1-14.

Nicklow, R., Wakabayashi, N. and Smith, H. G. 1972. Lattice Dynamics of Pyrolytic Graphite. *Physical Review B,* 5(12)**,** 4951-4962.

Nika , D. L. and Balandin, A. A. 2012. Two-dimensional phonon transport in graphene. *Journal of Physics: Condensed Matter,* 24**,** 1-18.

Nikitin, A., Li, X., Zhong, Z., Ogasawara, H., Dai, H. and Nilsson, A. 2008. Hydrogen Storage in Carbon Nanotubes through the Formation of Stable C-H Bonds. *Nano Letters,* 8(1)**,** 162-167.

Nikitin, A., Ogasawara, H., Mann, D., Denecke, R., Zhang, Z., Dai, H., Cho, K. and Nilsson, A. 2005. Hydrogenation of Single-Walled Carbon Nanotubes. *Physical Review Letters,* 95(22)**,** 225507.

Novoselov, K. S., Geim, A. K., Morzov, S. V., Jiang, D., Katsnelson, M., Grigorieva, I. V., Dubonos, S. V. and Frisov, A. A. 2005. Two-dimensional gas of massless Dirac fermions in graphene. *Nature,* 438(7065)**,** 197-200.

Okamoto, Y., Saito, R. and Oshiyama, A. 1997. Comparative study of vibrational frequencies of H2 molecules in Si and GaAs. *Physical Review B,* 56(16)**,** R10 016-R10 019.

Ortmann, F., Schmidt, W. G. and Bechstedt, F. 2005. Attracted by Long-Range Electron Correlation:Adenine on Graphite. *Physical Review Letters,* 95(18)**,** 186101.

Parr, G. R. and Yang, W. 1989. Denisty-Functional Theory of Atoms and Molecules. Oxford: Oxford Unversity Press.

Partoens, B., Peeters, F. M. and 2006. From graphene to graphite: Electronic structure around the K point. *Physical Review B,* 74**,** 1-11.

Paulatto, L., Mauri, F. and Lazzeri, M. 2013. Anharmonic properties from a generalized third-order ab initio approach:Theory and applications to graphite and graphene. *Physical Riew B,* 87(21)**,** 214303.

Pauli, W. 1925. *Zeitschrift fur Physik,* 31**,** 765-783.

Perdew, J. P., Burke, K. and Ernzerhof, M. 1996. Generalized Gradient Approximation Made Simple. *Physical Review Letters* 77(18)**,** 3865-3868.

Perdew, J. P. and Yue, W. 1986. Accurate and simple density functional for the electronic exchange energy: Generalized gradient approximation. *Physical Review B* 33(12)**,** 8800–8802.

Perebeinos, V. and Tersoff, J. 2009. Valence force model for phonons in graphene and carbon nanotubes. *physical Review B,* 79(24)**,** 1-4.

Piscanec, S., Lazzari, M., Mauri, F. and Ferrari, A. C. 2007. Optical phonon of graphene and nanotube. *The European Physical Journal Special Topics,* 148(1)**,** 159-170.

Reich, S. and Thomsen, C. 2009. Raman spectroscopy of graphite. *Philosphical Transactions of Royal Society A London,* 362(1824)**,** 2271-2288.

Roberston, I. J. and Payne, M. D. 1991. The k.p method in pseudopotential total energy calculations: error reduction and absolut energies. *Journal of Physics:Condensed Matter,* 3(45).

Ross, D. K. 1973. Inelastic neutron scattering from polycrystalline graphite at temperatures up to 1920°C. *Journal of Physics C,* 6(24)**,** 3525-3535.

Schimmel, H. G., Kearley, G. J., Nijkamp, M. G., Visser, C. T., De Jong, K. P. and Mulder, F. M. 2003. Hydrogen Adsorption in Carbon Nanostructures:

Comparison of Nanotubes, Fibers, and Coals. *Chemistry - A European Journal* 9(19)**,** 4764-4770.

Scholl, D. S. and Steckel, J. A. 2009. Density Functional Theory *A Practical Introduction* A John Wiley & Sons

Segall, M. D., Lindan, P. J. D., Probert, M. J., Pickard, C. J., Hasnip, P. J., Clark, S. J. and Payne, M. C. 2002. First-principles simulation: ideas, illustrations and the CASTEP code. *Journal of Physics: Condensed Matter,* 14(11)**,** 2717-2744.

Setyawan, Wahyu, Curtarolo and Stefano 2010. High-throughput electronic band structure calculations: Challenges and tools. *Computational Material Science,* 49(2)**,** 299-312.

Slater, J. C. 1930. Cohesion in Monovalent Metals. *Physical Review,* 35(5)**,** 509-529.

Stoicheff, B. P. 1957. High Resolution Raman Spectroscopy of Gases: IX. Spectra of H2, HD, and D2. *Canadian Journal of Physics,* 35(06)**,** 730-741.

Stojkovic, D., Zhang, P., Lammert, P. E. and Crespi, V. H. 2003. Collective stabilization of hydrogen chemisorption on graphenic surfaces. *Physical Review B,* 68(19)**,** 1-4.

Sutton, A. P. (ed.) 1996. *Electronic Structure of Materials,* Oxford: Clarendon Press.

Talyzin, V. A., Luzan, S., Anoshkin, V. I., Nasibulin, G. A., Jiang, H., Kauppinen, I. E., Mikoushkin, M. V., Shintov, V. V., Marchenkov, A. N. and Noreus, D. 2011. Hydrogenation, Purification, and Unzipping of Carbon Nanotubes by Reaction with Molecular Hydrogen:Road to Graphane Nanoribbons. *American Chemical Society Nano,* 05(06)**,** 5132-5140.

Tans, S. J., Devoret, M. H., Dai, H., Thess, A., Smalley, R. E., Geerlings, L. J. and Dekker, C. 1997. Individual single-wall carbon nanotubes as quantum wires *Letters to Nature,* 386**,** 474 - 477.

Taylor, P. R. and Heinonen, P. L. (eds.) 2002. *A Quantum Approach to Condensed Matter Physics*: Cambridge University Press.

Tewary, V. K. and Yang, B. 2009. Parametric interatomic potential for graphene. *Physical Review B* 79(7)**,** 1-9.

Thomas, T. H. 1926. The calculation of Atomic Fields. *Proc.Cambridge Philosphical Society,* 23(05)**,** 542-548.

Tkatchenko, A. and Scheffler, M. 2009. Accurate Molecular Van DerWaals Interactions from Ground-State Electron Density and Free-Atom Reference Data. *Physical Review Letters,* 102(7)**,** 1-4.

Tokura, A., Maeda, M., Teraoka, Y., Yoshigoe, A., Takagi, D., Homma, Y., Watanabe, Y. and Kobayashi, Y. 2008. Hydrogen adsorption on single-walled carbon nanotubes studied by core-level photoelectron spectroscopy and Raman spectroscopy. *C arbon,* 46(14)**,** 1 9 0 3 –1 9 0 8.

Trucano, P. and Chen, R. 1975. Structure of graphite by neutron diffraction. *Nature,* 258(13)**,** 136-137.

Tulip, P. R. 2005. *Dielectric and lattice dynamical properties of molecular Crystals via density functional perturbation theory:implementation within a first principles code.* PHD Thesis, Durham university, UK.

Vanderbilt, D. 1990. Soft self-consistent pseudopotentials in a generalized eigenvalue formalism. *Physical Review B,* 41 (11)**,** 7892–7895.

Vitali, L., Schneider, M. A., Kern, M., Wirtz, L. and Rubio, A. 2004. Phonon and plasmon excitation in inelastic electron tunneling spectroscopy of graphite. *Physical Review B* 69(12)**,** 1-4.

Wang, D., Zhao, C., Xin, G. and Hou, D. 2010. Density functional theory study of the hydrogen chemisorption of single-walled carbon nanotubes with carbon ad-dimer defect. *Journal of Molecular Structure: THEOCHEM,* 962(1-3)**,** 62-67.

Wang, Y., Panzik, J. E., Kiefer, B. and Lee, K. K. M. 2012. Crystal structure of graphite under room-temperature compression and decompression. *Scientific Reports,* (2)**,** 1-7.

Warren, J. L., Yarnell, J. L., Dolling, G. and Cowley, R. A. 1967. Lattice Dynamics of Diamond. *Physical Review,* 158(3)**,** 805-808.

Wirtz, L. and Rubio, A. 2004. The phonon dispersion of graphite revisited *Solid State Communications* 131(3-4)**,** 141-152.

Wu, X., Yang, J. A. and Zheng, X. C. 2006. Adsorption of hydrogen molecules on the platinum-doped boron nitride nanotubes *The Journal of chemical physics,* 125(04)**,** 004704.

Yan, J.-A., Raun, W. Y. and Chou, M. Y. 2008. Phonon dispersions and vibrational properties of monolayer, bilayer, and trilayer graphene:Density-functional perturbation theory. *physical Review B,* 77(12)**,** 1-7.

Ye, L.-H., Liu, B.-G., Wang, D.-S. and Han, R. 2004. Ab initio phonon dispersions of single-wall carbon nanotubes. *Physical Review B,* 69(23)**,** 235409.

Yildirim, T., Gülseren, O. and Ciraci, S. 2001. Exohydrogenated single-wall carbon nanotubes. *Physical Review B,* 64(7)**,** 075404.

Yoshihara, K., Ishida, K., Wongwiriyapan, W., Inoue, S., Okabayashi, Y., Honda, S., Nishimoto, Y., Kuwahara, Y., Kenjiro, O. and Katayama, M. 2008. Hydrogen Interaction with Single-Walled Carbon Nanotubes. *Appl. Phys. Express,* 1(9)**,** 094001–094003.

Yoshimori, A. and Kitano, Y. 1956. Theory of the Lattice Vibration of Graphite. *Journal of Physical Society Japan,* 11(2)**,** 352-361.

Young, J. A. and Kopple, J. U. 1965. Phonon Spectrum of Graphite. *The Journal Of Chemical Physics,* 42(1)**,** 357-364.

Yurum, Y., Taralp, A. and Veziroglu, T. N. 2009. Storage of hydrogen in nanostructured carbon materials. *International Journal of Hydrogen Energy,* 34(09)**,** 3 7 8 4 – 3 7 9 8.

Zhang, G., Qi, P., Wang, X., Lu, Y., Mann, D., Li, X. and Dai, H. 2006. Hydrogenation and Hydrocarbonation and Etching of Single-Walled Carbon Nanotubes. *American Journal of Chemical Society,* 128(18)**,** 6026–6027.

Zhao, Y. X. and Spain, I. L. 1989. X-ray diffraction data for graphite to 20 GPa. *Physical Review B,* 40(2)**,** 993-997.

Zimmermann, J., Pavone, P. and Cuniberti, G. 2008. Vibrational modes and low-temperature thermal properties of graphene and carbon nanotubes: Minimal force-constant model. *Physical Review B,* 78(4)**,** 1-13.

Zólyomi, V. and Kürti, J. 2004. First-principles calculations for the electronic band structures of small diametersingle-wall carbon nanotubes. *Physical Review B,* 70(8)**,** 085403.

Appendices

Appendix A

A.1. Dispersion Corrected Parameters for TS Scheme

Table A-1 displays the inter layer spacing for the graphite system by fixing one by one the parameters damping of steepness function d and the scaling factor s_r. Table A-2, Table A-2 and Table A-6 show the sensitivity of frequency with respect to parameter d and s_r. These parameters are adjusted in order to obtain accurate values at low frequency in graphite system

Table A-1: Sensitivity of inter-layer spacing with respect to damping steepness and scaling factor s_r .

Damping function steepness d	Inter layer distance d (Å)	Scaling factor s_r	Inter layer distance d (Å)
25	3.33	0.95	3.36
20	3.33	0.94	3.33
15	3.33	0.92	3.29
10	3.32	0.90	3.25
5	3.28	0.89	3.22
-	-	0.88	3.2
-	-	0.86	3.16

Table A-2: Sensitivity of frequency with respect to scale factor s_r at damping steepness d = 15.

Scaling factor s_r	Inter layer distance d (Å)	Out of phase (cm^{-1})	Out of plane (cm^{-1})
0.87	3.20	45.4215	132.7468
0.86	3.18	45.1859	127.2613
0.85	3.19	44.9562	121.5345

Table A-3: Sensitivity of frequency with respect to damping steepness at scale factor $s_r = 0.94$.

Damping function Steepness d	Out of phase mode (cm^{-1})	Out of plane mode (cm^{-1})
20	46.1731	176.7918
15	44.3097	140.7838
5	41.4135	126.8182

Table A-4: Sensitivity of frequency with respect to scaling factor s_r at damping function steepness d = 20.

Scaling factor s_r	Out of phase mode (cm^{-1})	Out of plane mode (cm^{-1})
0.94	46.1371	176.7918
0.92	45.9561	169.6219
0.88	45.7376	139.3250
0.86	42.2883	128.8753
0.85	44.45035	115.6254

A.2.   Dispersion Corrected Parameters for G06 Scheme

These tests for frequency sensitivity with respect to scaling parameter s_6 were performed in order to adjust the dispersion corrected parameters for a 4-atom unit cell in graphite at the Gamma point of the Brillouin zone.

Table A-5: Sensitivity of frequency with respect to scaling factor s_6 at damping function steepness d = 20.

Scaling factor s_6	Out of phase mode (cm^{-1})	Out of plane mode (cm^{-1})
0.75	53.23083	150.5775
0.85	53.20712	147.5470
0.95	53.18340	144.4519
1.05	53.15967	141.2878
1.3	53.10028	133.0434
1.4	53.07650	129.5966
1.45	53.06461	127.8379
1.48	53.05747	126.7708
1.5	53.05272	126.0544

A.3. Dispersion Curve of Diamond

The dispersion curve of diamond having two atoms in a primitive cell has been calculated using the finite displacement approach. Supercell of size 2×2×2 has been used to perform dynamical calculations. Most tetrahedral semiconductors have a particular flatness of the transverse acoustic (**TA**) modes over a large portion of Brillouin Zone (**BZ**). However the case of diamond is different; the **TA** acoustic branches are no longer flat and the frequency of **LO** decreases from **Γ** to **L** and **X** point due to over bending as shown in Figure A-1. Another very interesting feature has been found in the spectrum in that the maximum of the optical branches was not at the zone centre. Symbols **Γ/G, L, X, W** represent high symmetry points labelling the Brillouin Zone of a face centred cubic crystal. Long range interactions can be responsible for the flattening of the phonon dispersion in zinc blende and diamond semiconductor along the **K-X** line. This study is in general agreement with previous ab initio and experimental studies. Experimental values given in Table A-6 were reported by Warren et al. (1967) on the basis of inelastic neutron scattering for the diamond system.
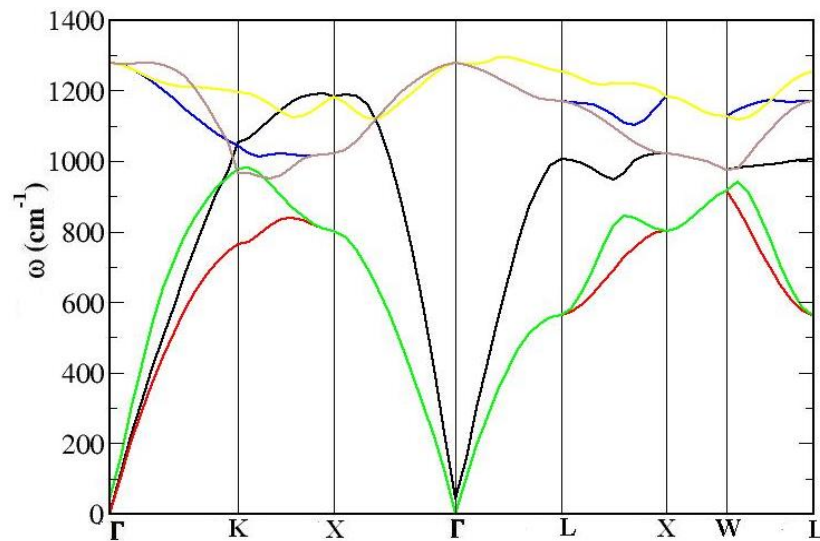
Figure A-1: Dispersion curve of diamond by finite displacement approach along the high symmetry direction.

Table A-6: Calculated values of frequency corresponding to modes of vibration by PBE functional.

Modes	Γ_O	X_{TA}	X_{TO}	X_{LO}	L_{TA}	L_{LA}	L_{TO}	L_{LO}
Ab initio	1278	801	1021	1181	563	1006	1170	1253
Experimental	1331	803	1077	1194	552	1035	1210	1242

A.4. Linear Response

In the microscopic linear response approach, the total energy of the system is calculated in the frame work of the dielectric matrix which contains the electric response of the material to linear order. Linear response is an approach to model lattice dynamics using density functional perturbation theory (Barno et al., 1987). This method describes the analytical derivative of the total energy with respect to a given perturbation. If such a perturbation is in the atomic positions then this directly calculates the dynamical matrix as in equation (4.12) and therefore leads to the normal modes of phonons.

The linear response method applies by minimizing the second order perturbation in the total energy, which gives the first order changes in the wave function, charge density and potential (Gonze, 1997). The equation minimized in this approach (as implemented by CASTEP 6.0 (Clark et al., 2005)) is

$$
\begin{aligned}
E^2 = \sum_{k,n} \Bigg\{ &\left\langle \Psi_{k,n}^{(1)} \middle| H^{(0)} - \varepsilon_{k,n}^{(0)} \middle| \Psi_{k,n}^{(1)} \right\rangle + \left\langle \Psi_{k,n}^{(1)} \middle| V^{(1)} \middle| \Psi_{k,n}^{(1)} \right\rangle \\
&+ \left\langle \Psi_{k,n}^{(0)} \middle| V^{(1)} \middle| \Psi_{k,n}^{(1)} \right\rangle \\
&+ \frac{1}{2} \int \frac{\delta^2 E_{xc}}{\delta n(r) \delta n(r')} n^{(1)}(r) n^{(1)}(r') \\
&+ \sum_{k,n} \left\langle \Psi_{k,n}^{(0)} \middle| V^{(2)} \middle| \Psi_{k,n}^{(0)} \right\rangle \Bigg\}
\end{aligned}
\tag{A.1}
$$

The superscripts (0), (1) and (2) denote the ground state and first and second order changes. The dynamical matrix is generated from the converged first order wave

function $\Psi^{(1)}$ and density $n^{(1)}(r)$. Linear response theory is not yet available for the ultrasoft pseudopotential in CASTEP code.

Appendix B

B.1. Structure File of CNT(4,4)

data_nanotube

_audit_creation_method   '(4,4) Nanotube -- TubeGen 3.3, J T Frey, University of Delaware

_cell_length_a   8.8181
_cell_length_b   8.8181
_cell_length_c   2.4630
_cell_angle_alpha   90.00
_cell_angle_beta   90.00
_cell_angle_gamma   120.00

```
C     2.735532    0.000000    -1.231487
C     2.366455    1.372233    -1.231487
C     1.934313    1.934313    0.000000
C     0.703021    2.643652    0.000000
C    -0.000000    2.735532    -1.231487
C    -1.372233    2.366455    -1.231487
C    -1.934313    1.934313    0.000000
C    -2.643652    0.703021    0.000000
C    -2.735532    0.000000    -1.231487
C    -2.366455    -1.372233    -1.231487
C    -1.934313    -1.934313    0.000000
C    -0.703021    -2.643652    0.000000
C     0.000000    -2.735532    -1.231487
C     1.372233    -2.366455    -1.231487
C     1.934313    -1.934313    0.000000
C     2.643652    -0.703021    0.000000
```

B.2. Structure File of CNT(4,4)H

```
%BLOCK LATTICE_ABC
     13.6797  13.6797    2.4630
      90          90         120
%ENDBLOCK LATTICE_ABC

%BLOCK POSITIONS_ABS
C          2.735532              0      -1.23149
C          2.366455       1.372233      -1.23149
C          1.934313       1.934313             0
C          0.703021       2.643652             0
C                 0       2.735532      -1.23149
C         -1.37223        2.366455      -1.23149
C         -1.93431        1.934313             0
C         -2.64365        0.703021             0
C         -2.73553              0      -1.23149
C         -2.36646       -1.37223      -1.23149
C         -1.93431       -1.93431             0
C         -0.70302       -2.64365             0
C                 0       -2.73553      -1.23149
C          1.372233       -2.36646      -1.23149
C          1.934313       -1.93431             0
C          2.643652       -0.70302             0
H          3.835489              0      -1.23149
H          3.318007       1.924008      -1.23149
H          2.7121          2.7121              0
H          0.985706       3.706664             0
H                 0       3.835489      -1.23149
H         -1.92401        3.318007      -1.23149
H         -2.7121          2.7121              0
H         -3.70666        0.985706             0
H         -3.83549              0      -1.23149
H         -3.31801       -1.92401      -1.23149
H         -2.7121         -2.7121              0
H         -0.98571        -3.70666             0
H                 0       -3.83549      -1.23149
H          1.924008       -3.31801      -1.23149
H          2.7121         -2.7121              0
H          3.706664       -0.98571             0
%ENDBLOCK POSITIONS_ABS

symmetry_generate
```

SNAP_TO_SYMMETRY

kpoint_mp_grid   1 1 20

%BLOCK SPECIES_POT
   C 2|1.4|9.187|11.025|12.862|20UU:21UU(qc=6)[]
%ENDBLOCK SPECIES_POT

B.3. Lattice Constants of Optimized CNTs

Table B-1: Lattice constants of geometry optimized structures of CNTs.

Materials	Types of Nanotubes	a(Å)	b(Å)	c(Å)
CNT(4,0)	zigzag	9.6649	9.6649	4.2194
CNT(4,0)H		10.2625	10.2625	4.3308
CNT(5,0)	zigzag	11.9117	11.9117	4.2644
CNT(5,0)H		12.7589	12.7589	4.3508
CNT(6,0)	zigzag	11.9498	11.9498	4.2662
CNT(6,0)H		13.0005	13.0005	4.3853
CNT(7,0)	zigzag	13.4840	13.4840	4.2726
CNT(7,0)H		14.7952	14.7952	4.4075
CNT(8,0)	zigzag	15.2672	15.2672	4.2721
CNT(8,0)H		13.0005	13.0005	4.3853
CNT(9,0)	zigzag	15.051	15.051	4.2744
CNT(9,0)H		16.8024	16.8024	4.4462
CNT(10,0)	zigzag	15.8343	15.8343	4.2760
CNT(10,0)H		17.7897	17.7897	4.4634
CNT(4,4)	armchair	12.4079	12.4079	2.4685
CNT(4,4)H		14.8880	14.8880	2.5930
CNT(5,5)	armchair	14.9049	14.9049	2.4678
CNT(5,5)H		17.2612	17.2612	2.6134

Materials	Types of Nanotubes	a(Å)	b(Å)	c(Å)
CNT(6,6)	armchair	17.0163	17.0163	2.4624
CNT(6,6)H		18.9728	18.9728	2.6319
CNT(8,8)	armchair	19.3770	19.3770	2.4678
CNT(8,8)H		21.9279	21.9279	2.6594
CNT(9,9)	armchair	21.2120	21.2120	2.4675
CNT(9,9)H		24.1048	24.1048	2.6705
CNT(10,10)H	armchair	21.5695	21.5695	2.4675
		24.6284	24.6284	2.6799
C_8H_8(Cubane)		9.1543	9.1543	9.1543

B.4. Vibrational Density of States of CNTs and Hydrogenated CNTs
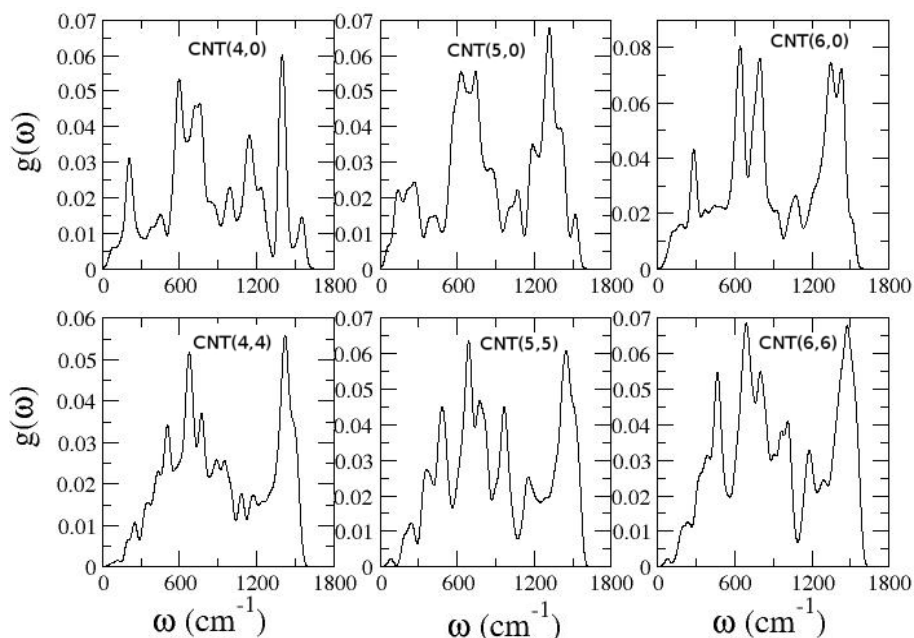
Figure B-1: Vibrational density of states of pristine zigzag and armchair CNTs.
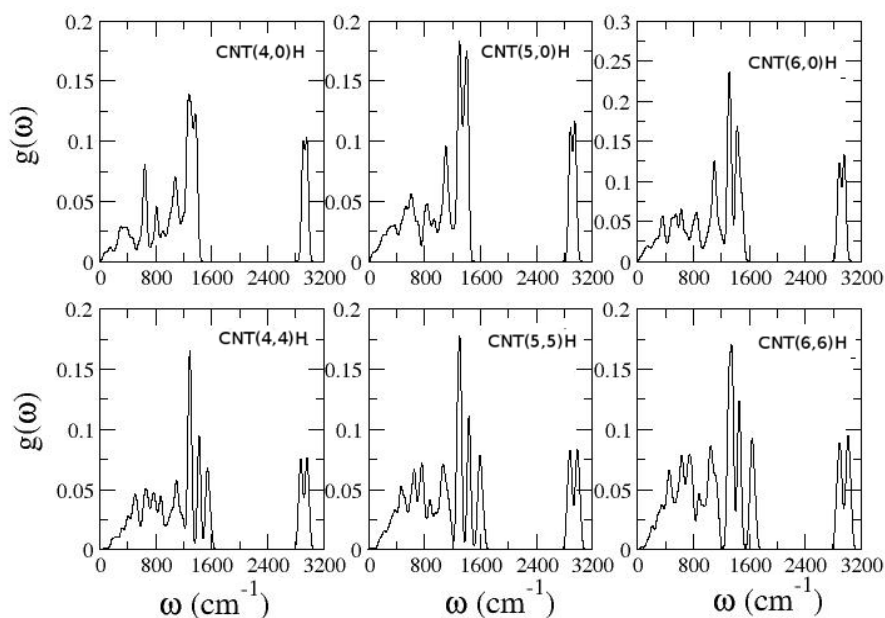
Figure B-2: Vibrational density of states of hydrogenated zigzag and armchair CNTs

B.5. Dispersion Curves of CNTs and Hydrogenated CNTs
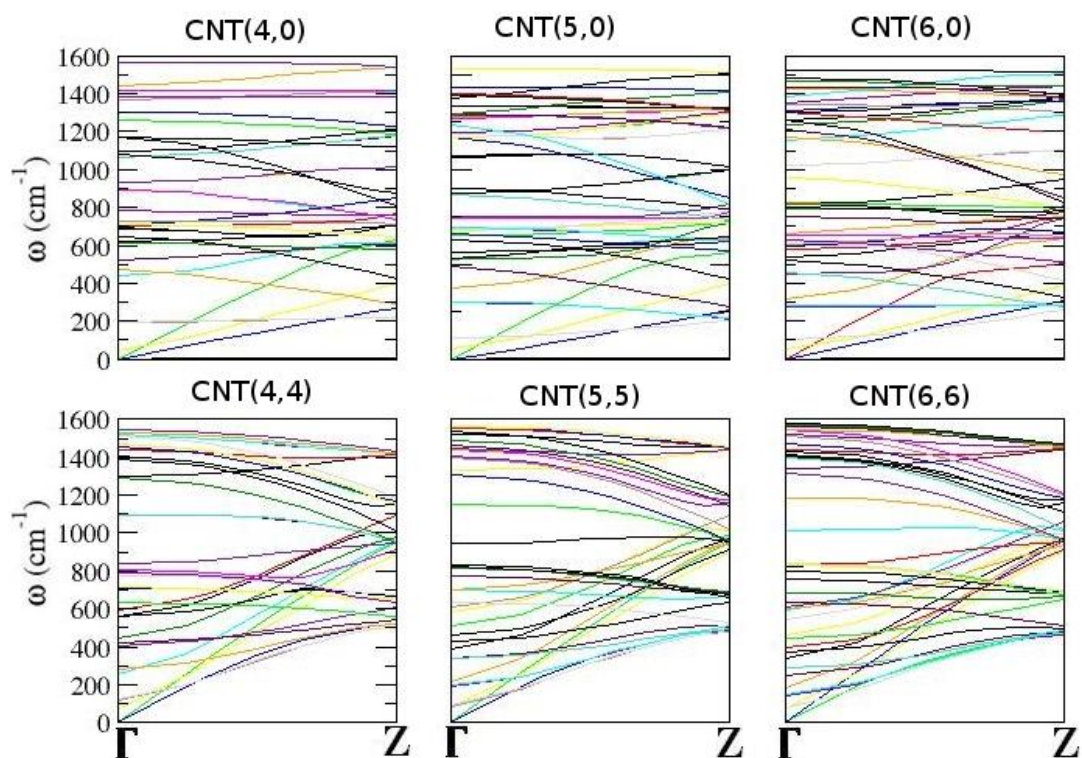
Figure B-3: Dispersion curve of pristine zigzag and armchair CNTs.
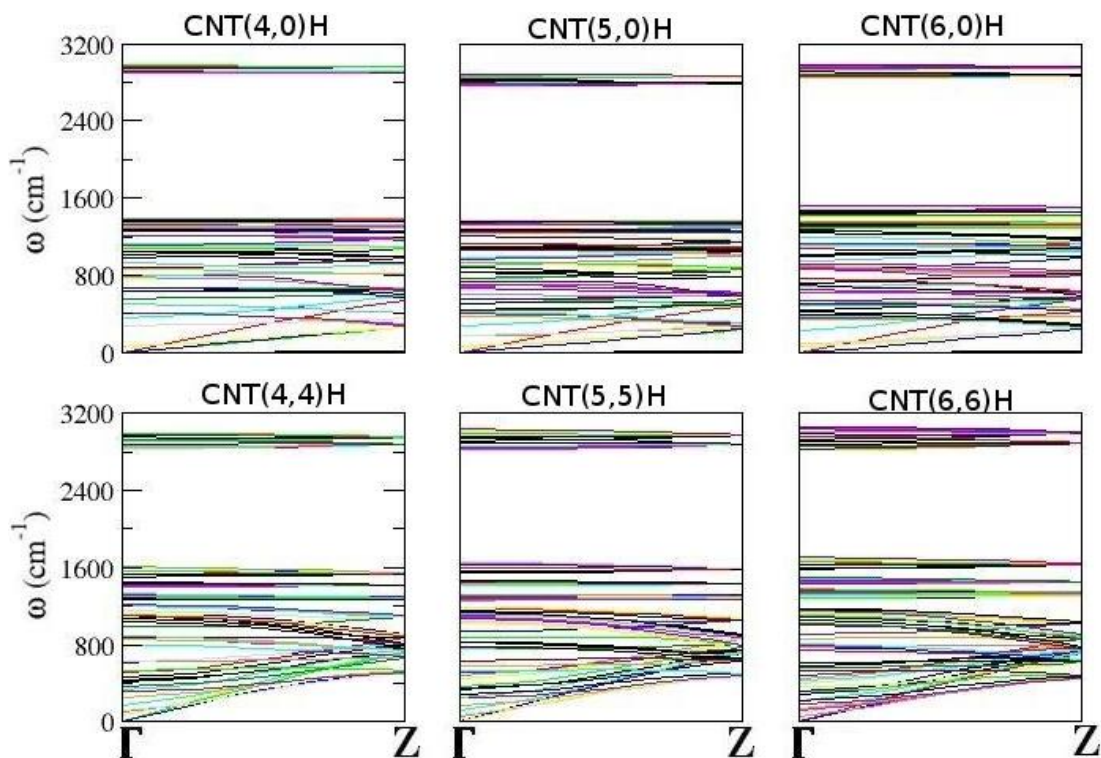

Figure B-4: Dispersion curve of hydrogenated zigzag and armchair CNTs.

B.6. Hydrogen Molecule Free Energies

Table B-2 shows the translational, rotational and vibration free energies (including ZPE) of H_2 molecule. Translation and rotational free energies were calculated using the statistical physics relations as described in section (4.6) and vibration free energies (including ZPE) were calculated using the CASTEP code (Clark et al., 2005).

Table B-2: Free Energies of hydrogen molecule.

Temperature (K)	Translational Energy (eV)	Rotational Energy (eV)	Vibrational Energy (eV)
0	0	0	0.311953
30	-0.011486383	0.00241559	0.311953
60	-0.033369974	0.000672297	0.31195
90	-0.059177926	-0.00264074	0.311896
120	-0.087534363	-0.006973172	0.311643
150	-0.117785837	-0.012063618	0.311045
180	-0.149547474	-0.01775813	0.310017
210	-0.182564964	-0.023954983	0.308527
240	-0.216657557	-0.030581877	0.306572
270	-0.251690106	-0.037584753	0.304165
300	-0.287557712	-0.044921652	0.301325
330	-0.324176574	-0.052559053	0.298075
360	-0.361478195	-0.060469559	0.294437
390	-0.399405542	-0.068630354	0.290432
420	-0.437910382	-0.077022147	0.286081
450	-0.476951393	-0.085628408	0.281401
480	-0.516492775	-0.094434818	0.276411
510	-0.556503213	-0.10342885	0.271125
540	-0.596955082	-0.112599454	0.265559
570	-0.637823832	-0.121936811	0.259725
600	-0.679087502	-0.131432135	0.253636
630	-0.720726328	-0.141077522	0.247303

Temperature (K)	Translational Energy (eV)	Rotational Energy (eV)	Vibrational Energy (eV)
659.9	-0.76258187	-0.150832963	0.240736
689.9	-0.804917889	-0.160757227	0.233944
719.9	-0.847580145	-0.170811987	0.226935
749.9	-0.890555035	-0.180991799	0.219719
779.9	-0.933830045	-0.19129166	0.212301
809.9	-0.977393625	-0.201706949	0.204689
839.9	-1.021235081	-0.212233388	0.19689
869.9	-1.065344483	-0.222867005	0.188908
899.9	-1.109712586	-0.233604103	0.180749
929.9	-1.154330763	-0.244441231	0.172418
959.9	-1.199190944	-0.25537516	0.163919
989.9	-1.244285563	-0.266402864	0.155258
1019.9	-1.289607512	-0.277521501	0.146437
1049.9	-1.335150102	-0.288728394	0.137461
1079.9	-1.380907028	-0.300021021	0.128334
1109.9	-1.426872334	-0.311397	0.119057
1139.9	-1.473040385	-0.322854077	0.109636
1169.9	-1.519405844	-0.334390117	0.100071
1199.9	-1.565963649	-0.346003096	0.090367
1229.9	-1.612708989	-0.357691089	0.080526
1259.9	-1.659637289	-0.369452265	0.07055
1289.9	-1.706744191	-0.381284883	0.060442
1319.9	-1.754025542	-0.39318728	0.050204
1349.9	-1.801477374	-0.405157869	0.039837
1379.9	-1.849095899	-0.417195136	0.029345
1409.9	-1.896877492	-0.42929763	0.018729
1439.9	-1.944818683	-0.441463963	0.00799
1469.9	-1.992916146	-0.453692805	-0.002868
1499.9	-2.041166692	-0.46598288	-0.013845
1529.9	-2.089567257	-0.478332963	-0.024939
1559.9	-2.138114901	-0.490741877	-0.036149

Temperature (K)	Translational Energy (eV)	Rotational Energy (eV)	Vibrational Energy (eV)
1619.9	-2.235640212	-0.515731715	-0.058907
1649.9	-2.284612536	-0.528310502	-0.070453
1679.9	-2.33372124	-0.54094384	-0.082108
1709.9	-2.382963887	-0.553630756	-0.093872
1739.9	-2.432338128	-0.566370309	-0.105742
1769.9	-2.481841693	-0.579161591	-0.117717
1799.9	-2.53147239	-0.592003727	-0.129797
1829.9	-2.5812281	-0.604895867	-0.141979
1859.9	-2.631106772	-0.617837193	-0.154263
1889.9	-2.681106425	-0.630826911	-0.166648
1919.8	-2.731057878	-0.643820716	-0.179131
1949.8	-2.7812934	-0.656904781	-0.191714
1979.8	-2.831644322	-0.670035007	-0.204393
2009.8	-2.882108897	-0.683210694	-0.217169
2039.8	-2.932685428	-0.696431163	-0.230039
2069.8	-2.983372268	-0.709695756	-0.243004
2099.8	-3.034167817	-0.723003832	-0.256061

B.7. Vibrational Contribution for Hydrogen Releasing Temperature

Table B-3 displays the hydrogen releasing temperatures using the vibrational free energy from CASTEP code. Hydrogen releasing temperature increases with increase in diameters in both armchair and Zigzag CNTs.

Table B-3: Hydrogen releasing temperature using vibrational contribution.

Reactants	Product	Hydrogen Releasing Temperature (K)
$CNT(4,0) + 8H_2$	$C_{16}H_{16}$	785
$CNT(5,0) + 10H_2$	$C_{20}H_{20}$	793
$CNT(6,0) + 12H_2$	$C_{24}H_{24}$	804
$CNT(8,0) + 16H_2$	$C_{32}H_{32}$	830
$CNT(4,4) + 8H_2$	$C_{16}H_{16}$	812
$CNT(5,5) + 10H_2$	$C_{20}H_{20}$	845
$CNT(6,6) + 12H_2$	$C_{24}H_{24}$	849

Appendix C

C.1.   Publications

- R.M.A.Khalil and I.Morrision, "Structural and Vibrational Properties of Graphite by incorporating the Dispersion Correction" CASTEP Workshop, 19-23 Aug., 2013, Oxford, UK.

- R.M.Arif.Khalil and I.Morrison, "Structural and Dynamical Studies of Graphitic Materials", 4th CSE Doctoral School Postgraduate Research Conference, 13/11/2013, Salford, UK.

- R.M.Arif.Khalil and I.Morrison, "An Accurate Dispersion Corrected Studies of Structural and Vibrational Properties of Graphite", Dean's Annual Research Show Case, 18/06/2014, Salford, UK.